Ecole Centrale de Nantes

ÉCOLE DOCTORALE

SCIENCES POUR L'INGENIEUR GEOSCIENCES ARCHITECTURE

Année 2011 N° B.U. :

Thèse de DOCTORAT

Spécialité : GENIE CIVIL

Présentée et soutenue publiquement par:

SYED YASIR ALAM

le 10 Mai 2011
à l'Ecole Centrale de Nantes

TITRE

EXPERIMENTAL STUDY AND NUMERICAL ANALYSIS OF CRACK OPENING IN CONCRETE

JURY

Président :	M. Gilles PIJAUDIER-CABOT	Professeur - Université de Pau et des Pays de l'Adour
Rapporteurs :	M. Frédéric COLLIN	Chercheur qualifié FNRS - Université de Liège
	M. Alain SELLIER	Professeur - Université Paul Sabatier, Toulouse
Examinateurs :	M. Nicolas CHEVAUGEON	Maître de Conférences - Ecole Centrale de Nantes
	M. Panagiotis KOTRONIS	Professeur - Ecole Centrale de Nantes
	M. Ahmed LOUKILI	Professeur - Ecole Centrale de Nantes
	M. Stéphane MOREL	Maître de Conférences, HDR - Université de Bordeaux I
	M. Jean Michel TORRENTI	Professeur - Ecole Nationale des Ponts et Chaussées

---

Directeur de thèse : Ahmed LOUKILI
Laboratoire : Institut de Recherche en Génie Civil et Mécanique, Nantes
Co-encadrant : Nicolas CHEVAUGEON
Laboratoire : Institut de Recherche en Génie Civil et Mécanique, Nantes

N° ED 498 - 181

ACKNOWLEDGMENTS

I would like to express my deepest gratitude to Higher Education Commission of Pakistan for the financial support towards my Doctorate degree.

I am highly grateful to Prof. Ahmed Loukili, my dissertation director for his guidance, support and encouragement during all these years. Discussion with him has always been a source of enthusiasm for me to perform quality research. I am very thankful to Prof. Panagiotis Kotronis, for his help, advice and fruitful discussions. I am also grateful to Dr. Nicolas Chevaugeon, my co-supervisor for his kind assistance during this study.

I am grateful to the students, Annie and Thibault who worked with me during this research work.

I'm indebted to Mr. Jean-Pierre Regoin for his expertise in building the experimental setup and full fledge cooperation through out this research. I am also thankful to Mr. Jean-Yves Letouzo and Mr. Patrick Denain for their skilled assistance in building the experimental setup.

I thank all the colleagues of the Civil Engineering group for their support more specifically for the administrative issues and the French language. I am highly grateful to my colleague friends Achraf and Jacqueline for their continuous help and the friendly environment during work.

I am very thankful to my Pakistani friends, Bilal, Sami, Atif, Naeem,…… for the support and loving environment during my stay.

I cannot thank enough to my parents and my sister for their love, support and prayers without which I would not be able to complete this task.

I am also thankful to my wife for her understanding, support, love and encouragement in the difficult phases of this journey.

ABSTRACT

It is commonly accepted that there is a size effect on the nominal resistances of quasi-brittle materials such as cementitious materials. This effect must be taken into account in the design of the ultimate behaviour of concrete structures in order to avoid damage and crack openings. These parameters are frequently used to study the behaviour of concrete and to characterize the durability of structures. Different theories exist in the literature to describe the size effect. Among them, we find the deterministic theory of Bazant where fracture energy is considered independent of the size and it is assumed that at peak load, the crack length is proportional to the size of the specimen.

In this work, attention is paid to investigate experimentally and numerically, the relationship between crack openings and length, and the size of the specimens.
In the experimental study, RILEM size effect method is adopted to test geometrically similar concrete beams of various sizes. Two types of concrete mixes are used with varying aggregate sizes in order to further investigate the effect of aggregate size on fracture behaviour. Digital Image Correlation (DIC) technique is adopted in this study to measure the cracking in concrete on the surface of the concrete specimen. It is established as a robust and highly precise tool for fracture measurements such as crack opening and crack length. The results have shown a significant size effect on the process of crack propagation. Furthermore, as the aggregate size increases the size effect becomes more critical. A case study of the size effect on crack openings and crack spacing in reinforced concrete beams is also presented. From serviceability point of view, it is observed that the Eurocode 2 underestimates the crack openings.

In the numerical study, the concrete beams are simulated using a nonlocal damage model. The internal length and other model parameters are calibrated by an inverse calibration technique using an automatic procedure. Crack opening profiles are extracted through post-treatment procedures. The mechanical behaviour and the crack propagation are finally analysed, reflecting a similar size effect as detected by the experimental results.

KEYWORDS

Concrete, cracking, crack opening, crack length, size effect, digital image correlation, nonlocal, modelling, damage, automatic calibration, inverse calibration.

RÉSUMÉ

Il est communément admis l'existence d'un effet d'échelle sur les résistances nominales des matériaux quasi-fragiles tels que les matériaux cimentaires. Cet effet doit être pris en compte dans le dimensionnement vis-à-vis du comportement ultime des structures en béton afin de limiter les dommages et les ouvertures de fissures. Celles-ci sont de plus en plus utilisées pour étudier le comportement du béton et caractériser la durabilité des structures. Différentes théories existent dans la littérature pour décrire l'effet d'échelle. Parmi celles-ci on trouve la théorie déterministe de Bazant où l'énergie de fissuration est considérée comme indépendante de la taille et il est supposé qu'à charge maximale, la longueur de fissure est proportionnelle à la taille de l'échantillon.

Dans le cadre de ce travail, on s'est attaché à étudier expérimentalement et numériquement les relations entre la longueur de fissure et la taille des éprouvettes.
Sur le plan expérimental, l'effet d'échelle est caractérisé par des essais de flexion trois points sur des poutres de béton entaillées de tailles géométriquement similaires. L'influence de la taille des agrégats sur le comportement à la rupture a aussi été étudiée. La technique de Corrélation d'Images Numériques (DIC) est adoptée dans cette étude pour déterminer à la fois la longueur et l'ouverture de la fissure à différentes étapes de chargement. Cette méthode s'est révélée comme un outil robuste et de haute précision pour la mesure des paramètres caractérisant les fissures. Les résultats ont montré un effet de taille significatif sur le processus de propagation des fissures. En outre, l'effet d'échelle diminue lorsque la taille des agrégats augmente. Une étude sur poutres en béton armé est aussi réalisée pour étudier l'effet d'échelle sur l'ouverture et l'espacement des fissures. De point de vue réglementaire, il a été observé que l'Eurocode 2 sous estime les ouvertures de fissures.

Sur le plan numérique, le comportement à la rupture des poutres en béton est simulé en utilisant un modèle d'endommagement non local. La longueur interne et d'autres paramètres du modèle sont calibrés par une technique de calibration inverse qui utilise une procédure automatique. Les profils d'ouverture de fissures sont déterminés par des procédures de post-traitement. L'analyse du comportement mécanique et de la propagation des fissures indiquent un effet d'échelle similaire à celui détecté par les résultats expérimentaux.

MOTS-CLÉS

Béton, fissuration, ouverture de fissure, longueur de fissure, effet d'échelle, corrélation d'images, nonlocal, modélisation, endommagement, calibration automatique, calibration inverse.

TABLE OF CONTENTS

GENERAL INTRODUCTION

Cracks are everywhere around us. Any quasi-brittle material like concrete is generally full of cracks. Throughout the decades, humans have been trying to understand the mechanism of the growth of cracks. In particular, after the pioneering work of Griffith on the quasi-brittle growth of cracks, much research has been directed towards a better and deeper understanding of this observed phenomenon.

It is known that the mechanical behaviour of quasi-brittle composites such as concrete, coarse grained ceramics and fibre-reinforced composites, is manifested by mechanisms like strain localization and progressive fracture in the material. The fracture is usually in the form of multiple cracks branching out in the zone where strains are localized. This is an intrinsic property of quasi-brittle materials and the Fracture Process Zone (FPZ) is generally considered as a characteristic parameter which is used to analyze the failure process. Due to the sizable FPZ in comparison with structure/specimen size, the linear elastic fracture mechanics (LEFM) laws cannot be applied.

Many theoretical techniques consider the size of FPZ as a material parameter. In these theories, the fracture process (or material degradation) is assumed to be accumulated in a certain length or width of FPZ at the crack tip. In this regard, the first attempt was made by Irwin [59], who identified the singularity of the (LEFM) stress-field at the crack tip and proposed the presence of a crack tip plastic zone. Hillerborg [51] improved the Irwin model by replacing the crack tip plastic stress with monotonic decreasing cohesive stress. He assumed that the energy dissipation during fracture process can be completely characterized by a cohesive stress-crack opening relationship. He regarded the fracture energy as a size/shape independent material property represented by the area under the entire softening stress-crack opening curve. Unlike Hillerborg, a distributed microcracking effect was considered by Bazant and Oh [11]. They modelled the fracture process zone with a band of uniformly distributed microcracks (or damage zone) which had a fixed width. In order to determine size/shape independent fracture energy, the damage band width was regarded as a material property (related to the size of aggregates in concrete). Recently, however, Duan and co-workers [38] have proposed a fracture model in which the fracture energy is subjected to boundary effects related to the crack length. Their model is based on the experimental observations that FPZ size is not constant as the crack reaches the boundary of the specimen/structure. Other researchers also consider that evolving dimensions of FPZ should be taken into account [94, 45].

Size effect in concrete structures

The study of the fracture behaviour of concrete cannot be separated from the size effect. In these materials, a large sized FPZ is present which consumes a considerable amount of energy supplied by the applied load. As a consequence, a decrease of nominal strength σ_N can be observed with the increase in size. Considering any type of geometrically similar specimens or structures of various sizes, with geometrically similar cracks, the variation of structural strength can be described by plotting the logarithm of the nominal stress σ_N versus the logarithm of their size (Figure 0.1).

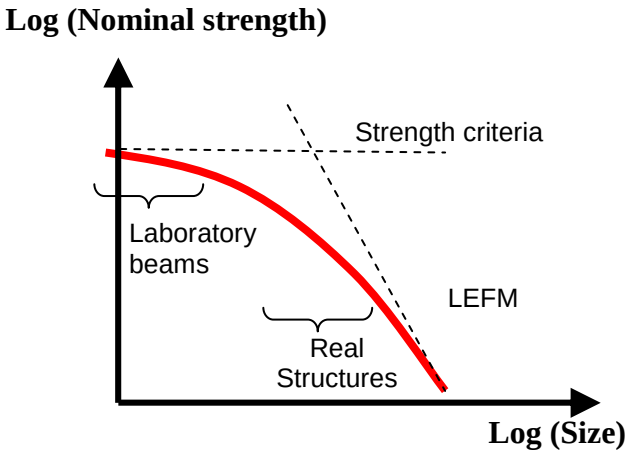

Figure 0.1 Transitional scaling of nominal strength of quasi-brittle structures [10].

On one hand, the strength criterion predicts σ_N at failure to be independent of size, while all tests indicate a decrease of σ_N when the size increases. On the other hand and according to the LEFM, σ_N is proportional to $(\text{size})^{-1/2}$. This slope, however, appears to be too steep in comparison with the experimental data. The reality seems to be a gradual transition from the horizontal straight line for the strength criterion, to the inclined straight line of slope – ½ for LEFM.

Scope of the thesis

In order to test the robustness of the different numerical models used to predict the mechanical behaviour, fracture behaviour and the size effect, one needs to use experimental data on nominal strength but also on crack openings and crack lengths. Nevertheless, crack openings and crack lengths are very difficult to measure. Different techniques have been introduced in the past e.g. LVDTs, dye penetration method, acoustic emissions and interferometry [91] but they do not usually provide accurate measurements. Other techniques are able to produce precise crack openings and lengths but are not accessible to everyone and present many limitations to their application (e.g. microtomography and X-Rays).

In this thesis, a large scale experimental campaign on geometrically similar concrete specimens has been conducted. In order to measure crack openings and crack lengths on the surface of the specimens the Digital Image Correlation technique (DIC) has been adopted. It is a robust technique and provides fracture measurement of high precision.

The numerical models usually used to describe crack or damage growth in concrete can be divided into two categories: models based on a continuum damage approach and on a discrete crack approach. Models based on continuum mechanics are incapable of determining crack openings directly. Therefore, post treatment procedures have been developed to extract the crack profiles from a continuum strain field [80, 81]. Discrete crack models are based on an explicit description of the discontinuity within the material e.g. cohesive crack model of Hillerborg [51]. Generally, the entire energy that is dissipated in the FPZ is "converted" into a crack length. Some part of this energy may be dissipated in the process zone outside the crack, and it follows that the crack length and the crack opening are probably overestimated. Furthermore, global experimental results (e.g. load versus displacement) are often used in literature to calibrate the above models and therefore they predict the maximum load well but not predict crack profiles, openings and length at different loading stages accurately.

In this work we choose to work with a classical non local damage mechanics model calibrated with global parameters (crack mouth opening displacements, CMOD) coming from the experimental campaign coupled with an optimisation algorithm, in order to improve the representation of size effect. Validation is provided using global but also local results.

Outline of the thesis

The above problem is analysed in the present document in four chapters.

- The first chapter presents a literature review of different physical mechanisms involved in the cracking process of concrete. The objective is to present state of the art developments and the tools to comprehend the problem. Finally, the basis of the principal physical theories, interpretations and experimental observations by different researchers, are discussed
- The second chapter is dedicated to the procedures, techniques and protocols adopted in the experimental campaign. Digital Image Correlation technique (DIC) and its application as a fracture measuring tool are discussed. RILEM (*Reunion Internationale des Laboratoires et Experts des Materiaux, Systemes de Construction et Ouvrages*) recommended test methods to measure fracture parameters of concrete are presented briefly, including RILEM

recommendation of the size effect method. The merits and demerits of these methods are discussed. Details of the experimental campaign are then presented, including material aspects, specimen preparation, experimental setup and the loading system.

- In the third chapter, experimental results of three point bending tests on concrete beams are analysed in order to characterize the fracture process. Crack opening is used as a key parameter. Experimental data of loading and crack notch opening displacement are analyzed first. Then, an experimental method to measure the crack opening displacement and profile using DIC is presented. The fracture process is monitored and the effect of aggregate size on cracking is also studied. The size effect is also identified on the mechanical response and crack opening respectively. Lastly a case study is presented in which crack openings and crack spacing in reinforced concrete beams are monitored. The results are compared with the values obtained by Eurocode expressions.
- In the fourth chapter, the most frequently used numerical approaches to simulate crack propagation are presented. Damage mechanics concepts for concrete structures are described in detail. Numerical simulations are then carried out using a nonlocal damage model. Validation is provided by comparing with the experimental results.

Chapter 1

Literature Review on Cracking in Concrete

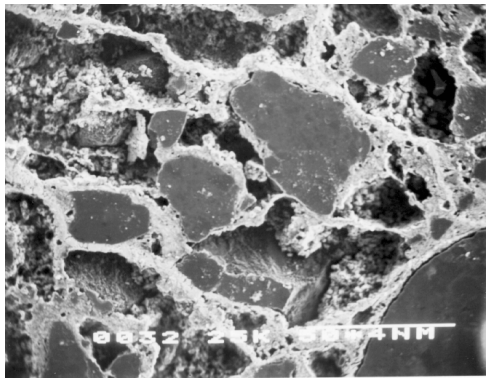

Failure in concrete is usually accompanied by cracking. Concrete being a tension-weak material, the process of cracking is more critical under tensile loadings. It is often found in literature that concrete even cracks under its own weight.

Crack creation and its propagation are the results of physical processes that are generally explained using the laws of conservation of energy. In most of these theories, concrete is assumed as a homogenous material. However, the effect of the fabrication process and the constituents shape and size influence the cracking process. Crack usually initiates from the weakest link in the material. It develops under the action of stresses developed around it. The process involves phenomena from the very small scale (e.g. uneven distribution of calcium silica hydrates which is the main hydration component) to the very large scale (e.g. effect of structural dimensions, known as size effect).

This chapter presents a bibliographic review of different physical processes affecting the cracking mechanism in concrete.

- In the first section, the different possible scales of observation are discussed.
- The second section describes the microstructural properties of concrete that may influence the fracture process.
- In the third section, a state of the art review on the fracture behaviour of concrete under the action of tensile loadings is presented. Discussion is made on the basis of physical interpretations and experimental observations provided by different researchers.
- The effect of structural size on the fracture behaviour of concrete is presented in the last section. Bazant's size effect theory is discussed in detail.

1.1 Morphology of concrete and different levels of observation

Concrete is generally considered as a continuum material in most numerical models. Nevertheless, its material structure varies depending on the scale of observation. In Figure 1.1 [55], it can be seen that concrete is a multi-scale material. Cement, sand, aggregates, water and sometimes other additives are mixed together and hardened to form a solid structure.

- The smallest or elementary particle of concrete is the atomic form of the cement and aggregates, which can be observed at nanometre scale (10^{-9} *m*).
- Then, the individual cement hydrated products are identified at micrometer scale (10^{-6} *m*). This includes primarily calcium-silicate-hydrate (C-S-H), calcium-hydroxide (C-H) and calcium sulfo-aluminates (ettringite, $C_3A.3CaSO_4.32H_2O$). The complex pore structure becomes visible as well.
- In the next scale (10^{-3} *m*), also known as meso-scale, concrete is generally considered as a two phase material consisting of matrix and aggregates. Internal voids ranging up to several millimetres in size may be regarded as another important component of the hardened concrete. This void structure or defects depend on the packing of aggregate particles in the cement matrix. They mainly includes pores in the cement paste, cracks at the aggregate interface and shrinkage cracks. These defects play an important role in the mechanical behaviour of concrete.
- In the next scale (10^{-3} to 10^{+0} *m*), the laboratory scale (mechanical) experiments are carried out. No internal structure is emphasized and the overall mechanical response is generally of importance. This scale is often called as macro-scale. In this scale and even in the larger scale (10^{+3} *m* and more), the material is assumed to have isotropic properties. At larger scales i.e. the scale of buildings and other civil engineering structures, the material is modelled as a continuum, or alternatively, some internal structure details can be identified, specifically when structure is formed by steel reinforcement.

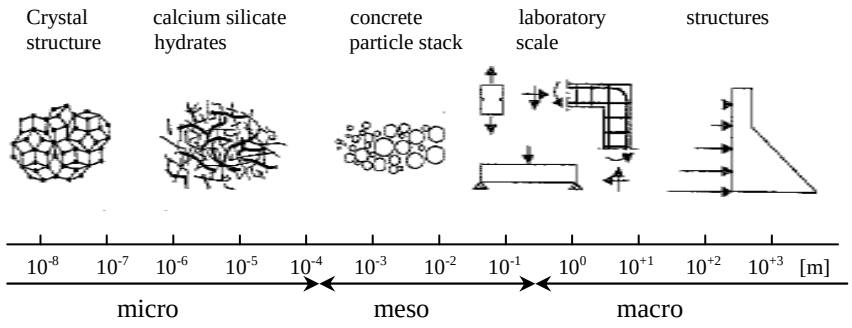

Figure 1.1 Various scales of observation of concrete material from atomic structure to large scale building (from [124]).

In material science of concrete structures, research is concentrated mainly into three levels of observation, namely the micro-level, the meso-level and the macro-level [133] identified in the previous paragraphs. Different mechanisms are occurring in the different scales. It is now understood that the mechanical behaviour depends on the fracture process. As concrete is a multi-scale and multi-phase material, the fracture process occurs within the micro and the meso-scale. In the next section, a brief description of the microstructure properties of concrete that may influence the fracture process is presented below.

1.2 Microstructure of concrete

Based on different constituents, cementitious materials can be classified as paste, mortar or concrete. Paste is a mixture of cement and water. Mortar is a mixture of sand, cement and water. Concrete is composed of cement, sand, coarse aggregate and water. Other admixtures may be used to improve the properties of these constituents. In all these mixtures, cement acts as the binder material. It hydrates when mixed with water and forms a matrix. In the fluid form, this matrix fills the space between the aggregates and sand. After a certain period of curing, the cement matrix hardens and bonds together all constituents into the form of hardened concrete.

1.2.1 Microstructure of cement paste

Hydration products of cement primarily include C-S-H, C-H and ettringite. The C-S-H is a purely crystalline material, a principal hydration component that makes up about one-half to two-thirds of the volume of the hydrated paste. The C-S-H forms extremely small particles of size less than $1\mu m$ in any dimension (Figure 1.2). The C-H is a crystalline material and occupies about 20 to 25% of the paste volume. The C-H crystals have distinctive hexagonal prism morphology with typical crystal dimension ranging from 0.01 to 0.1mm. Ettringite usually crystallizes as long, slender prismatic needles, typically of 10 x 0.5μm, in the cement paste and makes up approximately 10 to15% by volume of the cement paste.

Porosity is another major component of the microstructure of the hardened cement paste. It is usually classified as gel porosity and capillary porosity. Gel porosity, ranging approximately from 0.5 to 10nm in size, can be regarded as part of the C-S-H, whereas the capillary porosity varying from 0.01 to $10\mu m$ in size can be seen as remnants of water filled spaces that exist between the partially hydrated cement grains. The volume of porosity decreases during hydration.

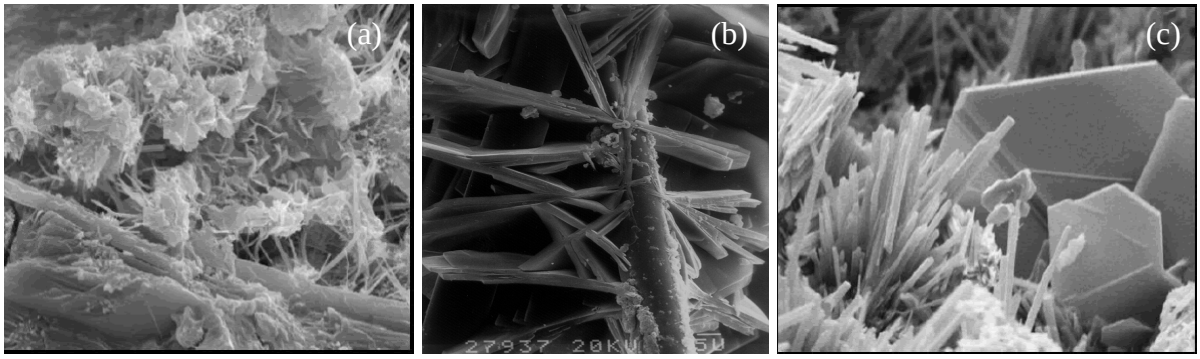

Figure 1.2 Electron microscopic images of (a) foil-like Calcium Silicate Hydrates, C-S-H and fine bundles of C-S-H fibres (b) c) Ettringite needles and plate-like C-H morphology (from [124]).

In the different models proposed in the literature to describe concrete microstructure, the C-S-H needles are of major importance. Many researchers believe that concrete structure is damaged during Scanning Electron Microscopy (SEM) preparation. Therefore, several of the structural models of the hardened cement paste are not directly derived from SEM observation only, but from other chemical and physical analysis techniques as well. Among several structural models proposed in the past, the best known are the models of Powers [101], Feldman [41] and Wittmann [133].

1.2.2 Aggregates, properties and particle distribution

Aggregates are generally about 75% of the total volume of concrete and therefore control many of its properties. Natural aggregates like limestone, quartz, basalt, granite etc are mostly in use. In addition to the natural aggregates, alternative materials can be also used, e.g. blast furnace slag, fly-ash, river gravel or lightweight by-products from industrial processes. The mechanical and other properties of these aggregates differ from those of natural aggregates e.g. density, water absorption and particle strength. The densities of such materials are very low due to high porosity, which has a significant effect on the flow of water at the matrix aggregate interface. Therefore, one must take care that a relevant correction of water cement ratio is made.

For a high strength concrete, aggregates like basalt or good quality limestone are recommended. In this case, balanced aggregate grading is very important in order to reduce the porosity of the material. Usually the different model codes contain detailed description of the aggregates grading that must be used in practice. Well graded aggregates not only decrease the porosity of concrete, but also have a significant effect on the amount of water in order to obtain certain workability. More water is absorbed over the surface of small sized aggregates. This means that more water must be added to obtain a given workability with fine grained aggregates than with coarse aggregates. The aggregate shape and

texture have also an important effect on the workability. Round, smooth aggregates generally give an improved workability.

Until now it has been assumed that in a concrete volume, the cement and aggregate particles are uniformly distributed. However, this may not be true, as concrete is generally cast in moulds and wall effects appear near the mould-concrete interface. Two types of such effects are generally observed. Firstly, the microstructural gradients appear at the casting surface where water is free to evaporate from the concrete [69]. Secondly, wall effect causes a rather different size distribution of aggregate particles in the part of concrete that are in contact with the mould. Many small particles fill the space between the larger aggregates and the mould. Usually the skin is also rich in cement content.

1.2.3 Interfacial properties between aggregates and cement paste

In most cases, concrete is considered as a two-phase material consisting of a cement paste matrix and aggregates. These two constituents are bonded together at the interface. For normal concrete, this interface is generally considered as the weakest link in the material; however, for concrete containing alternative aggregates or improved cement matrices, the interface might have different properties.

The strength of the interfacial transitional zone between cement matrix and aggregates has a significant effect on the global strength of concrete. Since bleeding or segregation normally occurs for fresh concrete, some cracks form at the interface between the matrix and the aggregates when the concrete is hardened. On the other hand, since the matrix and aggregates have different modulus of elasticity, thermal coefficients and response to change of moisture content, the interfacial transition zone between the matrix and the aggregates often has more voids and is weaker than the bulk cement matrix.

A structural model of the cement matrix-aggregate (rounded river gravel) interface is shown in Figure 1.3. The model is generally accepted and is based on the research carried out in [35, 79, 90]. It is assumed that a layer of C-H precipitates at the physical boundary between aggregates and cement matrix. It follows a layer containing C-H crystals, ettringite and C-S-H. This so called intermediate layer or interfacial transition zone has very high porosity and its thickness varies from 20 to 60μm for the concrete containing river gravels. A closer observation of the fracture surfaces has shown that fracture occurs not directly at the physical boundary but at the intermediate layer or the porous interfacial transition zone [136]. Using SEM in combination with image processing techniques, it is revealed that the weak transitional zone is due to an increased porosity close to aggregate surface and a reduced number of hydrated cement particles [112].

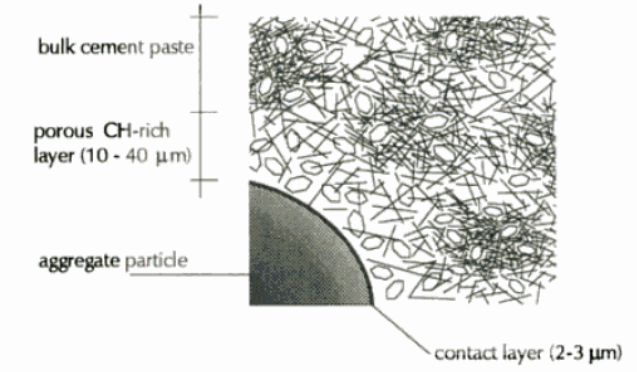

Figure 1.3 Structure of interfacial transition zone between rounded, dense, natural aggregate and Portland cement matrix (from [124]).

1.3 Fracture behaviour of concrete in tension

Failure of concrete is usually caused by the loss of material strength due to crack growth associated with microcracking. Concrete microstructure is very complex as the density, porosity and mechanical properties are not identical at each point within the sample, which induce stress concentrations when subjected to mechanical loadings. Microcracks start to develop from the weakest points or defects in the material structure. They make concrete highly weak in tension and its tensile strength approximately ranges from 8 to 15 % of its compressive strength. Various characteristics of cracking in concrete under tensile loadings are explained below.

1.3.1 Strain localization and softening behaviour

When concrete is subjected to tensile loading, strains are quickly localized in the weaker areas of the specimen. Li and co-workers [74, 75] examined a notch-less concrete plate under uni-axial tension (Figure 1.4). It can be seen that prior to point A, the specimen behaves elastically and the displacements measured from the four LVDTs are essentially the same and they increase linearly with the loading. For higher values of loading, the stress displacement relationship is no longer linear. After the peak load (point C), displacements from the three LVDTs decrease, while the displacement recorded by LVDT-4 continuously increases and the corresponding load decreases gradually (softening behaviour), (Figure 1.4(c)). Acoustic emission (AE) measurements indicate the initiation of internal cracks at point A which are uniformly distributed up to point B. After that point, the development of a narrow band of microcracks is detected near LVDT-4, indicating the onset of damage localization.

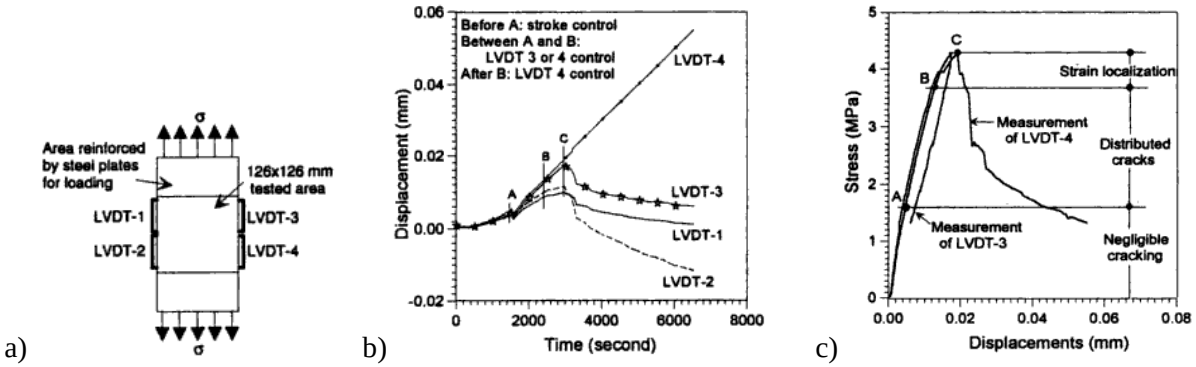

Figure 1.4 Concrete plate subjected to tension: (a) specimen geometry and arrangements of LVDTs, (b) relationships between displacements and time (c) stress-displacement relationship for four LVDTs (from [75]).

Other experiments [74, 75, 122, 125, 102] have shown that at the peak of the stress-deformation diagram, a macrocrack zone starts to develop and slowly transverses the whole cross-section of the specimen. In the post-peak regime, the residual load carrying capacity decreases with the propagation of the macrocrack. However, some residual carrying capacity remains, caused by toughening mechanisms as remnants of the non-uniform crack process (see Section 1.3.2 and 1.3.3).

In laboratory experiments, as the specimen has a finite size, such a load drop is observed and can be measured. For the case of a crack in an infinitely large plate subjected to far-field tension perpendicular to the crack, it is highly unlikely that softening would occur [127]. This is perhaps a theoretical case, but most classical fracture mechanics theories have been derived for cracks in infinitely plates. The use of finite dimensions leads to the introduction of a geometrical factor, which emphasizes the structural aspect of softening. Therefore, another school of thought is that softening is not a material property, but rather the outcome of a specific structure under certain boundary conditions loaded beyond its maximum carrying capacity [127].

In summary, tensile softening comprises of three distinct mechanisms: (1) the growth of microcracks that rapidly coalesce to a macrocrack (2) the progress of the macrocrack that gradually decreases the load carrying capacity of the specimen (3) toughening mechanisms that emanate due to the heterogeneous material structure and the randomly distributed material weaknesses.

The onset of localization is an important point in the fracture process. In different articles, localization is reported to occur at peak strength or just before the peak load [25, 102]. Both Cedolin and co-

workers [25] and Raiss and co-workers [102] adopted Moiré interferometry methods that allow for measuring the full-field strain distribution at the specimen surface. The experiments using AE techniques [70, 75, 94] have shown that AE events corresponding to damage localization begin to form well before the peak load (about 70 to 80 % of the peak load). Even at 30% of the peak load in the pre-peak regime, AE events are detected ahead of the notch.

1.3.2 Toughening mechanisms

Beyond the elastic range, strains localize into a zone known as the fracture process zone (FPZ) and are responsible for the softening behaviour (Figure 1.4). Different local toughening mechanisms occur in the fracture process zone:

- During fracture, the high-stress state near the crack tip causes microcracking at the weakest links. Such links result from water filled pores, air voids created during casting and shrinkage cracks due to the curing process. This phenomenon is known as *microcrack shielding* (Figure 1.5(a)) and consumes a part of the external energy received by the applied load.
- *Crack deflection* occurs when the path of least resistance is around a relatively strong aggregate particle or along a weak interface between cement matrix and aggregate (Figure 1.5(b)).
- Another important toughening process is *crack interface bridging* as shown in Figure 1.5(c). It occurs when the crack advances beyond an aggregate that continues to transmit stresses across the crack until it ruptures or is pulled out.
- Furthermore, during grain pullout or opening of a tortuous crack, there may be some contact or *interlock* between the cracked surfaces (Figure 1.5(d)). This causes energy dissipation through friction and crack interface bridging across the crack.
- It has been reported that crack tip is sometimes arrested by internal voids, which produces a blunt tip. This is called *crack tip blunting* by voids and is shown in Figure 1.5(e). Additional energy is required to propagate the crack with a new blunt tip.
- The final mechanism is *crack branching* (Figure 1.6(f)). The crack may propagate into several branches due to heterogeneity of concrete. More energy should be consumed to form new crack branches.

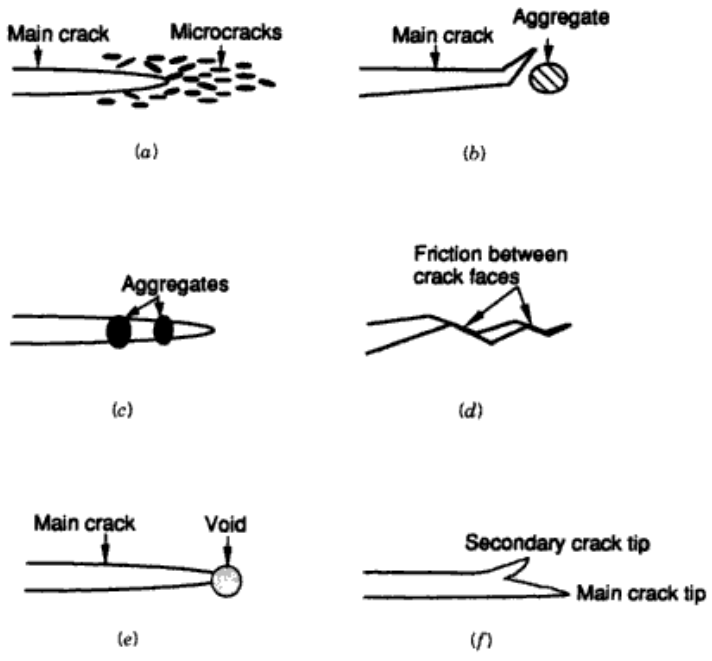

Figure 1.5 Toughening mechanisms in fracture process zone (a) crack shielding (b) crack deflection (c) crack or aggregate bridging (d) crack interlock sue to surface roughness (e) crack tip blunted by void (f) crack branching (from [114]).

The crack interface bridging is presented in detail hereafter.

1.3.3 Crack interface bridging

Van Mier [124] found that cracks in concrete are not continuous, but rather branch and overlap. This type of overlap is called *crack interface bridging*. Essentially the two crack surfaces are connected by a ligament between the overlapping crack tips, thus allowing for stress transfer between the crack surfaces. The overlap would fail if one of the crack tips propagates and coalesces in the wake of the second crack (Figure 1.6). Using microscopy studies it is found that the ligament between two overlapping crack tips fails gradually. This process is generally responsible for the tail of the softening diagram in the deformation controlled tension experiment. The mechanism is studied in detail for hardened cement paste in [126].

Figure 1.6 Stages of final rupture of the crack overlap (from [123]).

1.3.4 Characterization of the cracking process

Crack growth associated with microcracking is an important phenomenon for fracture or damage analysis and for the development of appropriate constitutive models for concrete. It varies with the size, distribution and type of the constituent materials and involves cracking at different scales (Section 1.1) [124]. It consists of main cracks with branches, secondary cracks and a micro fracture process zone ahead of the main cracks.

Mindess [91] used more than a dozen techniques to study the true mechanism taking place during tensile cracking. The estimation of crack size and the size of FPZ is varied according to the sensitivity of the measurement technique. He proposed that in fracture mechanics of concrete any crack with a width over $6\mu m$ should be termed macrocrack. Mihashi [86] considered that around the branches of the main crack there are closed microcracks (Figure 1.7) while opening microcracks exist in front of them. Another concept published by Hu and Wittmann [57] is shown in Figure 1.8. They separated an inner macrocracking zone from the isolated microcracking zone.

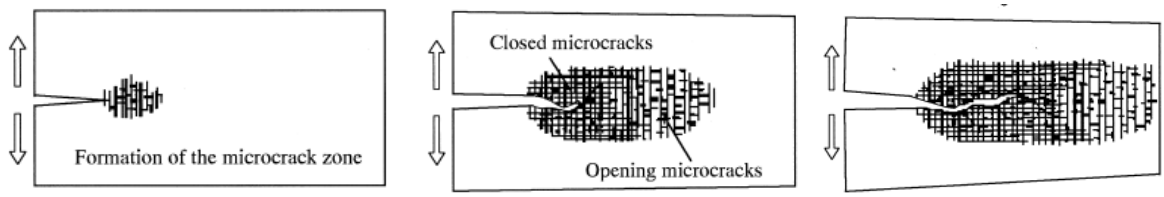

Figure 1.7 Concept of fracture process zone-1 (from [86]).

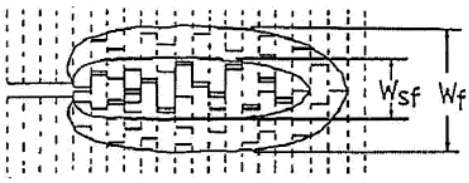

Wsf: Width of the inner zone with interacting microcrascks

Wf: Width of the inner zone in which isolated microcracking takes place

Figure 1.8 Concept of fracture process zone-2 (from [57]).

Distinction between micro and macrocracks could also be made based on the ability of the material to arrest the crack [127]. Obviously this is related to the degree of the heterogeneity and the scale of

observation (Section 1.1). Thus it can be assumed that microcracks can be stopped in local stress fluctuations caused by specific material structural elements like aggregates and pores; however, macrocracks are more energetic and cannot be arrested in these local stress fluctuations.

In a series of vacuum impregnation experiments and optical microscopy tests, the internal crack growth is monitored in notched concrete specimens subjected to uni-axial tension [125, 123]. However, this technique is limited to the detection of continuous macrocracks in contact with the outer surface of the specimen. The authors have found that cracks extend from the surface of the specimens into the interior, but do not connect. Cracking in the form of distributed microcracks occur near the vicinity of the notch at lower load levels, an indication of the existence of a microcracking zone before the macrocrack starts to propagate. The macrocrack extends way through the specimen but an intact core seems to remain. This internal core may contain distributed microcracks that cannot be detected with impregnation technique. At a load drop 60 to 70% of the peak load, around 80% of the cross-sectional area is cracked.

The observations from these experiments reveal the false assumption made in the continuum damage models which predict that at final stage, the full cross section of the specimen is cracked and load cannot be transferred. The fact is that at 100% cracked area, the specimen can still carry a certain load (e.g. 0.2 σ_{peak} for a concrete of maximum aggregate size of 16*mm* [123]). This clearly shows that other mechanisms are active allowing the stress transfer between the crack faces.

1.3.5 Size of fracture process zone

Both experimental and theoretical studies have shown that fracture process zone has to have a certain width and length to allow for the various toughening mechanisms [55, 124]. Its size relative to the structure size is of fundamental importance and is used as the basic assumption in the development of most numerical models. The width of the FPZ and its length ahead of the propagating macrocrack are generally assumed constant and are considered as material properties.

Otsuka [94] performed an experimental campaign using concrete specimens of different dimensions and aggregate sizes. Using X-ray and acoustic emission techniques he found that the width of FPZ increases with an increasing maximum aggregate size (d_a), however its length decreases (Figure 1.9(a)). However, in his paper the FPZ is considered as the whole zone ahead of the notch in which cumulative AE events are detected. This could be questionable, as FPZ should be measured ahead of the actual crack tip. The detection of the crack tip position is not doubt difficult but it can be measured using optical techniques [91].

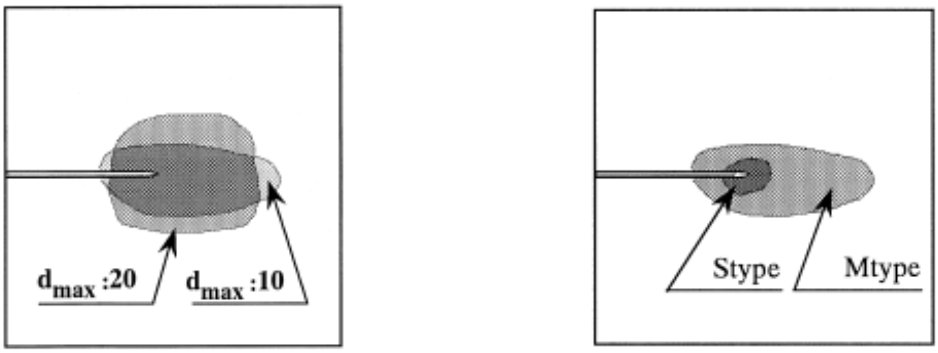

(a) (b)

Figure 1.9 Comparison of fracture process zone obtained with AE technique (from [94]) (a) Influence of aggregate size (mm), (b) Influence of specimen size.

It is also detected that the width of FPZ varies with the crack length relative to the specimen dimension. This effect is called as *the boundary effect on the FPZ*. Studies have shown that FPZ width decreases dramatically when FPZ approaches the back face of a notched concrete specimen. Hu and Wittmann performed a saw-cutting experiment on mortar and showed that the development of FPZ in a wedge splitting specimen is severely limited when specimen size or ligament length is reduced [57, 55]. When the ligament length (= specimen length - crack length) is small, the specimen dimension along the direction of the crack propagation can be divided into inner and outer regions. In the inner region, the growth of fracture process zone is not affected by the boundaries of the specimen and its size can be assumed as constant. When the crack reaches the outer region, the fracture process zone decreases due to the boundary influence [38].

1.4 Effect of aggregate size on fracture behaviour

The use of larger size of aggregates has long been considered a fundamental basis for an economic concrete mixture design. The reason behind this long accepted concept is straightforward. Concrete made with larger sizes of aggregates requires less mixing water [129]. The well established and almost universally accepted “water-cement ratio law” says that there should be an increase in strength consistent with the reduced amount of water.

Nevertheless, tests have shown that the size of coarse aggregates exerts an influence on concrete strength independently of the water cement ratio. For a given water cement ratio, strength increases as the maximum size of coarse aggregates is reduced. It seems probable that a point likely to be reached beyond which there is no strength advantage in using smaller sizes of aggregates and if size is further decreased, strength starts to decrease [129].

1.4.1 Effect on microcracking characteristics

Characteristics of microcracks are dependent on the degree of heterogeneity in the material. Fine-grained materials show different micro fracture characteristics than coarse grained materials. Landis and Shah [70] characterized microcracks according to their fracture mode. The fine grained materials show primarily a mixed-mode micro-fracture, whereas the coarse grained materials show a mode-II (shear) micro fracture.

A relationship between the microcracking characteristics and the overall fracture toughness of the material is established through quantitative AE analysis [70]. The AE source locations in the coarse mortar specimen shows significantly more scatter than the fine mortar, indicating a larger damage zone. The coarse mortar has a higher overall toughness, attesting to the fact that diffused damage leads to greater energy absorption capacity.

The enhancement of fracture properties of concrete due to large aggregate particles can be explained by microcrack shielding and crack bridging (see Section 1.3.2), which cause the reduction of stress in the FPZ. Also, the interlocking of the particles between the crack surfaces consumes energy and thus enhances the fracture resistance [135]. For smaller d_a especially in the mortar, the fracture surface is smooth. For higher d_a, surface becomes rough and complex, and also some coarse aggregates are found snapped [2, 135]. As crack meets an aggregate particle, it is forced either to propagate through the tougher aggregate or to deflect and travel around the aggregate-mortar interface. Since the interface toughness is usually lower than the matrix, the advancing crack tip is prone to deflect the aggregate, resulting in a tortuous cracking path and needs more energy. Thus, larger the size of aggregates is, the more tortuous cracking path would be and higher energy will be required to overcome the interfacial bond.

The potential of the fractal geometry as means of describing the scaling of surface roughness has been explored by many researchers [8, 78]. Mandelbrot and co-workers [78] were the first to suggest a link between fractal dimension of fracture surface and fracture toughness. Since the roughness of the cracked surface may play the important role of the intrinsic parameter at the microstructure level, the roughness of the fractured surface and the fractal theory have been used to quantitatively characterize the coarseness of internal structure of concrete. It has been proven experimentally [119, 94, 27] that the size of the FPZ in concrete increases with increasing average aggregate size. From this point of view, the coarseness of grain structure of concrete should be considered as one of the dominant parameters affecting the size of the FPZ.

1.4.2 Effect on brittleness and fracture energy

When FPZ is small, the failure pattern is more brittle and towards the region of LEFM, which is manifested as the shift to the right side on the size effect plot (see Figure 1.11). Such shift was obtained in the study of Chang and co-workers [26] and Amparano and co-workers [2]. In their studies the size of the aggregates and their volume fraction are the experimental parameters respectively. In the study of Chang and co-workers [26] the test data for concrete with large aggregate (and thus coarse internal structure) falls in the transition zone between LEFM and the strength criterion; while the test data of cement pastes with small aggregates (and thus fine internal structure) shifts to the right. From a LEFM point of view, this means that a cement paste is more brittle than concrete, and can be characterized by LEFM.

The fracture parameters also depend on the aggregate size. It was shown that both fracture toughness and fracture energy increase with an increase of the maximum aggregate size, with a fixed value of aggregate content [27]. Kleinschrodt and Winkler [67] reported that the influence of d_a is probably insensitive to fracture energy while Mihashi and co-workers [88] showed that the influence is significant. As the aggregate size became larger, the values of fracture energy and AE hits significantly increased.

The volume content of aggregates (V_{agg}) is also an important parameter. Higher volume fraction of aggregates leads to a finer grain structure, and thus to a small size FPZ [2]. The article concludes that the fracture properties of concrete depend strongly on the total aggregate content. The fracture energy exhibits variations in the range of 25%: fracture energy decreases with an increasing aggregate content and reaches a minimum value by V_{agg} = 65%, then starts to increase (but there is no such critical volume fraction which gives maximum G_f). The size of the FPZ decreases with increasing content of aggregates, something that can be explained by the change of coarseness of grain structure defined in terms of mosaic patterns [2]. The nominal strength of concrete beams shifts from the left to the right in the size effect curve with an increasing volume fraction of aggregates. In other words, the failure mechanisms of the concrete used in the study shift toward the region of linear elastic fracture mechanics.

1.5 Size effect on strength of concrete structures

Size effect is the change of response of a material due to geometrical changes in the dimensions of the structure. In solid mechanics, the scaling problem of main interest is the effect of size of the structure on its strength. Emphasis is placed on quasi-brittle materials, for which the problem is most acute and

complex. These are materials incapable of plastic yielding, failing due to fracture characterized by a large FPZ that undergo distributed strain-softening in the form of micro-cracking and fractional slip. The mechanism of size effect is mainly deterministic, involving stress redistribution and the release of stored energy engendered by a large fracture or a large FPZ.

Experimental results have indicated that the strength of concrete usually decreases with increasing size of structures. The size effect on concrete may be primarily explained by the FPZ. When a concrete structure is loaded, the strain energy produced by the applied load is converted to the energy consumed to create a new fracture surface and the energy absorbed in the FPZ (due to toughening mechanisms). For large-size structures that have long ligament lengths on crack sections, the latter is negligible compared to the former, whereas for small size structures the latter can be of the same magnitude as the former. Therefore, the larger the structure's size, the lower the nominal strength. However, the concrete strength approaches a constant when the size of the structure becomes very large [10].

1.5.1 Size effect theories

In concrete structures, size effect theories are mainly divided into three categories:

- Statistical theory of random strength [131].
- Theory of crack fractality [24].
- Deterministic or energetic size effect [7].

Statistical theory of random strength

The statistical theory of size effect began to emerge after Peirce [96] formulated the weakest-link model for a chain and introduced the extreme value statistics originated by Tippett [120], Fréchet [44] and Fisher and Tippett [43]. The capstone of the statistical theory of strength was laid by Weibull [131]. A three dimensional continuous generalization of the weakest link model for the failure of a chain of links of random strength leads to the distribution [131]:

$$P_f(\sigma_N) = 1 - \exp\left[-\int_V c[\sigma(x), \sigma_N]dV(x)\right] \tag{1.1}$$

which represents the probability P_f that a structure fails as soon as a macroscopic fracture initiates from a microcrack (or flaw) somewhere in the structure; σ = stress tensor field induced by the load that corresponds to the nominal strength σ_N, x = coordinate vector, V = volume of structure and $c(\sigma)$ = a function giving the spatial concentration of the failure probability of the material.

Applications of Weibull's theory to fatigue embrittled metals and to ceramics have been researched thoroughly. Applications to concrete, where the size effect has been of the greatest concern, have been studied by Mihashi and Izumi [87], Mihashi [85], Wittmann and Zaitsev [134], Carpinteri [23] and others. Based on some serious limitations e.g. absence of material characteristic length, no information on structural geometry, negligence of spatial correlations of material failure probabilities of neighbouring elements caused by non local properties of the damage evolution, the theory appears applicable to some extremely thick plain (unreinforced) structures [14].

Theory of crack fractality

Observations have shown that the fracture surfaces in concrete exhibit partly fractal characteristics. Recent advances in the study of the fractal aspects of crack morphology and energy dissipation by fractal cracks have shown a correlation between the fractal dimension of the crack surface and the fracture energy of concrete materials. In [24] a size effect theory is proposed called *multi fractal scaling law* (MFSL) showing that a fractal nature can be the physical origin of the size effects observed on the concrete structures. For failures occurring at fracture initiation from a smooth surface, the scaling law reads:

$$\sigma_N = \sqrt{A_1 + \frac{A_2}{D}} \tag{1.2}$$

Where A_1, A_2 = constants depending upon the fractal nature of the crack.

There are, however, few objects to the fractal theory [9]:

- A mechanical analysis of fractal nature of cracks predicts a different size effect than Equation 1.2.
- The fractality of the final fracture surface should not matter, because typically a major amount of energy is dissipated by microcracks and fractional slips on the sides of this surface.
- The fractal theory does not predict how $A_1$and A_2 should depend on the geometry of the structure.

Deterministic or energetic size effect

Application of LEFM to concrete was first considered by Kaplan [63] but subsequent test results showed significant disagreements [66, 72, 130]. Leicester [72] conducted tests of geometrically similar notched beams of different sizes, fitted the results by a power-type size effect, and observed that the optimum exponent was greater than $-1/2$, the value required by LEFM. He tried to explain it by noting that the strength of the stress singularity for sharp notches of a finite angle is less than that for sharp cracks. This explanation however is questionable because notches of a finite angle cannot

propagate, and because the singular stress field of notches of a finite angle gives a zero energy flux into the notch tip. Besides, Leicester's power law for size effect implied nonexistence of a characteristic length. Based on more extensive tests of geometrically similar notched beams of different sizes, Walsh [130] was the first to make the doubly logarithmic plot of nominal strength versus size and note that it appears to be transitional between plasticity and LEFM, although he did not attempt to make a mathematical analysis and obtain a formula.

A different type of quasi-brittle size effect was brought to light by Hillerborg and co-workers [51] who extended the models of Barenblatt [4] and Dugdale [39] to formulate the cohesive (or fictitious) crack model for concrete characterized by a softening stress-crack opening law. Using finite element analysis, they showed that the failures of plain concrete beams exhibit a deterministic size effect, which agrees with the test data on the maximum peak load obtained from Brazilian tests.

Bazant's size effect law

In 1976 it was analytically demonstrated that localization of strains engenders a size effect on post-peak deflections and energy dissipation of structures [6]. Inspired from the work of Hillerborg [51] and using the energy release rate concept, Bazant [7] derived a size effect law which describes the size effect on nominal strength of quasi-brittle structures containing notches or traction-free (fatigued) large cracks that have formed in a stable manner. Measurement of the size effect on the maximum load of notched specimens are shown to provide simple means for determining the fracture energy and effective length of the FPZ and are embodied in a standard RILEM Recommendations [107].

According to Bazant's size effect law, introduction of a crack with a FPZ of fixed width *h* at peak load causes the release of strain energy from the shaded triangles on the flanks of the crack band shown in Figure 1.10. The slope *k* of the effective boundary of the stress-relief zone is considered independent of the size *D* of the specimen. The length of the crack at maximum load, called hereafter *a*, is assumed proportional to *D*, while the width *h* of the FPZ is essentially a constant, related to the in-homogeneity size in the material. Subsequently, using an approximate energy release analysis, the following approximate size effect law is derived [7] for the quasi-brittle size effect in structures failing after large stable crack growth:

$$\sigma_N = Bf_t'\left(1+\frac{D}{D_0}\right)^{-1/2} \tag{1.3}$$

Where σ_N = nominal strength; D = characteristic size of the structure; B and D_0 = parameters depending on structural geometry and ft' = the material tensile strength.

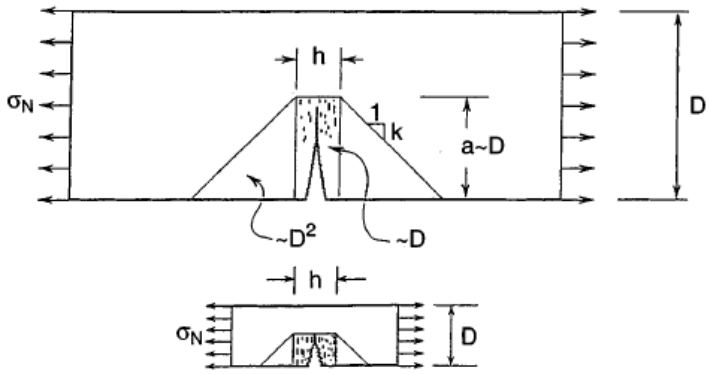

Figure 1.10 Zones of stress relief according Bazant's size effect law (from [7]).

It is important to note that according to Bazant's size effect law, stress reduction in the triangular zones of area $ka^2/2$ (Figure. 1.10) causes an energy release $U_a = 2(ka^2/2)\sigma_N^2/2E$ (E being the Young's modulus). The stress drop within the crack band of width h causes further energy release $U_b = ha\sigma_N^2/2E$. The total energy dissipated by fracture is $W = aG_f$, where G_f is the fracture energy, a material property representing the energy dissipated per unit fracture length. Energy balance during static failure requires that $\partial(U_a+U_b)/\partial a = dW / da$. Setting $a = D(a/D)$, where a/D assumed constant for structures with geometrically similar sizes, the solution of the last equation for σ_N yields Bazant's approximate size effect law (Equation 1.3).

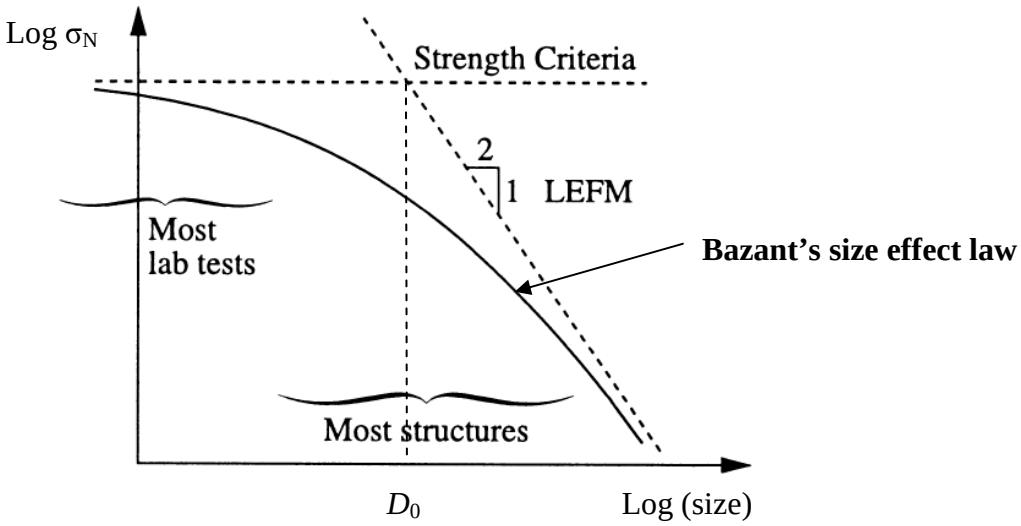

Figure 1.11 Transitional scaling of quasi brittle structures (from [14]).

More rigorous derivations of this law, applicable to arbitrary structure geometries, have been given in terms of asymptotic analysis based on equivalent LEFM [14]. The application of Bazant's size effect law to predict the size effect on peak strength of concrete beams has been verified experimentally,

among which the earliest is found in the famous Walsh's tests of notched concrete beams [130]. For very large sizes ($D >> D_0$), the size effect law (Equation 1.3) reduces to the power law $\sigma_N \propto D^{-1/2}$, which represents the size effect of LEFM (for geometrically similar large cracks) and corresponds to the inclined asymptote of slope -1/2 in Figure 1.11. For very small sizes ($D << D_0$), this law reduces to σ_N = constant, which corresponds to the horizontal asymptote and means that there is no size effect, as in plastic limit analysis.

1.5.2 Brittleness number

Brittleness number is defined as the non-dimensional characteristic that indicates whether the behaviour of a given specimen or structure is closer to a strength limit analysis or to LEFM. The relative structure size $\lambda = D/d_a$ cannot serve as an objective indicator of this behaviour. Bazant and co-workers [12] proposed that an objective indicator can be the brittleness number defined as:

$$\beta = \frac{D}{\lambda_0 \, d_a} \tag{1.4}$$

The value of $\beta = 1$ indicates that the specimen is at the centre of the transition between the two elementary failure criteria i.e. the point where the horizontal asymptote for the strength criterion intersects the inclined straight line asymptote of the LEFM criterion. For $\beta \leq 0.1$, the plastic limit analysis can be used as an approximation and for $\beta \geq 10$, linear elastic fracture mechanics may be used as an approximation.

λ_0 represents the value D / d_a for $\beta = 1$ and can be calculated by finding the structural strength σ_N simultaneously using a plastic limit analysis and LEFM analysis. By equating both equations for σ_N, Bazant obtained the following expression for the transition value D_0 of the characteristic dimension D of the structure at the transitional point (see Figure 1.11).

$$D_0 = \frac{G_f E}{f_t'^{\,2} B^2 g_f(\alpha_0)}, \qquad \lambda_0 = \frac{D_0}{d_a} \tag{1.5}$$

Therefore,

$$\beta = B^2 g_f(\alpha_0) \frac{f_t'^{\,2} D}{G_f E} \tag{1.6}$$

Where α_0 = relative crack length at the transition point = a_0 / D_0; $g_f(\alpha_0)$ = non-dimensional energy release rate calculated according to LEFM; G_f is the fracture energy corresponding to of an infinitely large specimen (under the condition that failure of an infinitely large specimen must follow linear elastic fracture mechanics).

1.5.3 Size effect on fracture energy and softening curve

Many numerical models can be found in literature to calculate fracture energy as a material property. Three of these models have been adopted by RILEM to determine experimentally the fracture energy: the Fictitious crack model [51], the Two parameter model [61] and the Size effect Model [7]. The details of the RILEM methods are presented in Section 2.2.

In the Fictitious crack model, the fracture energy for a specimen of height *D* and an initial notch (or crack) length *a* is calculated as the area under the tensile softening or cohesive stress-crack opening (σ~w) diagram. This definition of fracture energy would lead to different values if the ligament length/size ((*D*-*a*)/*D*) ratio is varied. This variation has been reported widely in the literature [38, 37, 36]. Van Mier [127] argued that a gradual post-peak load drop (or softening curve) is generally observed when testing specimens of finite dimensions, but is highly unlikely to happen for cracks in infinite plates (where material behaviour is brittle and follows LEFM law). Therefore, the softening or cohesive stress-crack opening (σ~w) diagram should be considered as an outcome of loading of a specific structure under specific boundary conditions.

The size effect law proposed by Bazant [7] is based on the assumption that the FPZ size and fracture energy are independent of the structural size and geometry. Bazant assumed that the FPZ size is not negligible and for laboratory-size fracture specimens, the fracture process zone is of the same order of magnitude as the specimen size. Furthermore, he assumed that due to the limited plasticity of concrete under tensile loadings, the hardening nonlinear zone surrounding the fracture process zone is rather small and the boundary of this nonlinear zone lies very close to the boundary of the fracture process zone. Therefore, and in order to isolate the boundary effects, an extrapolation to an infinite specimen size is made and thus the fracture process zone becomes infinitely small compared to the specimen. Under this condition the failure of an infinitely large specimen can be modelled with a linear elastic fracture mechanics law. Based on this hypothesis and using a dimensional analysis of energy release rate for linear elastic materials, Bazant calculated the fracture energy of concrete as:

$$G_f = \frac{g_f(\alpha_0)}{A\ E} \tag{1.7}$$

where A = slope of the linear regression plot between nominal strength, σ_N and square of specimen dimension, D for failure of geometrically similar specimens according to Bazant's size effect law (Equation 1.3).

It is very important to mention here that Bazant's size effect law is based on two main assumptions (1) the size (width) of the FPZ ahead of the crack at peak load is constant and (2) the crack length at peak load is proportional to the specimen size i.e. α_0 is a constant. The critical stage or unstable crack propagation is assumed to occur at peak load. An extrapolation to an infinite size of specimen is made to apply LEFM and then the critical strain energy release rate is calculated according to equivalent LEFM analysis for an infinite size of the specimen with proportional crack size.

1.5.4 Boundary effect on fracture properties

Hu and Wittmann [54, 56] examined the fracture of a large plate with an edge crack and pointed out that failure transition from strength dominated failure to the LEFM controlled fracture was due to the interactions between crack, fracture process zone and boundary, which lead to the common size effect. They performed a saw cutting experiment on mortar and showed that the development of FPZ in a wedge splitting specimen was severely limited when specimen size or ligament length was reduced [57]. They also showed that the FPZ width decreases dramatically when the FPZ reaches the back face of the notched concrete specimen.

In the following explanation of the non constant fracture energy, G_F is used exclusively for the size independent fracture energy and G_f is for the size dependent fracture energy. Considered the important role of fracture process zone size (or width) in fracture energy dissipation, Duan and co-workers [38, 37, 36] proposed a local fracture energy (G_f^*) model, in which $G_f^*(x)$ is assumed related only to the cohesive $\sigma(w)$ relationship [51] at one particular location (x) along the crack path. A bilinear function is used to induce the boundary effect on G_f^* (see Figure 1.12). The bilinear function consists of a horizontal length with a constant value of value of G_f* (or G_F) (within the region where FPZ length/width is maximum and essentially a constant) and a descending line that reduces to zero at the back surface of the specimen (the region where FPZ length/width is restricted due to boundary influence). For a specimen with ligament length (D-a) longer than the transitional ligament length (a_l*) (see Figure 1.12), the local fracture energy is given as:

$$G_f^*(x) = \begin{cases} G_F & x < D - a - a_l^* \\ G_F (D - a - x)/a_l^* & x \geq D - a - a_l^* \end{cases} \tag{1.8}$$

Subsequently, the size dependent fracture energy G_f in terms of the relative crack length (a/D) is obtained as:

$$G_f(\frac{a}{D}) = \begin{cases} G_F\left(1-\frac{1}{2}\left(\frac{a_l^*/D}{1-a/D}\right)\right) & 1-a/W > a_l^*/W \\ G_F\,\frac{1}{2}\left(\frac{(1-a/W)}{a_l^*/W}\right) & 1-a/W \le a_l^*/W \end{cases} \tag{1.9}$$

A representation of the changes in local fracture energy g_f and the size dependent fracture energy G_f are illustrated in Figure 1.12.

A size effect solution is proposed in [36, 56] to describe the dependence of specimen's nominal strength σ_N on the crack length a.

$$\sigma_N = \frac{f_t}{\sqrt{1+a/a_\infty^*}} \tag{1.10}$$

Where a^*_∞ is defined by the intersection of the maximum tensile stress and the LEFM criterion and is referred to as the reference crack size.

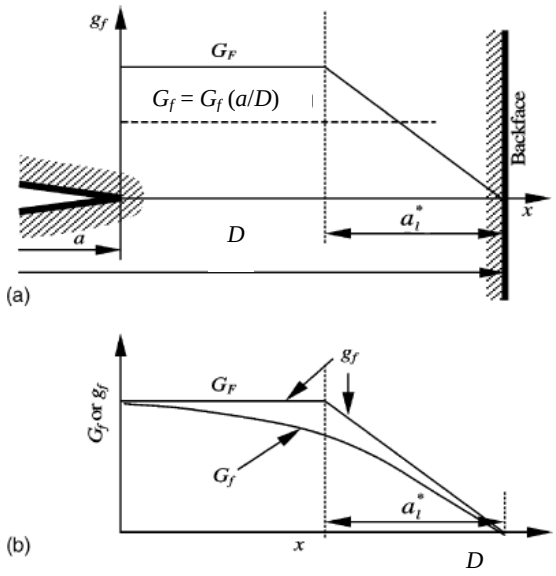

Figure 1.12 The distribution of fracture energy (G_f and g_f) along the ligament of a specimen (from [36, 56]).

In order to summarize the boundary effect on fracture (Figure 1.12), the physical size of a specimen alone is not sufficient to characterize the size effect on laboratory-size specimens. Boundary effect (thus another level of size effect) exists on the fracture properties if the $(D-a) \leq a_l^*$ even if $D >> a_l^*$ .This clearly demonstrates the significance of crack length in the size effect of concrete fracture.

Conclusion

When concrete is subjected to loadings, cracking usually initiates from the weakest links in the material microstructure. Under tensile loadings, the fracture process is characterized by strain localization and results in the post-peak softening of the stress-strain diagram. Many toughening mechanisms are responsible for the strain localization and additional energy is consumed during such mechanisms.

Cracking can be discretized into main cracks, secondary cracks and microcracks ahead of the main and secondary cracks. Different theories are available in literature to differentiate the different cracking zones (Section 1.3.4). However, the inner cracking zone (or the fracture process zone) associated with the main crack is more energetic and is responsible for the decrease in the load bearing capacity of a concrete structure.

The size of the fracture process zone is of fundamental importance and is considered as a material parameter in most numerical models. Recent experimental studies have shown that the size of the fracture process zone varies with the specimen size as well as the aggregate size (Section 1.3.5, 1.4). A boundary effect is also observed when the fracture process zone approaches the boundary of the specimen.

Experimental studies have shown that a size effect is present on the strength of concrete. Different theories exist in the literature (Section 1.5.1), among which the deterministic energetic size effect theory is most appealing. In this case, the decrease of the nominal strength while increasing the size of the structure is attributed to the growth of the fracture process zone of significant size. In Bazant's size effect law [7], a size independent fracture energy is considered and it is assumed that at peak load the crack length is proportional to the size of the specimen and the width of the fracture process zone is a material parameter (Section 1.5.1.3, 1.5.3). However, Duan and co-workers [38, 37, 36] propose a non constant fracture energy model (Section 1.5.4) based on the experimental observation of a boundary effect on the size of fracture process zone.

Chapter 2

Experimental Approach to Characterize Fracture in Concrete: Theoretical Background and Methodology

Different experimental techniques have been developed to measure fracture in concrete structures. The main purpose of these techniques is to study the fracture process zone (FPZ), the deformation contours and the crack path. Among the different experimental methods to estimate intrinsic fracture properties, RILEM (International Union of Laboratories and Experts in Construction Materials, Systems and Structures) has developed various testing procedures and recommendations based on simple mechanical tests.

This chapter is dedicated to present the procedures, techniques and protocols adopted in this study in order to characterize the fracture in concrete.

- In the first section, the Digital Image Correlation technique and its application as a fracture measuring tool are discussed.
- In the second section, the RILEM recommended test methods to measure fracture parameters of concrete are presented briefly, including the size effect method which is adopted in this study. The merits and demerits of these methods are discussed.
- In the third section, details on the experimental campaign performed in *GeM* at *Ecole Centrale de Nantes* in order to characterize fracture are presented (e.g. material aspects, specimen preparation, experimental setup, loading system).
- The last section is dedicated to the difficulties encountered in the preparation of the concrete specimens and the shortcomings of the mechanical testing equipment used in this study.

2.1 Digital Image Correlation as a fracture measuring tool

2.1.1 Introduction

In material testing, monitoring the geometrical changes of the test specimens is required to study the behaviour of the structural elements and also to validate constitutive models. Displacement and deformation measurements are typically measured by displacement transducers or strain gauges. These devices have been used extensively in the past, providing online results with sufficient precision and reliability (under certain conditions). A general disadvantage of these techniques, however, is their point wise nature and (often) one-dimensional measurement capability. If simultaneous two- or three-dimensional measurements at several locations are required, the instrumental effort quickly becomes rather important. In other words, these techniques are generally not suited for tasks requiring a large number of measurement points distributed over an object surface or for complete surface measurements. For these cases, techniques based on digital photogrammetry are a valuable alternative as a powerful and flexible measurement tool. Data processing can be highly automated and fast, limited only by the camera image rate.

A very popular photogrammetric technique known as Digital Image Correlation (DIC) has been validated theoretically and experimentally by many researchers [21, 29, 76]. In contrast to the more traditional methods it is a robust technique, which has a high degree of measurement accuracy and is much easier to apply experimentally. DIC requires minimal or no surface preparation and provides surface displacement data as a primary output. It is now well known that digital images of the deformed objects can be analyzed to estimate the in-plane displacements of various points on the surface of a specimen. Continuum mechanics theory is adopted to calculate deformations from surface displacements. Some specific properties of DIC that make it extremely attractive in the field of experimental mechanics are [109]:

- Optical digital image acquisition equipment, from CCD (Charged Coupled Device) to CMOS (Complementary Metal Oxide Semiconductor) sensor based cameras, are available with increasing quality and decreasing cost. Nowadays, the resolution (number of pixels) reaches 10 Mega pixels.
- Image acquisition is a non-contact technique, tolerating a large distance between the samples and the camera even for large magnifications. This non-contact character makes it suitable for unfriendly environments (high temperatures and humid or corrosive atmosphere).
- Fast digital cameras provide images with a high frequency (from about 10^4 to 10^6 frames per second) and thus open the way to detailed analyses of dynamic tests.

- DIC requires minimal or no surface preparation. The image surface under analysis has to be patterned. This pattern can be the natural surface of the specimen if it is textured and opaque enough (e.g., concrete, raw surface of ceramic). Otherwise, paints can be sprayed easily on the surface to provide the required texture without affecting the mechanical behaviour.
- Basic DIC dealing with image pairs only analyzes in-plane displacements. However, using two (or more) cameras provides the relevant information for the extraction of full three dimensional displacement fields of the surface of the solid. This technique is called "stereo correlation" and is useful for experiments where out-of-plane displacements are required e.g. compression tests on cylindrical specimens.
- A typical full field measurement of the displacements using DIC contains a considerable amount of data compared with classical instruments available on universal testing machines (e.g., extensometers, strain gauges). This can be useful to validate and identify constitutive laws.

2.1.2 Principles of Planar Digital Image Correlation

The process of correlation consists of analyzing a series of images of the specimen surface having a distributed grey level pattern. These patterns are monitored during the load application by a digital camera and stored in a computer in a digital format. Displacements fields can be measured by matching the first image (or the reference image, typically corresponding to the unloaded stage) and each subsequent image. However, when displacement amplitudes are too large, the consecutive pairs of images are generally matched to measure the elementary displacement field. In the latter case, the displacement field from the reference image is constructed as a sum of the elementary displacements, taking into account the non-linearity induced by the large displacements.

During the imaging process, the intensity of the random pattern is transformed into a finite number of samples on a rectangular grid. Each sensor, or pixel, in a typical camera averages the incident light intensity in the form of a grey intensity value, which is in the range of 0 to 256. Thus, a digital image is represented as a simple scalar valued number (gray level) at each pixel, and is denoted $f(x)$. The x argument is discretized into elementary pixels, usually in two dimensions, along a regular square grid (the pixel matrix). For optimal results, the image texture should be a rapid varying field with sharp contrast. An adequate speckle pattern must have a considerable quantity of black speckles with different shapes and sizes (Figure 2.1). The effectiveness of the speckle pattern can be determined by the quantity of pixels per black speckle. A good speckle pattern should have small black speckles (10 pixels), medium black speckles (20 pixels) and large black speckles (30 pixels) (the above quantity of pixels per speckles is approximated).

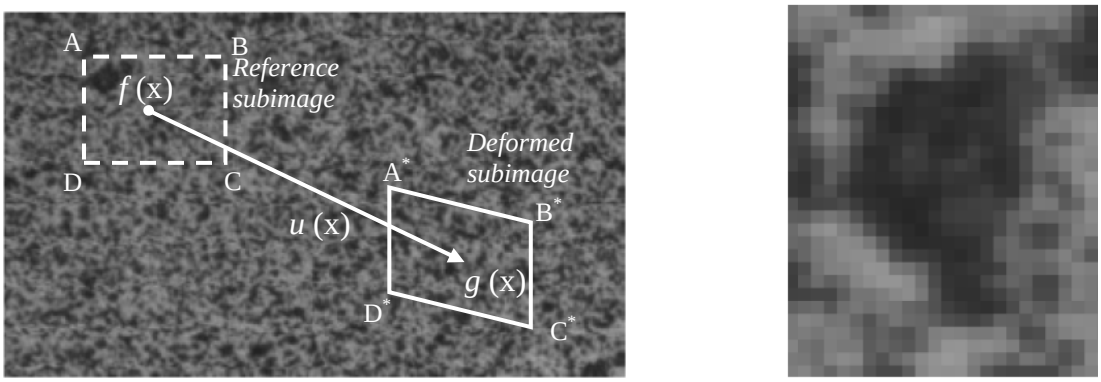

a) (b)

Figure 2.1 (a) Schematic representation of the deformed and reference subimages located on an instantaneous image (b) A medium black speckle pattern zoomed. The speckle pattern is approximately 15 pixels wide and 20 pixels high.

The basic principle underlying DIC is that each image is deformed only by the in-plane displacement field u, without any alteration of the gray levels. Thus, the reference and deformed images can be related by:

$$g(x) = f(x+u(x)) \tag{2.1}$$

Here g is the gray level of the deformed image. This equation is often termed as the brightness conservation equation. It does not take into account the topography of the surface. Hence, it can be modified to consider out-of-plane displacements.

Furthermore, the image acquisition is never perfect and always contains a small amount of noise, so that

$$g(x) = f(x+u(x)) + \eta(x) \tag{2.2}$$

Where η is the noise amplitude.

During an experiment, the illumination of the image window can change (e.g. affine change in gray levels). To improve the results, the gray level offset b and rescaling a parameters have to be determined in addition to the displacement unknowns.

$$g(x) = [(1+a(x))\, f(x + u(x))] + \eta(x) + b(x) \tag{2.3}$$

The *a* and *b* coefficients of brightness conservation are often ignored in order to make the algorithm more robust [109].

To account for subpixel movement, it is necessary to specify an interpolation scheme (Figure 2.2). The most elementary is the linear interpolation scheme which consists of assigning a combination of four functions (1, *x*, *y* and *xy*) at each square of pixels in order to match the subpixel gray values. This interpolation scheme gives satisfactory results even if it provides discontinuous derivatives across edges and at the nodes of the pixel matrix. Higher order interpolation schemes (cubic, quintic spline functions) are also in use. They typically improve the results (eliminate errors like lens distortions, vibrations, periodic bias [117, 28]) usually at the expense of longer computation times. Another choice is given by the Fourier decomposition of the original image that naturally provides a continuous field with infinite differentiability, and yet a small computational cost. The main difficulty of this choice, however, is the aliasing effect of non-periodic boundary conditions on the edge of images or subimages [109].

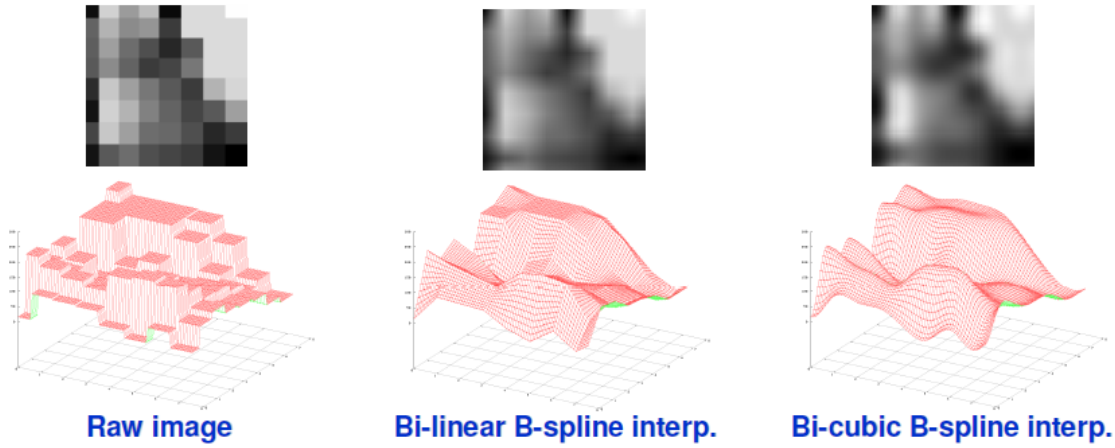

Figure 2.2 Representation of interpolation schemes used in correlation of digital images.

An additional improvement consists of restricting the variability of the displacement field. This regularization is usually defined considering that $u(x)$ is piecewise constant or linearly varying with x over zones, allowing for arbitrary discontinuities across zone boundaries. The extension of these zones referred to as “correlation zones” thus qualifies the quality of regularization. Other than linear variability, choices like imposing a global continuity for u through decomposition over classical finite element shape functions, or extended shape functions suitable for cracks [93, 110], one may benefit from a prior knowledge of the analytical displacement fields. Such regularization can be made using specific choices of the basis function $\psi_n(x)$.

$$u(x) = \sum_n \omega_n \psi_n(x) \tag{2.4}$$

Because of the above image imperfections, or simply because the actual displacement field is not exactly part of the chosen subspace, the brightness conservation cannot be exactly fulfilled. Thus, an iterative approach known as correlation is used by minimizing a functional Φ in the space ω_n of the correlation zone. The following criteria can be used for the minimization:

- Sum of Squared Differences criterion (SSD)

$$\Phi^2(\omega_n) = \int \left[g(x) - f\left(x + \sum_n \omega_n \psi_n(x) \right) \right]^2 dx \tag{2.5}$$

- Zero mean Sum of Squared Differences criterion (ZSSD)

$$\Phi^2(\omega_n) = \int \left[\left(g(x) - \overline{g}\right) - \left(f\left(x + \sum_n \omega_n \psi_n(x) \right) - \overline{f} \right) \right]^2 dx \tag{2.6}$$

Where $\overline{g}$ and $\overline{f}$ are the average grey levels over the domain of correlation in the deformed and reference images respectively.

When ψ is constant over the correlation zone ω_n, minimizing Φ^2 is equivalent to maximizing the cross-correlation coefficient $C(\omega_n)$ between *f* and *g* over this zone.

$$C(\omega_n) = \int g(x) f\left(x + \sum_n \omega_n \psi_n(x) \right) dx \tag{2.7}$$

The displacement which maximizes the above product corresponds to the estimation of the unknown displacement vector *u*(*x*). It can be computed in the reference space or in a Fourier space. A polynomial fit of the cross-correlation function allows locating its maximum with subpixel resolution. The advantage of this formulation is that a global search for the maximum is easy to perform and hence this technique is also suitable to large displacements. The following two criteria can be used for maximizing $C(\omega_n)$:

- Normalized Cross-Correlation criterion (NCC)

$$C(\omega_n) = \frac{\int g(x) f\left(x + \sum_n \omega_n \psi_n(x)\right) dx}{\sqrt{\int (g(x))^2 dx \int \left(f\left(x + \sum_n \omega_n \psi_n(x)\right)\right)^2 dx}} \tag{2.8}$$

- Zero mean Normalized Cross-Correlation criterion (ZNCC)

$$C(\omega_n) = \frac{\int \left(g(x) - \overline{g}\right)\left(f\left(x + \sum_n \omega_n \psi_n(x)\right) - \overline{f}\right) dx}{\sqrt{\int \left(g(x) - \overline{g}\right)^2 dx \int \left(f\left(x + \sum_n \omega_n \psi_n(x)\right) - \overline{f}\right)^2 dx}} \tag{2.9}$$

2.1.3 Overview of DIC application in fracture measurements

DIC has been established as a stable and reliable tool for damage and fracture measurements [28, 114]. In [28] DIC is used in concrete compression tests to detect cracks and to measure strains. The authors estimated the accuracy of the displacement measurements using three different procedures and the maximum error was about 1/20 pixels.

The possible error sources may be due to lens distortions, vibrations, or periodic bias in measured displacements. When cracks form in a concrete specimen, the pixels near the crack may rotate. Since displacement measurements are based on the transitional shift of images, rotation can affect the results to a small extent. Local discrepancies (e.g. cracks) can also significantly decrease the magnitude of the coefficient of correlation. Thus, the acceptable level of the correlation coefficient should be set higher in order to have precise estimations [28]. Lawler and co-workers [71] reported that single surface information by DIC may not reflect the behaviour of the remaining surfaces or the inside of the specimen. The crack propagation was shown as a representation of displacement contours ($2\mu m$/line). They demonstrated that for wider cracks, the contour maps of DIC results are unable to portray crack shape as effectively, though crack width information is clear and accurate. Also, the shape represented in the contour map is dependent on the layout of the node grid when the discontinuities become large.

The periodic bias in measured displacements can be removed by using higher interpolation functions [117]. A more precise estimation of the actual position of a point on the deformed specimen can also

be determined by fitting a bilinear surface to the correlation coefficient scores for the discrete pixel locations surrounding the highest correlation and choosing the location of the surface's peak [71]. Lawler and co-workers [71] found that DIC is very effective at determining the crack width and location of small cracks (under $30\mu m$).

In the experimental campaign presented in this chapter, the size of each subimage is equal to 21 x 21 pixels. They are regularly spaced in the reference image (of size 1392 x 1040 pixels) in the form of a grid. The commercial package Vic2D by Correlated Solutions is used to perform digital image correlation analysis and the NCC correlation criterion is adopted. Gaussian weight functions that provide the best combination for spatial and displacement resolutions are used [121].

2.2 RILEM methods to determine material fracture parameters

Conventional test methods based on LEFM are not able to determine material properties of concrete due to the presence of a large fracture process zone. Different nonlinear constitutive laws able to describe strain localization and failure of quasi-brittle materials can be found in the literature. They use material parameters which are independent of the structural geometry and size. In order to determine these material parameters, the RILEM committees on fracture mechanics of concrete (Committees *50–FMC* and *TC89–FMT*) have proposed three tests detailed hereafter.

2.2.1 Work of fracture method

Work of fracture is the first method for determining fracture properties of concrete to be proposed as a standard [105]. The basis for applying this method to concrete was developed by Hillerborg and co-workers [50] who adopted the fictitious crack concept [51]. In LEFM, the critical energy release rate G_{IC} is the energy required per unit crack extension in a material with no fracture process zone, i.e. all the energy is surface energy, and no energy is dissipated away from the crack tip. On the contrary, in the work of fracture method, the process zone exists and therefore the total energy includes the energy dissipated per unit crack propagation distance of the fracture process zone as a whole, and it is called fracture energy G_f. The proposed test standard uses a beam specimen loaded in three point bending with a central notch. Complete details of the proposed standard are given in the RILEM Recommendation [105]. The fracture energy is calculated as

$$G_f = \frac{W_0 + mg\delta_0}{A_{lig}} \tag{2.10}$$

Where W_0 is area under the vertical load displacement curve up to δ_0; δ_0 is displacement corresponding to complete failure (when load equals zero); mg is $(m_1+2m_2)g$ where m_1g is beam weight between supports, and m_2g is extra weight carried by the beam (e.g. fixtures); and A_{lig} is original, un-cracked ligament area.

The reported results show variability ranged from about 2.5% to 25%. The results also show an undesirable dependency on the size of the beam and the notch length [14].

2.2.2 Jenq and Shah two parameters model

The effect of a large sized FPZ at the crack tip of the notch or continuous crack, is a reduction of the stresses at the crack tip and a pushing back of the peak stress. Consequently, the specimen behaves roughly as an elastic specimen with a longer effective crack length. Such an approach is known as the effective crack approach and is adopted in the model of Jenq and Shah [61].

The two fracture parameters of the model are (1) the critical stress intensity factor K_{IC} at the tip of the effective crack of length a_c at P_u (defined hereafter) and (2) the value of the critical (at P_u) crack tip opening displacement (δ_{CTOD}), which is calculated at the tip of the pre-existing crack or notch, whose length is denoted as a_0. RILEM recommends [106] to perform a three point bending test on a concrete beam under stable displacement control with the crack mouth opening displacement as the displacement control variable. The critical point P_u is estimated at about 95% of the peak load in the post-peak branch. At that point, the specimen should be unloaded manually and reloaded again as soon as the load has reached zero. The effective crack length is calculated from the compliance decrease (see [106]). In the RILEM Recommendations, the various formulas are given to compute the critical stress intensity factor K_{IC} and the critical tip opening displacement δ_{CTOD}. This method, although more complicated, provides similar results with the size effect model detailed hereafter [118].

2.2.3 Size effect method

One of the RILEM Recommendations [107] on concrete fracture recommends determining the material fracture characteristics from the Bazant's size effect law [107]. The idea of this method proposed by Bazant and Pfeiffer [12] is that one first determines the parameters of the size effect law by linear regression and then the parameters of material fracture. Three point bending beams are recommended. The span to height ratio of the specimen, S/D should be at least 2.5 and the ratio of notch length to the beam height, a_0/D, should be between 0.15 and 0.5. The notch width should be as small as possible and must not exceed 0.5 d_a, where d_a is maximum aggregate size. The width b and

height D of the beam should not be less than $3d_a$. At least three sizes of specimens of different heights ($D = D_1 \ldots D_n$) should be tested. The smallest height D_1 must not exceed $5d_a$ and the largest D_n must not be smaller than $10d_a$. Because of the random scatter exhibited by concrete, the ratio D_n/D_1 must be at least 4. To avoid differences in the hydration heat effects and to minimize other types of size effect, all the specimens should be geometrically similar in the other two dimensions, that is, the third dimension (width b) should be the same for all the specimens. The specimen should be loaded under constant displacement rates.

2.3 Experimental research

2.3.1 Materials

The cement used to prepare the concrete is ASTM type I with 28 days strength of 52.5 MPa. Two types of coarse aggregates are selected from the same source. These aggregates are crushed limestone particles with maximum size of 12 and 20*mm* respectively. Fine aggregates used are crushed fine sand with maximum size not greater than 5*mm*. Particle size distribution curves are presented in Figure 2.3. The choice of coarse aggregates can be clearly understood from the graph i.e. the two coarse aggregates present parallel size distribution between their maximum and minimum sizes respectively. Two types of concrete mixes are prepared with mix design proportions as shown in Table 2.1. In mix M1, the maximum aggregate size is 20*mm* and in mix M2 the maximum aggregate size is 12*mm*. Workability tests are performed and both mixes are found nearly equally workable in terms of slump value (= 4.0*cm*). However, cement paste content is found to be a little higher in concrete mix M2 than in mix M1. This is because in mix M2, due to the smaller aggregate size, a lesser amount of paste is needed to coat the aggregate particles and the remaining paste stays in suspended form. A small quantity of super plasticizer is used to improve the workability of both mixes from 5.0 to 6.0*cm* in terms of slump value.

Table 2.1 Concrete mix design details.

	M1 kg/m^3	M2 kg/m^3
Cement (Portland 52.5N)	312	312
Sand	820	820
Coarse aggregate (12.5 – 20*mm*)	784	-
Coarse aggregate (5 – 12.5*mm*)	316	1100
Water	190	190

Table 2.2 Mechanical properties of concrete.	M1	M2
Average strength at 28 days	MPa	MPa
Compressive strength (f_c')	45	48
Split cylinder strength	3.5	3.8
Young's Modulus	38 x 10^3	45 x 10^3
Poison's ratio	0.25	0.25

Tests for axial compressive strength and split cylinder tensile strength, using cylindrical specimens with diameter 100*mm* and height 200*mm*, are performed on both mixes. Stiffness modulus is determined by a non destructive test using Grindosonic apparatus. Results are summarized in Table 2.2.

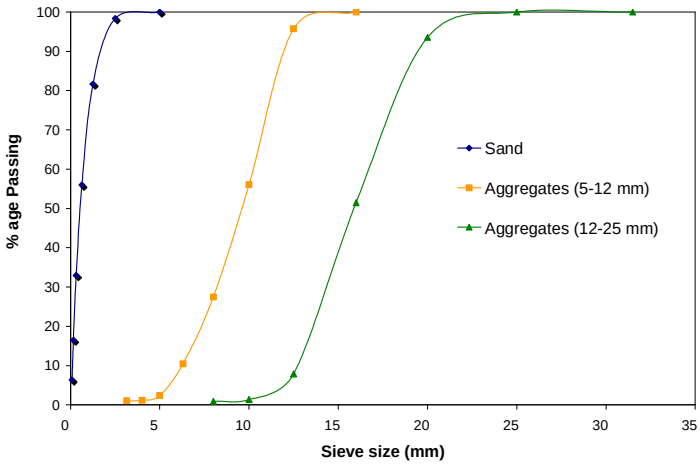

Figure 2.3 Particle size distribution curves of concrete constituents.

2.3.2 Specimen preparation

Three sizes of specimens are prepared, which are geometrically similar in two dimensions. The cross section of the specimens is rectangular, and the span to depth ratio is *l/d* = 3:1 for all the specimens. The cross sectional height *d* is 100, 200 and 400*mm* respectively for the three specimens. The thickness or third dimension *b* is kept constant at 100*mm* for all the specimens. The formwork used for casting beams is made of wooden sheets of 2*cm* thickness (Figure 2.4). Smaller beams are cast using a formwork to cast a set of 4 beams. For medium size beams, a formwork to cast a set of two beams is used. The large beams are cast using a formwork for a single beam. The beams are notched at midspan. The notch length varies in proportion to the size of the beam with a constant *a/d* = 0.2 for all

the beams. The notch is created using a rigid, non-stick Teflon strip 3*mm* thick, which is placed into the mould before pouring the concrete. The concrete is poured in three layers, by increasing the layer thickness and the vibration time as the time increases. The concrete vibration is done using a vibration table. The formwork is removed with care after an initial curing period of 24 hrs at 20°C and relative humidity of 95%. The beams are covered with a plastic sheet during this initial curing period to avoid surface evaporation and autogenous shrinkage cracks. The beams are then kept completely submerged for 28 days in a water chamber controlled at 20°C.

(a) (b)

Figure 2.4 (a) Concrete specimens upside down (b) Formwork of concrete beams

In the following, the beams are classified into three classes depending upon their dimensions. The beams are designated as D1, D2 and D3 for small, medium and large sizes respectively (Figure 2.5). For M1 concrete, all the three classes of specimens are cast to study the size effect. The fracture parameters are obtained following RILEM Size Effect Method [107]. For M2 concrete, only D1 and D2 specimens are cast to study the effect of aggregate size on crack propagation of concrete.

Figure 2.5 Three beams of geometrically similar size in two dimensions (width is constant)

Some difficulties are encountered during the fabrication and testing of the beams. The current study seems very sensitive to aggregate particles arrangement. Therefore to obtain the same quality of concrete for all specimens, maximum attention is paid during the fabrication of concrete, its pouring

and vibration. However, the casting of large beams requires special attention. Since the beam is deeper, there is a chance that the formwork will swell. Therefore, inverted U shape supports are placed on top of the formwork in the midspan region. This provides support to the beam formwork and helps it to keep its shape and thus the beam thickness. For large sized beams, the formwork and Teflon strip are removed with special care.

The surface of the specimen should be considered as well. In fracture experiments where highly accurate surface deformation measurements are required, the specimen size and the condition of the surface of the specimen must be highly specific. The latter is extremely important when we are using optical crack detection equipment. The most accurate surface smoothness can be obtained when steel moulds are used but they are difficult to handle. In this case, timber moulds were used. In the very first batch, the specimen surface obtained was less smooth. Then, by careful vibrating and placement of concrete in layers, this problem was overcome. However, in the cast specimens, problems always remain, e.g. bleeding water normally causes a rather rough surface. Moreover, the skin of the specimen is rich in fine particles. High surface smoothness can also be obtained by sawing the specimen from large concrete [124].

Notched specimens are generally used in fracture experiments to confine crack growth to a known location, and the placement is controlled by LVDT (or CMOD gauge). Concrete is rather notch insensitive, in particular when large coarse aggregates are used in the mixture [124]. In fact notches restrict the possibilities where a crack nucleate, thus, by chance a notch may be situated in a stronger or weaker part of the specimen, which may cause the observed strength to be either higher or lower. To avoid this problem newly developed electronic devices can be used on an un-notched specimen. In such a scheme, many LVDTs are placed in a row along the specimen length. Dedicated electronics and software decide which LVDT is to be used for test control and which fracture zone will nucleate from the weakest spot.

2.3.3 Loading frame and mechanical measurement devices

The loading frame consists of *Instron* closed-loop universal testing machine of 160 kN capacity. The load was applied with the help of a circular jack to ensure a point load. A rubber pad was placed between the load jack and beam to take care of the surface unevenness and to avoid damage under the load. The beam was simply supported on two circular supports. The notch mouth opening displacement was measured with a crack mouth opening displacement (CMOD) gauge of capacity ± 4*mm*. The two blades of the CMOD gauge, each 10*mm* in length, were attached to two metallic plates 10*mm* apart, one on either side of the notch at the bottom face of the beam as shown in the Figure 2.6.

These metal plates were firmly attached to the specimen with high strength glue, which guaranteed the perfect stability of the plates and consequently the CMOD gauge.

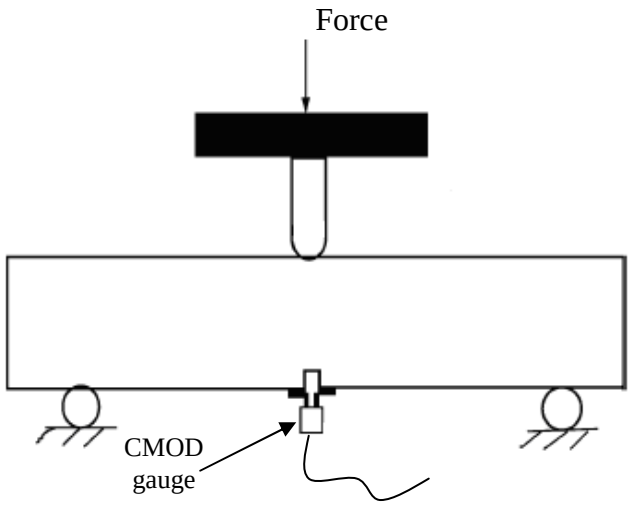

Figure 2.6 Experimental setup of three point bending test

2.3.4 Test control

All the tests were performed with a controlled notch opening displacement rate of 0.05$\mu m/sec$. Therefore, load was applied as a function of the notch mouth opening. This loading arrangement allows us to obtain firstly, a gradual increase in the crack opening and secondly, a steady decrease of load bearing capacity of the beam in the post-peak regime. The mechanical data thus obtained is the evolution of a force with a precision of 1/100 Newton and the notch mouth opening displacement with a precision of 1/10 of micrometer, acquired after each 1 *sec* interval. The load is applied in two stages: a preload and then the main load with controlled notch mouth opening displacement. The preload is the load corresponding to 1 μm of CMOD or 0.25 N (whichever is attained earlier) and is operated manually.

The stability of the loading frame is also very important. The loading should be applied vertically to study two dimensional crack propagation. Therefore, the stability and verticality of the loading frame and the loading jack are assured before every test. An eccentricity in the loading can produce crack propagation which will have no characteristic meaning.

The measuring length of the CMOD gauge is the distance between the two metallic plates. Since the cracking process is highly localized, the deformation measured with the CMOD gauge is equal to the crack width, plus the elastic strain of the part of the specimen contained in the measuring length. Since the specimen unloads during crack growth, at larger crack openings, i.e., in the tail of the softening diagram, the contribution in the measuring length becomes negligibly small. Therefore, the direct

CMOD measurement is not generally corrected for the elastic deformations in the measuring length. Moreover, the CMOD measures the displacement between two points which are glued to the concrete surface. Rotations of these measuring points might introduce an error in the displacement measurement as shown in Figure 2.7. In tensile tests the rotations are generally negligibly small, however, in bending and compressive tests the effects might become important. Rotations of measuring points do not blur the test results if the strain gauges are glued directly on the specimen surface.

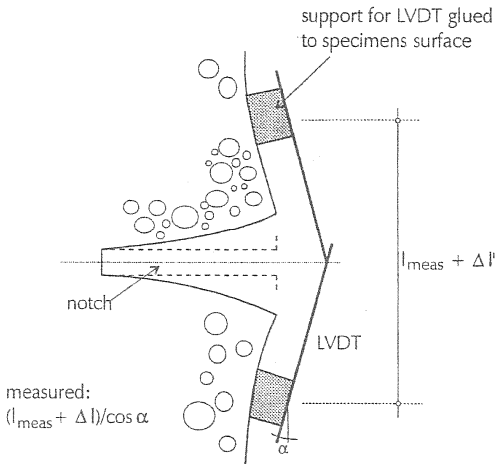

Figure 2.7 Local rotations as a source of error in notch opening measurement using CMOD gauge.

2.3.5 Digital Image Correlation - experimental setup

In our experimental program, the digital images are acquired continuously as the specimens are loaded. Two digital cameras with 75*mm* macro lens are used to capture images of both faces of the beam (Figure 2.8). The digital cameras have a resolution of 1040 x 1392 pixels and give 256 levels of gray output. For each size of the beam, two series of tests are performed. In the first series, the cameras are mounted in order to image an area of approx. 60 x 100*mm* above the notch of the beam. At this location, notch opening and initial crack profile are captured. For this resolution, one pixel in the image represents an approx. 35μm square on the specimen, which is considered sufficient to determine a displacement measurement with 2μm accuracy [30]. In the second series, the cameras are mounted at a distance required to observe the full height of the specimen (except for D3). Thus the resolutions obtained for each size of specimen are 1 pixel = 105μm for D1, 1 pixel = 180μm for D2 and 1 pixel = 288μm for D3 specimens. Four lamps, two on either side are used to improve the luminosity of the images. The images from the camera are stored using an image grabber program developed using LabVIEW. The image grabber is synchronized with the testing machine and it allows us to take images with two cameras at the same time at a given frame rate. The images are taken at a rate of 6 images per minute for each camera. The images are stored in the system and are analyzed afterwards. The resolution of the system depends directly on the distribution of gray levels which

depends on the texture of the material. The texture of the surface can be improved by using a fine network of scratches, classical painted speckle pattern or nitropental paint. In this study, a speckle pattern of black and white paint is sprayed onto the surface of the specimen, which improves the displacement resolution to about five times [115].

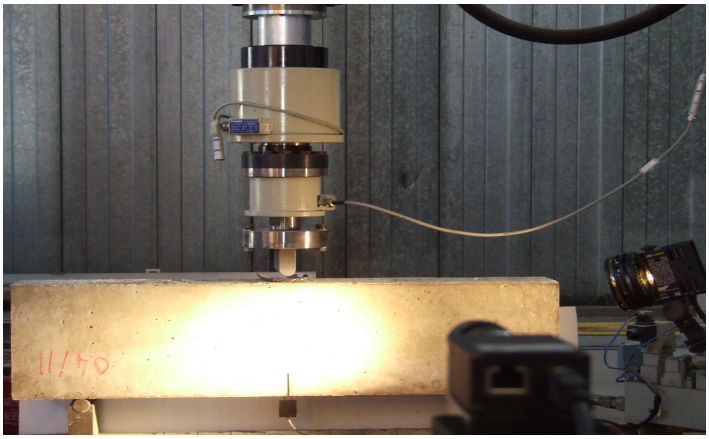

Figure 2.8 Experimental setup of digital image correlation method

In the above experimental study, local estimates of the displacements are used by considering independent interrogation windows. An alternative solution is to use global (or Galerkin) approaches to measure displacement fields. It is based on a variational formulation of the conservation of the brightness [128]. When particularized to finite element shape functions, it allows one to use all the numerical tools to analyze cracks (e.g., X-FEM [93]). This procedure was followed to develop eXtended Digital Image Correlation (X-DIC) [110] to analyze straight or curved cracks.

Up to now, only 2D displacement fields are discussed. Stereovision [116] can also be used to evaluate 3D displacements on external surfaces of a body using camera pairs. This technique is referred to as 3D-DIC or Volumetric-DIC, and will be reserved in the sequel to determine 3D displacements in a volume.

To monitor phenomena within opaque materials, X-Ray Computed Micro Tomography (XCMT) is a very powerful way of imaging material microstructures in a non-destructive manner [5]. In particular, cracks can be observed and crack opening displacement can be measured in the interior of the specimen [49]. When the crack morphology is determined, X-FEM techniques allow for the evaluation of surface vs. bulk propagation features [42]. Enriched kinematics are also implemented (i.e., it corresponds to eXtended Digital Image Correlation to measure 3D displacements, or X3D-DIC) [111]. This procedure allows one to bridge the gap between 3D pictures and numerical models.

Conclusion

In this chapter, the outline of the experimental program is presented. In order to study the size effect, RILEM size effect method was adopted. Two types of concrete mixes were used. The M1 concrete mix (maximum aggregate size = 20*mm*) was used in the RIELM size effect experiments. Three point bending tests were also performed on the M2 (maximum aggregate size = 12*mm*) concrete specimens under similar loading and boundary conditions in order to study the effect of aggregate size on the fracture behaviour. The experimental procedure was simple to carry out. The loadings were applied as a function of constant notch mouth opening rate. This caused a progressive fracture in the beams and was easy to monitor.

Digital image correlation (DIC) technique is used in this study to measure the cracking in concrete. The basic principle and the application of DIC in this experimental program are presented in this chapter. DIC allows us to measure surface displacements of the concrete specimen. It is found to be a robust and highly precise tool for fracture measurements. The possible error sources (lens distortion, vibrations, periodic bias and image distortions etc.) are eliminated by adopting a higher interpolation function and a higher order correlation algorithm. The results will be presented in the next chapter.

Chapter 3

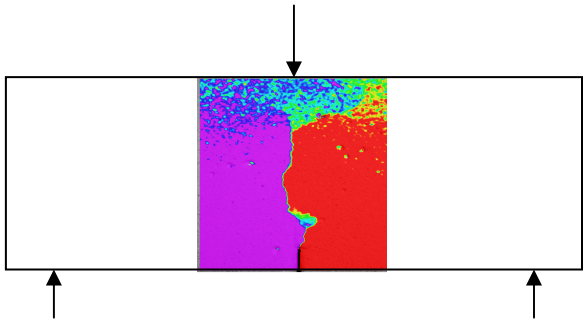

Experimental Investigation of Crack Opening in Concrete Fracture

In order to build sustainable structures and especially for sensitive installations, the study of structural behaviour must integrate with local phenomena, e.g. fracture and strain localization. The fracture usually develops in the form of main crack, with branches, secondary cracks and a microcracking zone ahead, as shown in Figure 3.1. The fracture process, however, depends largely on the aggregates size and distribution, the void structure and the aggregate matrix interface.

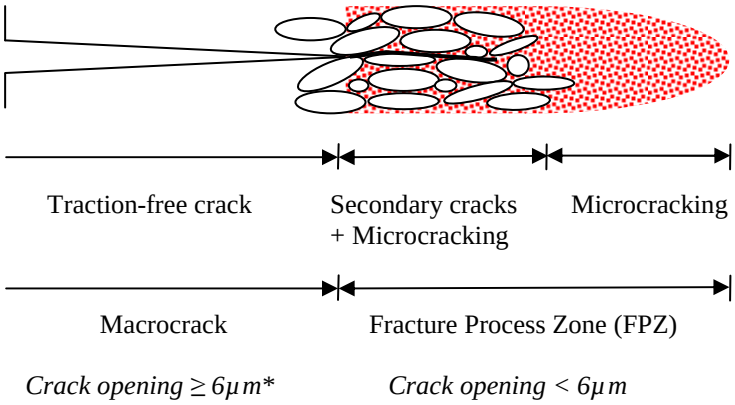

Figure 3.1 A schematic diagram to illustrate cracking in concrete. *[91]

Crack opening is a key parameter when estimating the durability of the structural components of most concrete structures. Also, in Eurocode [40], the crack opening is specified as a principal element in the crack control provisions. Many numerical models can also be found in literature in which crack opening is considered as a key fracture parameter. However, very few experimental studies exist, in which the fracture behaviour and the size effect are investigated based on the crack opening measurements.

In this chapter, experimental results of three point bending tests on concrete beams are analysed to characterize the fracture process.

- In the first section, the mechanical response of the beams is analyzed.
- The approach to determine the crack opening displacements and profiles from the displacement field obtained by DIC is presented in the second section.
- In the third section, the fracture process is characterized based on the crack opening in the crack beams.
- The fourth section deals with the effect of aggregate size on the cracking process.
- In sections five and six, the size effect on mechanical response and crack opening are investigated respectively.
- In the last section a case study is presented in which reinforced concrete beams are tested in three point bending. The crack openings and spacing are monitored and compared with design values of Eurocode.

3.1 Mechanical response of the concrete beams in terms of global variables

The results presented in this chapter refer to three point bending tests, the experimental setup of which is presented in Chapter 2. The mechanical data obtained is in the form of two variables: the force applied by the hydraulic jack and the notch mouth opening displacement, measured using an external Crack Mouth Opening Displacement (CMOD) gauge. As recommended by RILEM, loading is applied by controlling the notch mouth opening with a constant rate of $0.05\mu m/sec$.

For each class of concrete beams (small D1, medium D2 and large D3) three or more specimens are tested to study the variability of the experimental results. The mechanical responses presented in this chapter are the average loading curves and the gray zone indicates the variability of the results. The average curves are obtained by averaging the applied force for different beams of the same class, corresponding to the same crack mouth opening displacement.

Two types of concrete mixes (M1 and M2) are used in this study, in which size of aggregates is varied. In the following, firstly M1 (d_{max} = 20mm) concrete beams are analyzed in order to study the fracture process based on the crack opening measurements. Size effect analysis is also performed on M1 concrete beams. Lastly, the results of the bending tests performed on the M2 (d_{max} = 12mm) concrete beams are presented in order to study the influence of aggregate size on crack opening in concrete.

3.1.1 M1 concrete beams

M1 – D1 beam

In the M1 – D1 beam, the ratio of maximum aggregate size (20mm) to the height of the beam (100mm) is 1:5. Figure 3.2 presents the Force-Notch mouth opening displacement curve.

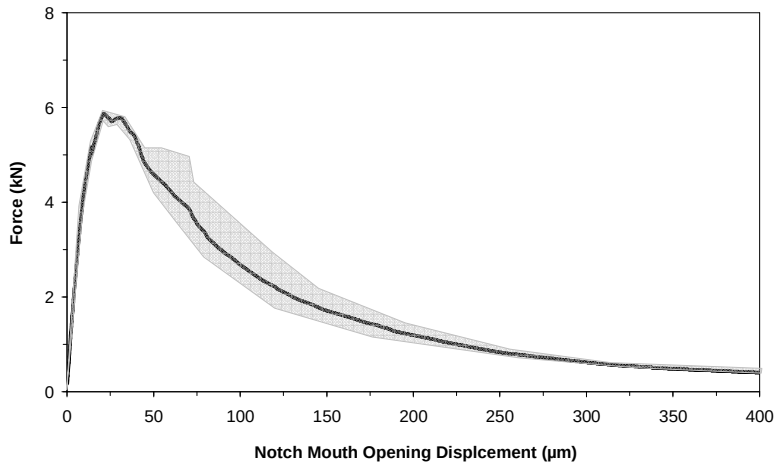

Figure 3.2 Average Force-Notch mouth opening displacement curve for the M1 – D1 beam.

M1 – D2 beam

This is the intermediate size beam in which the ratio of maximum size of aggregates to the height of the beam (200*mm*) is 1:10. Figure 3.3 presents the Force-Notch mouth opening displacement curve for the M1 – D2 beam.

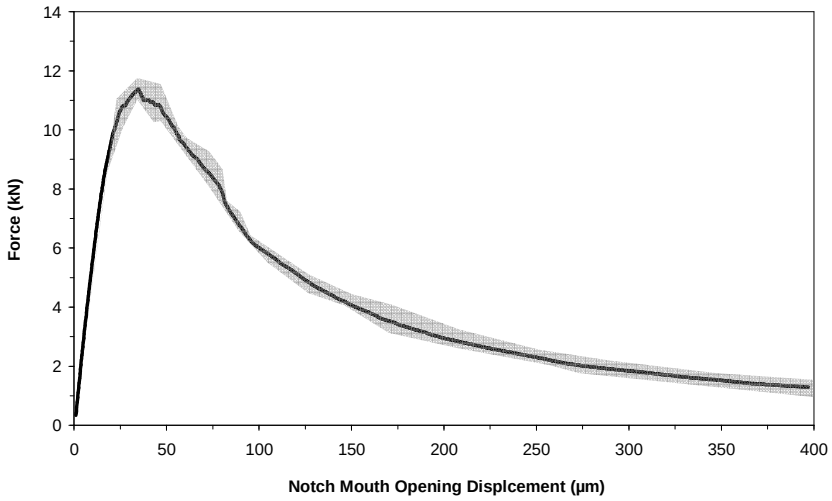

Figure 3.3 Average Force-Notch mouth opening displacement curve for the M1 – D2 beam.

M1 – D3 beam

This is the largest sized beam in which the ratio of the maximum aggregate size to the height of the beam (400 *mm*) is 1:20. Figure 3.4 presents the Force-Notch mouth opening displacement curve.

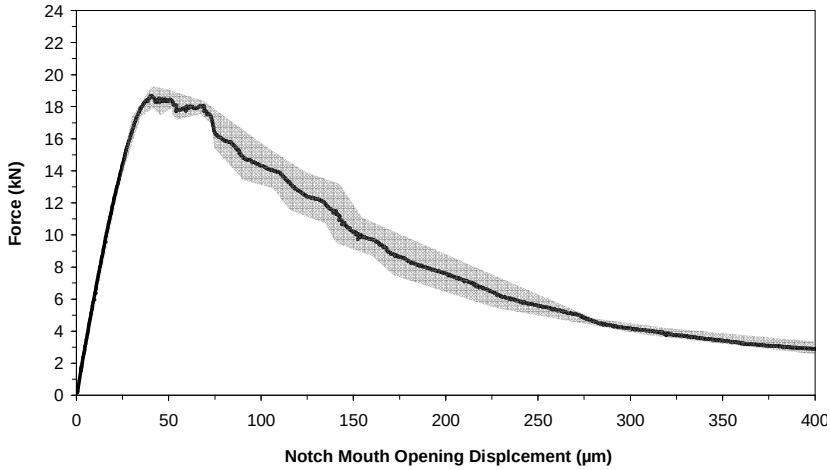

Figure 3.4 Average Force-Notch mouth opening displacement curve for the M1 – D3 beam.

In all the above curves, the relationship between the applied force and the notch mouth opening displacement can be divided into four parts. In the first part, the relationship is linear i.e. the material remains in the elastic range. The second part starts as soon as the curve deviates from linearity. Crack opening starts to increase at a faster rate, indicating the development of damage in the material. In this part, the load continues to increase further until the peak load value is reached and the material cannot go beyond this maximum loading capacity.

After the peak load stage, the notch mouth opening displacement continues to increase and the load starts to decrease. This is the third part of the curve, where a major load drop occurs. A shift in the Force-Notch mouth opening displacement relationship is observed in the tail of the curve. This final part of the curve shows a considerable increase in the crack opening, while the load decreases gradually. The notch mouth opening displacement continues to increase until the specimen fails.

The above stages are the typical trends observed in the three types of beams. These stages are no doubt related to the crack propagation in the material but this information is not available in the mechanical curves.

3.2 Digital Image Correlation : Determination of crack characteristics & validation

This section is a description of the procedure adopted to determine crack opening profiles from displacement fields which have been obtained by Digital Image Correlation (DIC).

3.2.1 Displacement and strain fields

The correlation algorithm determines the location of each sub-pixel in the imaging area. It provides the corresponding displacement vectors in the coordinate axis. The horizontal (axial) displacement can be easily calculated from the displacement vectors. Figure 3.5(a) presents the axial displacement field on the surface of the beam (M1-D2 specimen at peak load). A sudden jump in the displacement values can be observed ahead of the notch and it represents a discontinuity (crack) in the material. Crack path can be determined easily from this figure.

The other displacement field (vertical) determined from the displacement vectors can be useful in obtaining the load point settlement, but this value has to be corrected with the settlement of the supports of the beam. In our experiments, the imaging area is limited to the midspan of the beam and thus, the specimen surface above the supports is not captured. This is the reason why the vertical displacement field is not analysed in this study.

The displacement field can also be used to calculate strains (outside of the crack area) using standard continuum mechanics. Figure 3.5(b) presents the field of the first component of the Green Lagrange strain tensor (ε_{xx}). It is calculated between two instantaneous loading conditions i.e. 60% pre-peak and at the peak load. It can be observed that strains localize into a narrow band and the material undergoes cracking in this area.

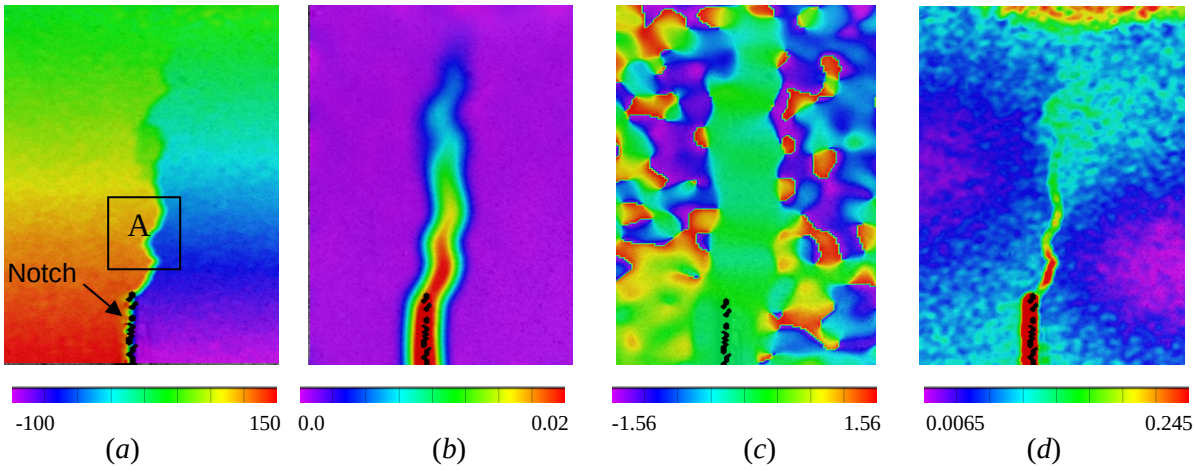

Figure 3.5 (a) Axial displacement (μm) (b) Green Lagrange axial strain (ε_{xx}) (c) Principal strain direction (*radians*) (d) Correlation error (*pixel*).

The profile map of the principal strain direction is presented in Figure 3.5(c). Comparing the Figures 3.5(a) and 3.5(c), it can be seen that in the areas near the crack, the principal strains are almost parallel to the horizontal axis (± 0.2 radians). This observation will be used in the following section when determining the crack openings.

The correlation error, calculated from the degree of similarity of the gray levels and the rotation of the sub-image is presented in Figure 3.5(*d*). The correlation error is relatively important near the crack. This is because the sub-images close to the crack not only translate but also rotate and deform, and this distortion of the sub-images affects the correlation algorithm.

Figures 3.6(*a*) and 3.6(*b*) show the surface profile of the axial (horizontal) displacement and axial strain field (ε_{xx}) on the surface *A* of the specimen (see Figure 3.5(a), the y-axis corresponds to the height of the specimen). The jump in the displacement field and the localization of strains show the evidence of a strong discontinuity or crack in the material.

When a crack appears in the material, strains in the area near the crack cannot be calculated from the displacement field, as the standard continuum mechanics assumptions are no longer valid. Therefore, the strain fields are not further analysed in this study.

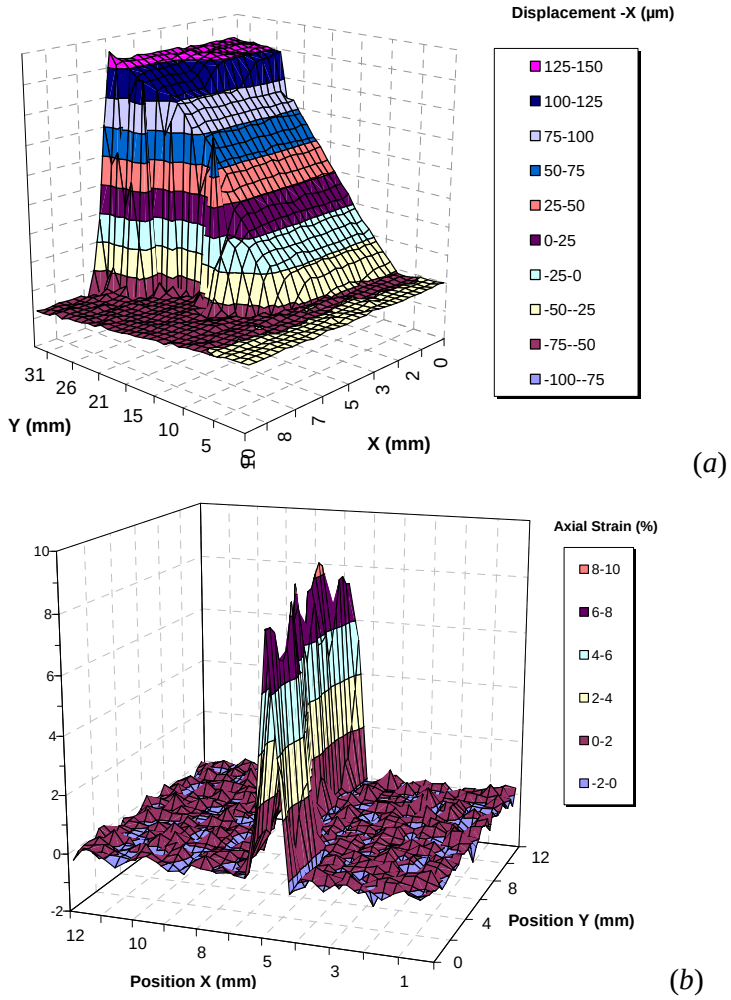

Figure 3.6 (a) Axial displacement field in the area A* (*b*) Axial strain (ε_{xx}) in the area A*.

* For area A see Figure 3.5(a).

3.2.2 Determination of crack opening displacement

In concrete structures, a crack usually passes through the interface between aggregates and the cement matrix. Thus, the crack path is generally tortuous depending upon the size of the aggregates. In this experimental campaign, the cracked surface of concrete specimens is examined through the digital image correlation method. The analysis of the axial displacement field diagram on the surface of the specimen shows that a sudden jump in the axial displacement field occurs as soon as a crack appears in the material. This displacement jump increases with the loading as shown in Figure 3.7. Theoretically speaking, the crack opening is the displacement jump between the two points located just at the faces of the crack. This may be true when a macrocrack is formed and it is wide open. At the tip of the macrocrack, the cracking is diffused due to toughening mechanisms. Also, it is found that the correlation error is maximum near the edges of the crack. The displacement profile in Figure

3.7 shows that the displacement jump occurs in a very small length (about 2*mm*) and then the displacement values remains practically constant. Therefore, a practical approach to measure crack openings is to use the points at a certain distance from the crack, where the correlation error is minimum and the diffused cracking can be contained. In this study, crack opening is measured at a distance of 5*mm* on either side of the crack. This method provides a simplified approach to measure crack opening with a desirable level of precision.

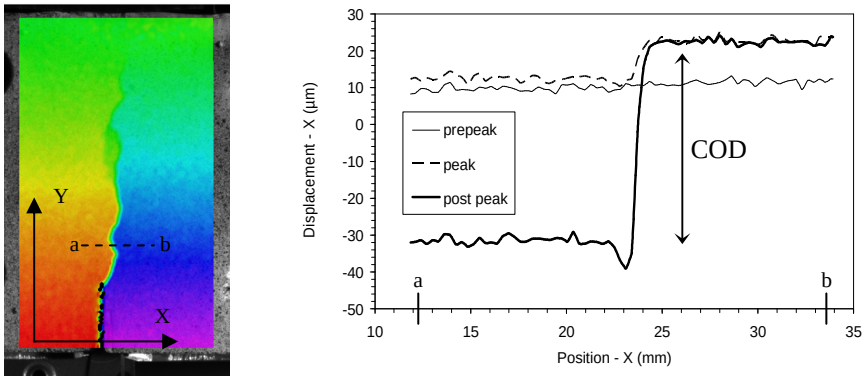

Figure 3.7 Measurement of crack opening displacement (COD) at three different loading stages.

Using the above method, the notch mouth opening displacement (CMOD) is also determined and compared with the result coming from the CMOD gauge (Figure 3.8). The two measurements show good agreement with a maximum variation in the range of ± 3 µm. DIC can only produce surface crack measurements, therefore some discrepancies between the crack opening measurements may occur due to the anisotropy of the material. By taking the average of the displacement fields on both faces of the specimen, this difference can be minimized. Nevertheless, this average will blur the results of the local phenomena occurring at each face of the specimen.

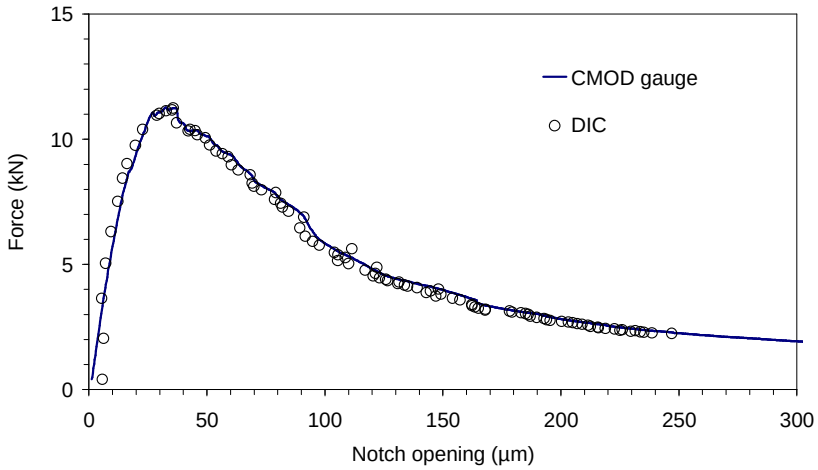

Figure 3.8 Comparison of the notch mouth opening displacement measured by the CMOD gauge and DIC.

3.2.3 Description of the crack opening profile

The shape of the crack path can be derived from the axial displacement field as shown in Figure 3.5(*a*). The crack path obtained in all the experiments is very tortuous. It is also probable that the crack path inside the specimen is different from the crack path on the specimen surface, due to the internal heterogeneity of the material. This is the reason why the crack path on one face of the specimen is not similar to the crack path of the other side (Figure 3.9). The figure presents the crack paths at peak load on both sides of the M1-D2 specimen.

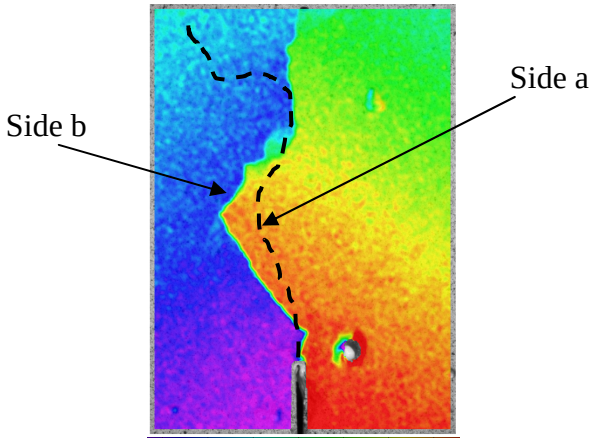

Figure 3.9 Crack paths at peak load on both sides of the M1-D2. The dash line represents the crack path on the other side of the specimen.

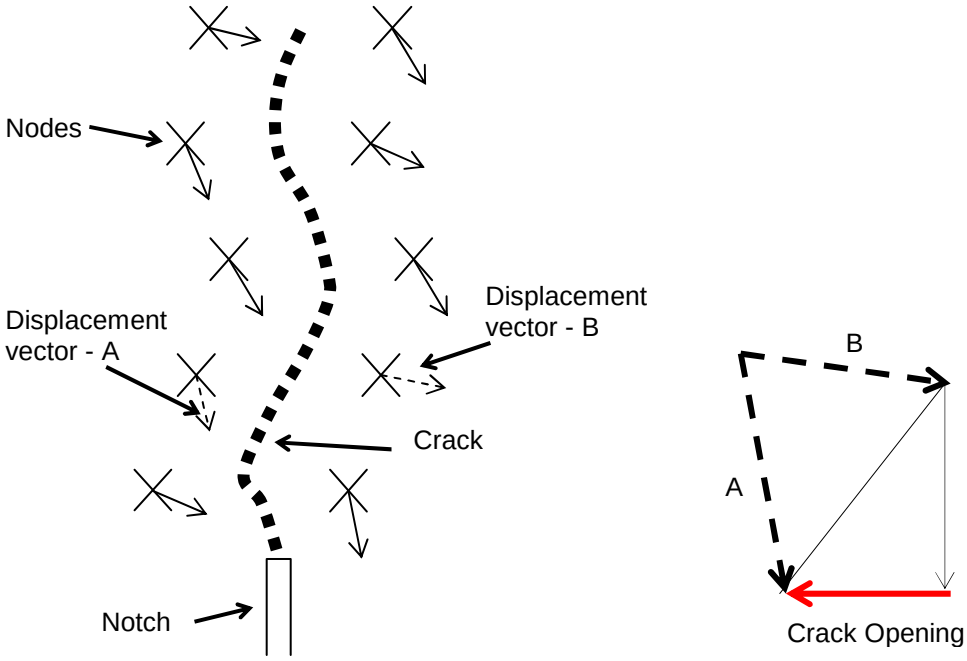

Figure 3.10 Determination of the crack profile from a displacement field.

In this study, we are not interested in the crack path, but in the actual crack openings along the crack. In the following, the variation of the crack opening along the length of the crack is termed crack opening profile. The crack opening profile can be drawn when two parameters are known: the crack opening displacement at different points along the crack path and the vertical coordinates of the crack line.

The crack opening displacement at different crack lengths is calculated from the displacement vectors located at 5*mm* on each side of the crack path, as shown in Figure 3.10. Beams are subjected to three point bending i.e. the lower part of the beam presents tensile stresses and the maximum bending moment occurs at midspan. Because of the notch at midspan, the crack always initiates from here and propagates upwards into the specimen. As the surface of the specimen above the notch is captured by digital cameras, the complete crack opening profile i.e. from the notch mouth (bottom of the specimen) to the crack tip, can be obtained from the axial displacement field data as shown in Figure 3.11.

In Figure 3.11, crack profiles at three different loading conditions (60% pre-peak, peak load and 60% post-peak) of two specimens (beam-1 and beam-2) of the same class (M1-D2) are presented. For beam-1, a higher image resolution is chosen (1 pixel = 35μm) and therefore the image is limited to a small area in front of the notch. This resolution gives a precision of 1.75μm (1/20 pixel [28]) for the DIC measurements. For beam-2, the digital image resolution is lower (1 pixel = 105μm) with a precision of 5.25μm. It can be noticed that the profile of beam-2 is not uniform and follows a zigzag path. If the average line is drawn, the variation of the crack opening displacement will be ± 5μm for beam-2 and ± 2μm for beam-1.

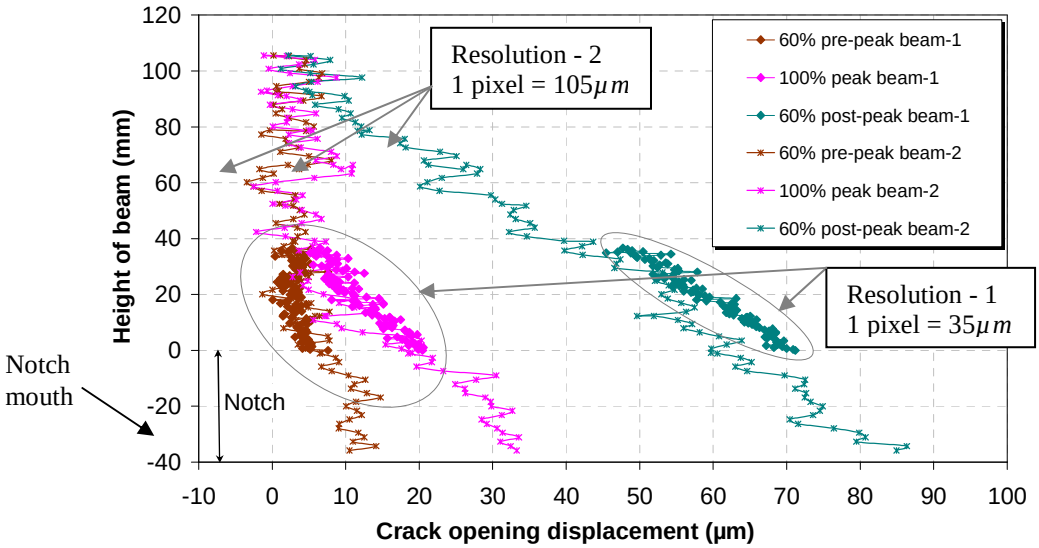

Figure 3.11 Crack opening profiles at different loading stages for two similar specimens (M1-D2) using different resolutions.

In Figure 3.11 it can be also observed that crack opening profiles from different resolutions are the same in the pre-peak loading region and at the peak load. A slight variation appears in the post-peak region. The mean variation calculated between the crack openings of the two profiles is about $3\mu m$. However, this variation can be ignored, considering the size of the aggregates (D_{max} = $20mm$ for M1 concrete) and the measurement precision ($3\mu m$).

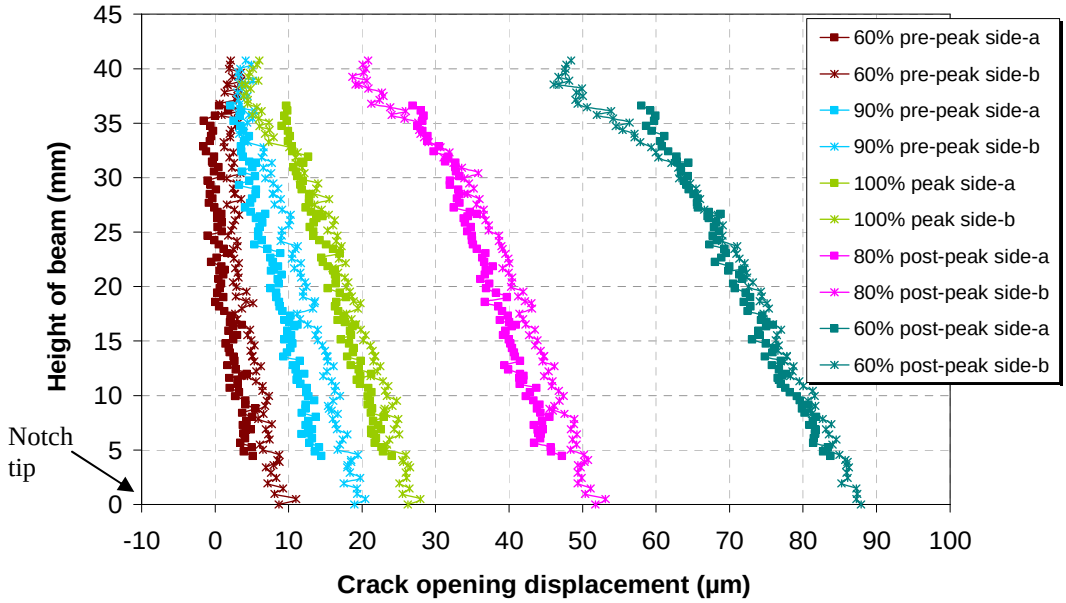

Figure 3.12 Crack opening profile on two sides of the same specimen (M1-D2).

* High resolution

We have already seen in Figure 3.9 that the crack paths on each side of the specimen are not identical. Now Figure 3.12 presents a comparison of the crack opening profiles at different loading stages on both sides of the specimen M1-D2. Comparing Figures 3.9 and 3.12, it can be observed that the crack profiles have the same slope although the crack paths are different. Also, the profiles on both sides are quite similar for all loading stages. However, a small mean variation of $3\mu m$ is observed. In the following, this variation is ignored considering the aggregate size.

3.3 Digital Image Correlation : Results & characterization of the fracture behaviour

In order to analyze the cracking process in the concrete beams, we first analyze the cracking behaviour of the M1-D2 and M2-D2 beams. In the following, the cracking process will be analysed in four loading stages, presented as a percentage of the peak load attained by the specimen.

3.3.1 Crack opening in the elastic phase

In the first stage i.e. up to about 60% of the peak load in the pre-peak region, the Force-Notch mouth opening displacement relationship is almost linear. The crack opening profiles in this loading region are presented in Figure 3.13 and show a zigzag variation of crack opening (in the range of 0-5μm) along the height of the beam. We assume that these profiles do not indicate the presence of a macrocrack before 60% of the peak load. However an increase in the crack opening with the increase in load is observed in the parts of the crack near the notch tip. This indicates that microcracks may be present and can be detected using a different experimental technique, e.g. acoustic emission [94]). As the material shows elastic behaviour in this loading regime, microcracks (if present) have not yet localized.

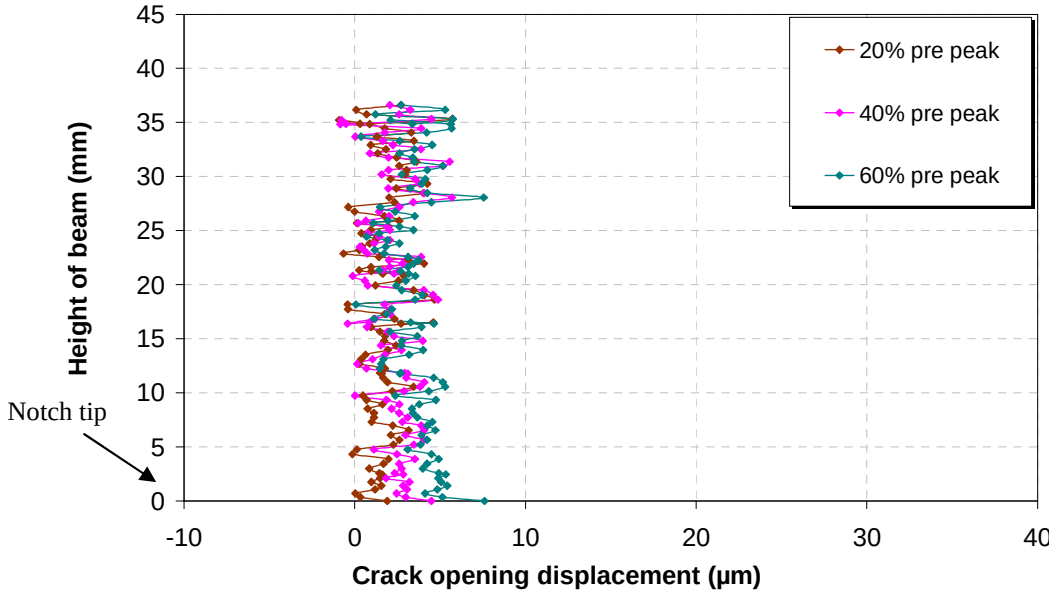

Figure 3.13 Crack opening profiles in the elastic loading stage (M1-D2 beam).

* High resolution

3.3.2 Crack opening profile near the peak load

At the notch tip, the crack opening starts to increase rapidly at about 60% of the peak load (Figure 3.14), evidence of the localization of microcracks into a microcrack. If one adopts the definition of Mindess [91], a macrocrack has not yet existed (crack opening superior to 6μm, see Chapter 1).

In the subsequent loading stages (95% and 100% of the peak load), the crack opening continues to increase near the notch tip of the beam (Figure 3.14). The crack opening profiles show that the macrocrack is advancing upwards in the specimen. The profiles are very zigzag in the final part of the macrocrack and indicate the presence of microcracking and toughening mechanisms at the macrocrack tip. When the loading reaches near the peak load the crack growth becomes more important. A

significant increase of crack opening and advance of macrocrack can be observed between the loading stages 95% of peak load and the peak load. It is assumed that when peak load is attained the crack opening at the notch tip and the crack length (macrocrack length + length of microcracking zone, see Section 3.3.4) reach certain critical values. These values show a typical trend when the size of the specimen is varied and they will be analysed as size effect in Section 3.6.

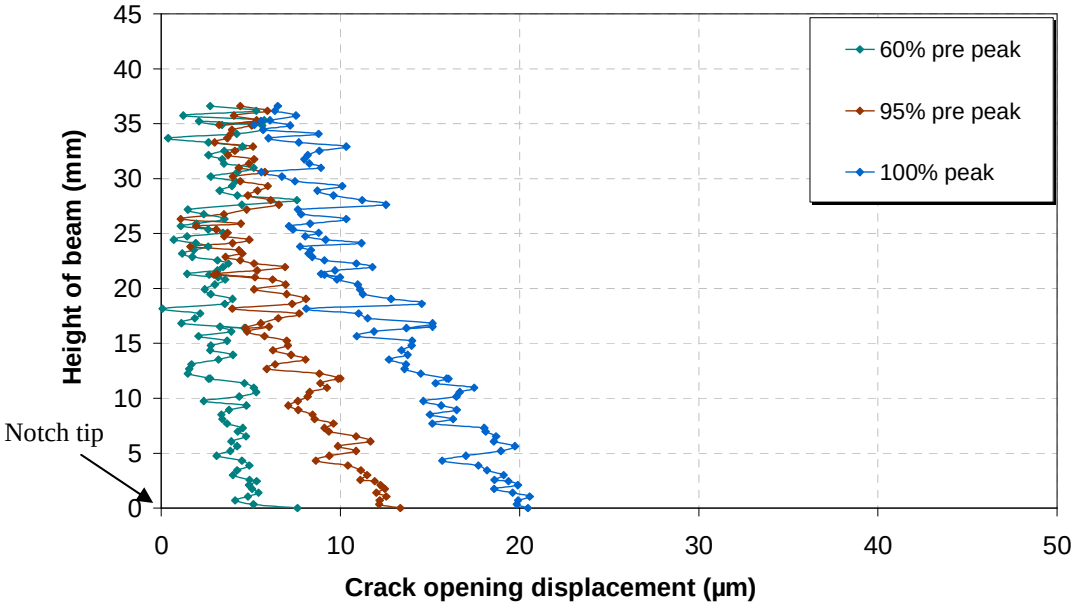

Figure 3.14 Crack opening profiles near peak load (M1-D2 beam).

* High resolution

In all the experiments the digital images are stored at a rate of 15 images per minute. The correlation of these images with respect to the reference image (unloaded specimen) provide with the crack opening at different crack locations and thus crack opening rate can also be calculated at each interval of time. In Figure 3.15 the crack opening rate at three different crack locations is presented.

- At notch mouth, the opening rate is constant as it is controlled by the CMOD gauge.
- At notch tip (after a few unstable measurements at the beginning), the crack opening rate decreases while the load increases. In this part of the curve, the material behaviour is in the elastic range and the decrease of crack opening rate points out the resistance of the material to the opening of the crack. The rate then starts to increase with further increase of the load. This increase of the crack opening rate represents the microcrack localization or macrocrack initiation. This continues until the specimen reaches its maximum load limit. After the peak load, the crack opening continues to increase at constant rate which indicates that the crack surfaces are now completely separated at the notch tip. It is also observed that the crack opening rate at the notch tip is always less than the crack opening rate at the notch mouth.
- At 36.6*mm* from the notch tip, the crack opening rate increases suddenly just after the peak load. After this sudden increase, the crack opening rate increases smoothly and then it becomes

constant. Again it is observed that the crack opening rate is always less than that at the notch tip and the notch mouth.

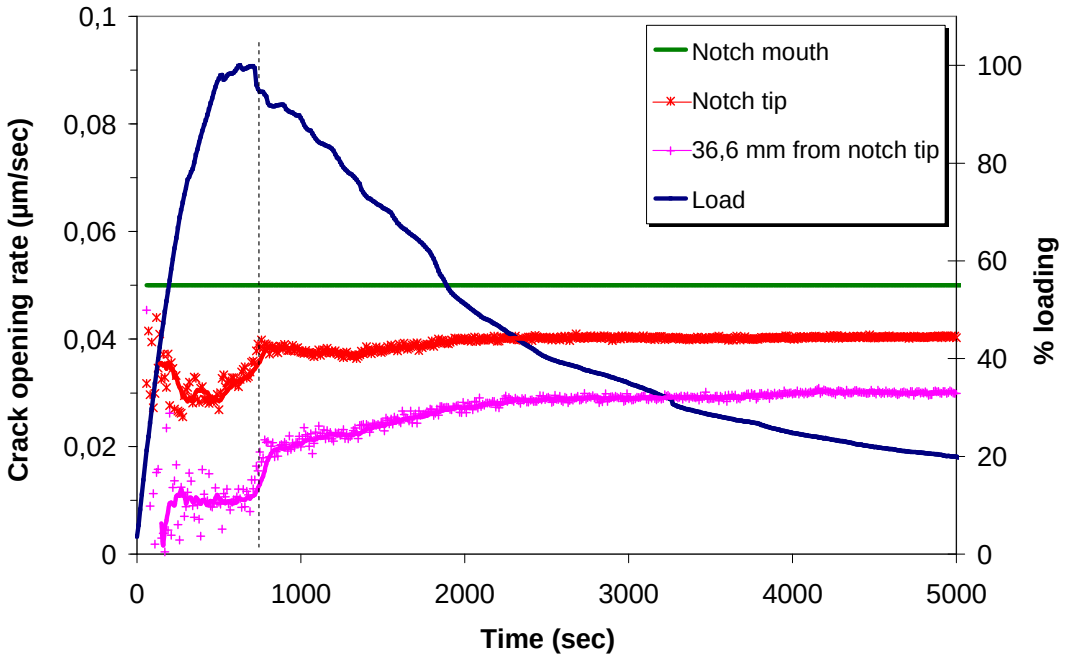

Figure 3.15 Crack opening rate at three locations in the beam (M1-D2 beam).

* High resolution

3.3.3 Crack opening profile in post peak

Figure 3.16 presents the crack opening profiles in the post-peak loading stages. The process of crack growth in the post-peak regime can be divided into two phases. In the first phase, i.e. early post-peak stage, the macrocrack extends into the specimen with a corresponding increase in the crack opening at the notch tip. In the second phase, the crack opening becomes relatively more important as compared to macrocrack extension. In D2-M1 specimens, the second phase starts at about 50% of the peak load in the post-peak regime and at this loading stage, the crack length (see Section 3.3.4) is about 80% of the specimen height. It is assumed that the top 20% part of the specimen height contains strong cohesion forces which may be due to compressive stresses.

In the first phase, a sharp decrease in the specimen load bearing capacity is observed. This is due to the development of macrocrack in the specimen. In the second phase, the specimen strength (or load carrying capacity) decreases mainly due to the breakage of the remaining bonds between the crack surfaces (i.e. the failure of crack surface interlocks due to surface friction and aggregate bridging etc) in the semi-separated crack part. This is observed by a significant increase of the crack opening in the lower part of the beam (Figure 3.16). The macrocrack advances slowly until the specimen fails when

the material strength vanishes completely and there is no possible transfer of stress across the crack (due to surface friction or aggregate bridging). In case of pure tension, the specimen would theoretically not have this behaviour and the crack would propagate rapidly until complete failure of the specimen.

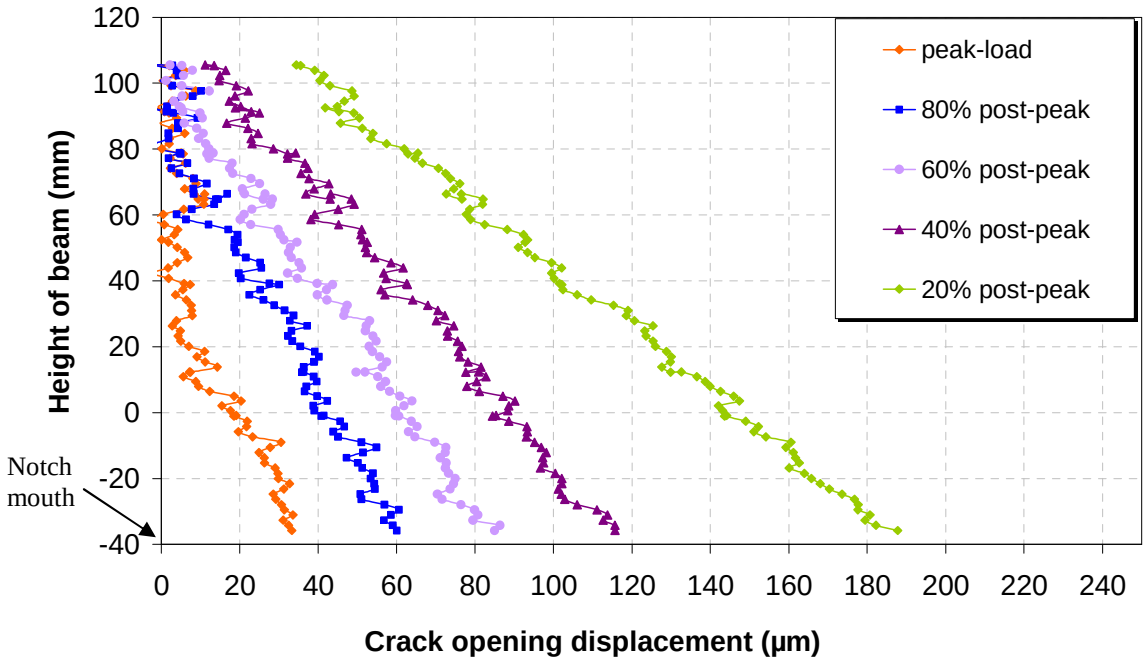

Figure 3.16 Crack opening profiles in the post peak loading stages (M1-D2 beam).

* Low resolution

3.3.4 Measurement of crack length from crack opening data

From the crack opening profile, the crack tip can be theoretically estimated as the location where the crack opening becomes zero i.e. crack closure. In the previous experimental crack opening profiles (Figures 3.14 and 3.16), it is observed that the crack opening decreases upwards along the height of the specimen, sometimes reaching zero (Figure 3.16) and sometimes not (Figure 3.14). In fact, the crack tip is blurred by toughening mechanisms and these mechanisms are more active in the pre-peak regime (Figure 3.14) as compared to post-peak regime (Figure 3.16). Thus, as shown in Figure 3.17, the crack can be divided in two parts:

- In the first part, the crack surfaces are completely separated up to the point where the crack opening decreases and reaches zero (or a constant value). This part of the crack can be considered as the macrocrack.

- In the second part, the values obtained for the crack opening are limited by the precision of the DIC measurement. Also, toughening mechanisms (e.g. aggregate bridging) and microcracking processes occur. The crack surfaces are semi-separated (discontinuous crack length, Figure 3.17) and the size of this zone depends on the size and the packing of aggregates particles. It is thus very difficult to measure using DIC.

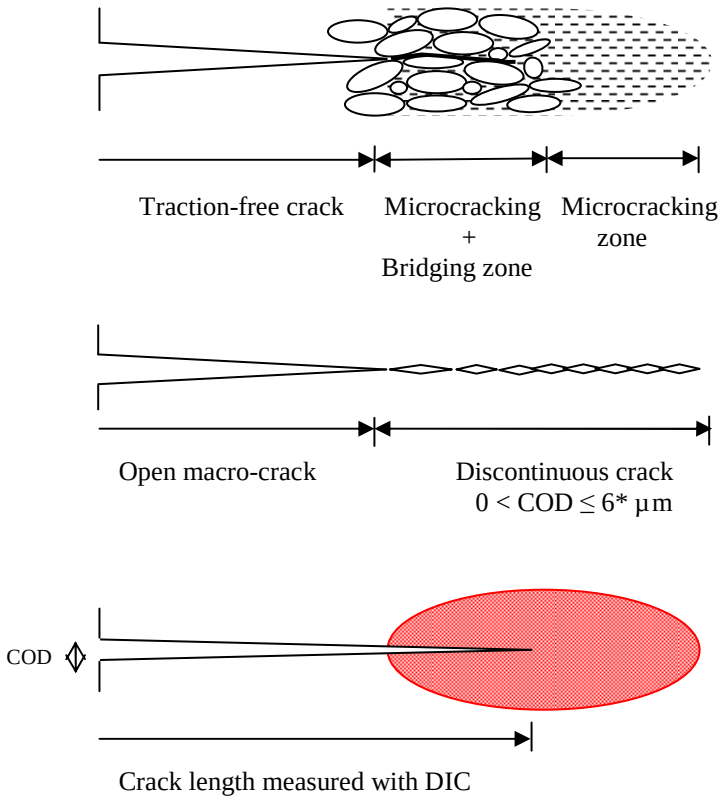

Figure 3.17 Schematic diagram of a crack in concrete structures, representing the open macrocrack and the semi-separated discontinuous cracks. * [91]

Therefore, in the following, the crack length considered is the one represented by the linear interpolations in Figure 3.18.

The crack length measured with DIC or simply crack length is plotted at different loading stages in Figure 3.19. The crack appears at about 60% of the peak load in the pre-peak regime. This loading stage also corresponds to the sudden increase in the crack opening rate at the notch tip (Figure 3.15) and the deviation of the mechanical behaviour from linearity. The crack length increases smoothly until the peak load. A sudden increase in crack length is observed between the peak load and 80% of the peak load in the post-peak regime. The crack propagation becomes relatively slower in the final loading stages until the specimen fails completely.

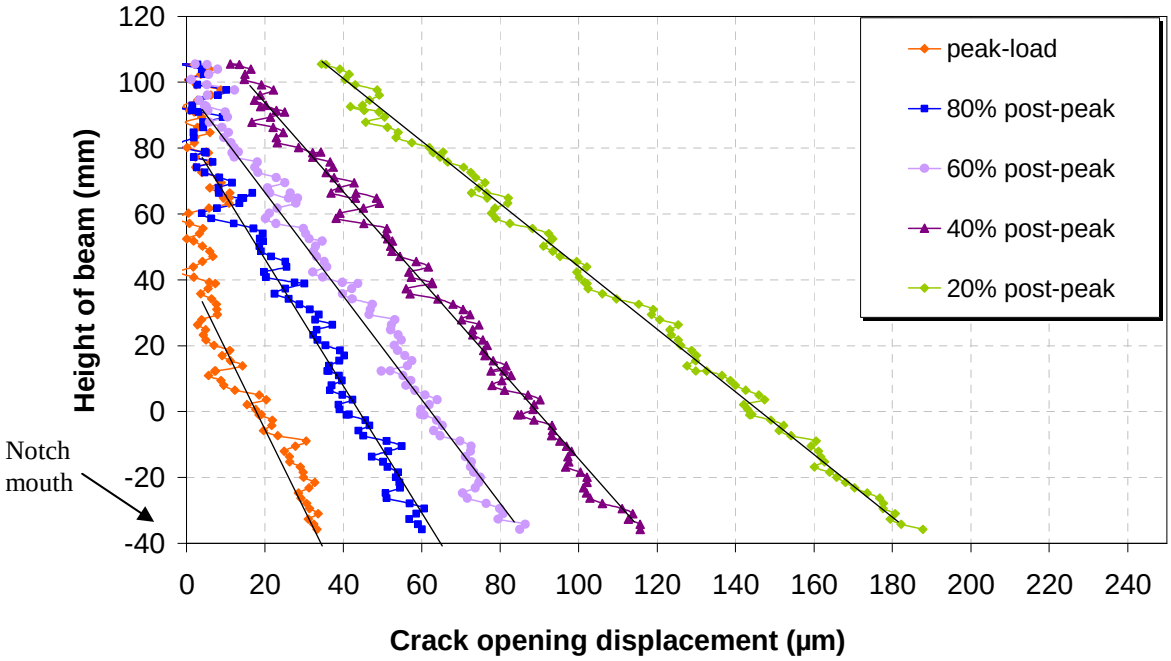

Figure 3.18 Linear interpolation of crack opening profiles (M1-D2 beam).

* Low resolution

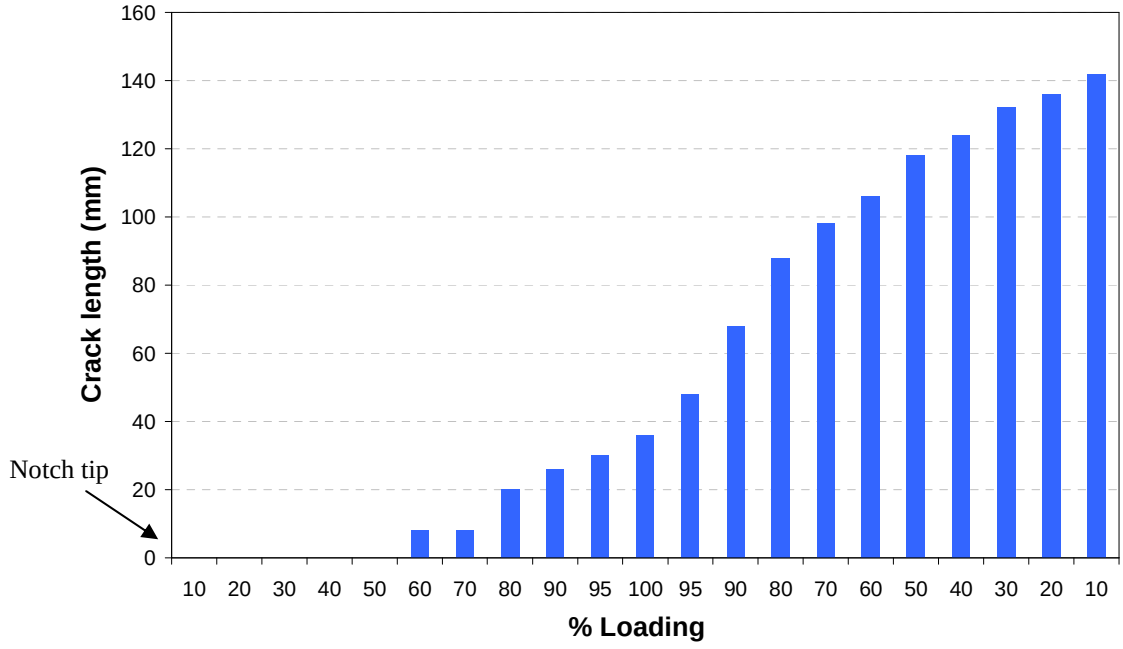

Figure 3.19 Evolution of crack length with the loading stages (M1-D2 beam).

* Low resolution

3.3.5 Crack bridging effect and tail softening

Crack interface bridging is a phenomenon in which crack surfaces are connected by weak ligaments. This phenomenon is responsible for the tail diagram of the Force-Notch mouth opening displacement curve in which large crack opening occurs (Figure 3.16). The evolution of the crack length is slower as compared to that in the early post-peak regime. This is due to the crack bridging phenomenon i.e. in the final loading stages, much energy is consumed in breaking the attached ligaments of the semi-crack parts of the concrete. This results in relatively less important crack extension. The beam loses its remaining strength gradually and a softening tail Force-Notch mouth opening displacement diagram is obtained. The beam fails finally when all the ligaments between the surfaces of the crack are broken.

3.3.6 Aggregate interlock and softening

The crack can sometimes be interlocked by an aggregate. This aggregate interlock or aggregate shielding is observed in our experimental study. An example of a M1-D2 beam presenting aggregate interlock is shown hereafter.

The interlock can occur at any loading stage. However, in the following example it has occurred near the peak loading stage (Figures 3.20 and 3.21). An aggregate particle usually comes into the path and causes the crack to deflect. Sometimes aggregate particles also break due to a higher stress state in that location. In this case, aggregate interlock occurs just in front of the notch and causes an immediate drop of the crack opening.

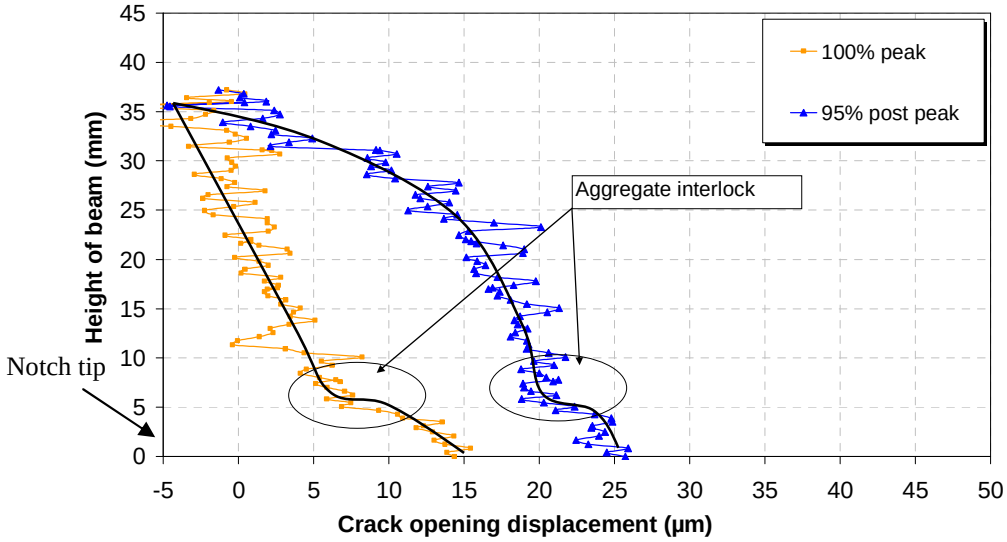

Figure 3.20 Crack opening profiles showing aggregate interlock (M1-D2 beam).

* High resolution

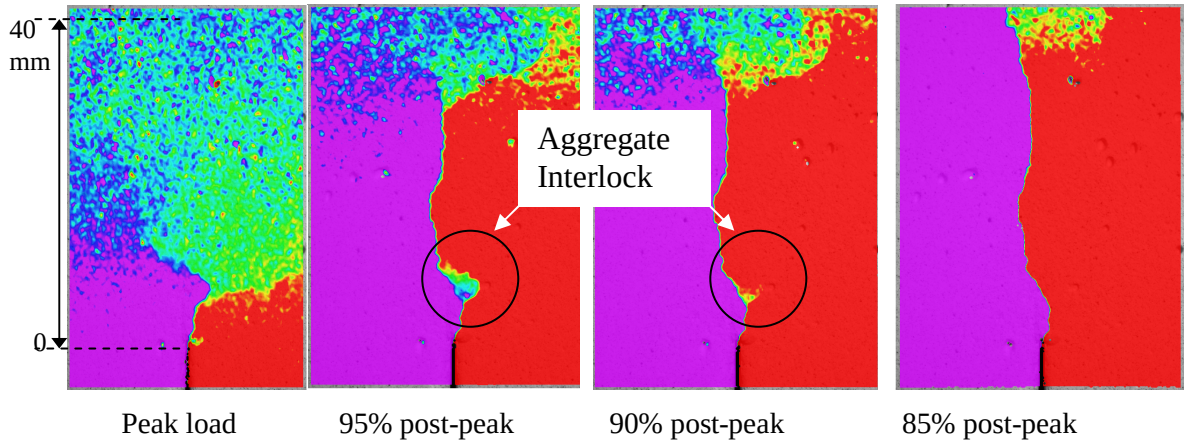

Figure 3.21 Crack propagation in a specimen showing aggregate interlock. (M1-D2 beam).
* High resolution (displacement field)

It can also be seen in the Force-Notch mouth opening displacement diagram (Figure 3.22) that the beam presents a softening behaviour at this particular loading stage. The softening of concrete is due to large crack openings. However, the crack extension is almost insignificant during the phase of aggregate interlock (Figure 3.21). Thus, more energy is consumed to break the crack interlock than to extend the crack. However, the crack continues to extend as soon as the aggregate interlock is resolved. In this case, crack interlock is resolved by crack deflection. We can see that the crack path at the interlock location is not the same for 100% peak load and 80% post-peak load i.e. when the aggregate interlock is resolved. It is also observed that after the crack extends rapidly, it attains a "normal" crack length similar to other specimens where no aggregate interlock is observed.

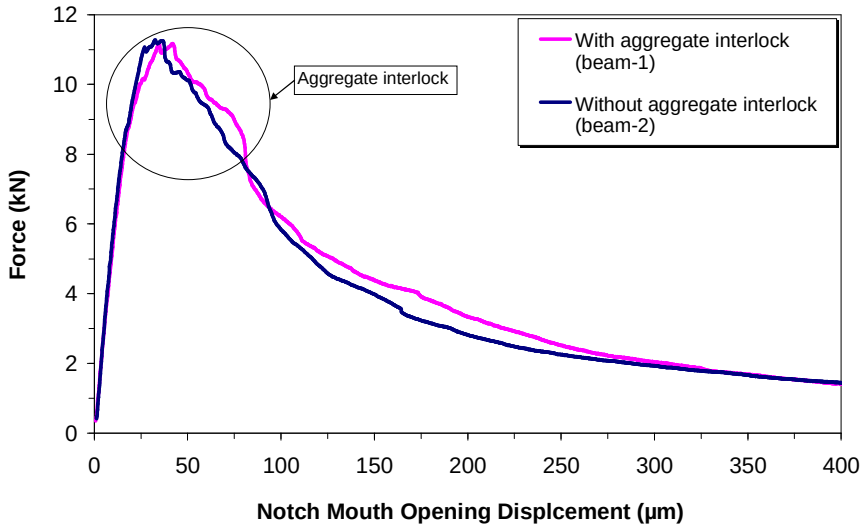

Figure 3.22 Comparison of the mechanical behaviour of beams with and without aggregate interlock (M1-D2 beams).

3.4 Influence of aggregate size on the fracture behaviour

In this section, the fracture behaviour of similar sized beams that are made of different concretes (M1 and M2), is discussed. In these concretes, the maximum size of aggregates is varied to study the influence of their size on fracture behaviour. The beams studied are the (small) D1 and (medium) D2 beams.

3.4.1 Influence on the mechanical behaviour

The mechanical responses of D1 and D2 beams are presented in Figures 3.23 and 3.24 respectively. The two concretes have the same initial slope. However, the peak load is considerably affected by the maximum size of the aggregate. It is observed, for both D1 and D2 specimens, that the peak load increases with the decrease of the aggregate size. However, it occurs at the same notch mouth crack opening.

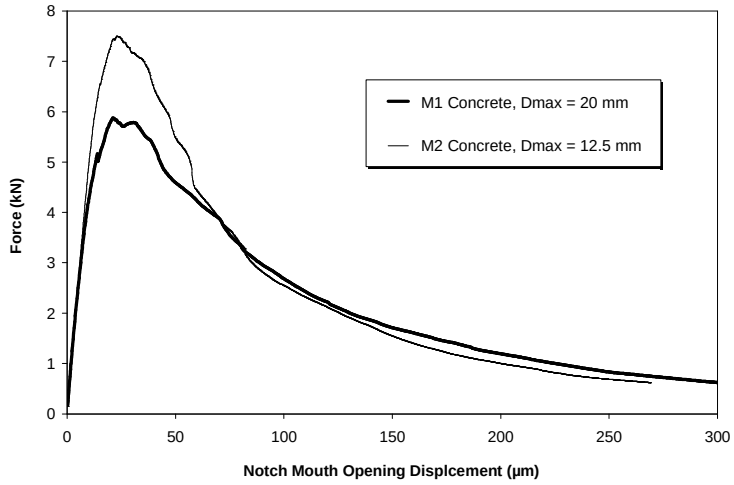

Figure 3.23 Average Force-Notch mouth opening displacement curves for the D1 beams.

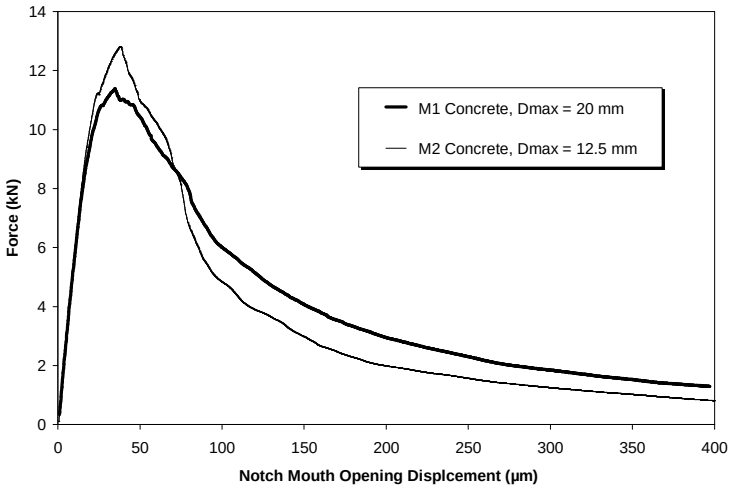

Figure 3.24 Average Force-Notch mouth opening displacement curves for the D2 beams.

The post-peak characteristics are different for the two types of concrete. For the M2 concrete which has smaller sized aggregates, the response is more brittle than for the M1 concrete. The load decreases sharply in the early post-peak regime for the M2 concrete. This brittleness is more pronounced in the D2 beam due to the size effect on the mechanical behaviour. Moreover, the tail softening curves for the two concretes are not the same. The residual tail strength of concrete due to the crack bridging effect is more important for the M1 concrete (especially for the D2 beam).

3.4.2 Influence on the crack length evolution

The crack length evolution diagrams for both types of concrete mixes are presented in Figure 3.25. In the pre-peak regime and at the peak load, the crack length in the M2-D2 specimen is bigger than in the M1-D2 specimen. In other words, the M2-D2 specimen with higher peak load (or nominal strength) corresponds to a longer crack. However, the crack length extension becomes more important for the M1-D2 concrete in the post-peak regime. At the final stage (10% post-peak) both specimens have a similar crack length. The same conclusion is found for the D1 specimen.

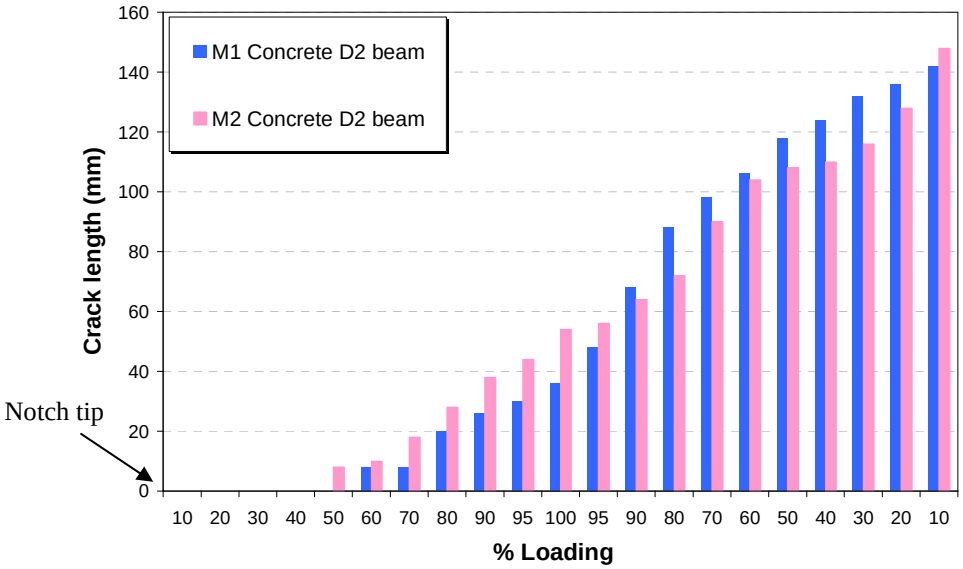

Figure 3.25 Evolution of crack length with the loading stages (M1-D2 and M2-D2 beams).

* Low resolution

3.5 Size effect on the mechanical behaviour

Heterogeneity has an important effect on the mechanical behaviour of concrete. In this experimental campaign, bending tests under the same loading conditions are performed on beams of three different sizes (D1, D2 and D3). In this section, the influence of the size effect on the mechanical results is analysed. The mechanical results due to three different ratios of the maximum size of aggregates to the

height of the beam, are used. In the next section, a size effect analysis is performed following the RILEM recommendations [12, 14, 107].

Figure 3.26 shows the relationship between the nominal stress and the notch mouth opening displacement for each specimen size. The nominal stress σ_N is calculated as:

$$\sigma_N = \frac{3P\,S}{2b\,D^2} \quad , \tag{3.1}$$

Where P is the applied load, S is the span of the beam, b is the width of the beam and D is the total height of the beam (including the notch length).

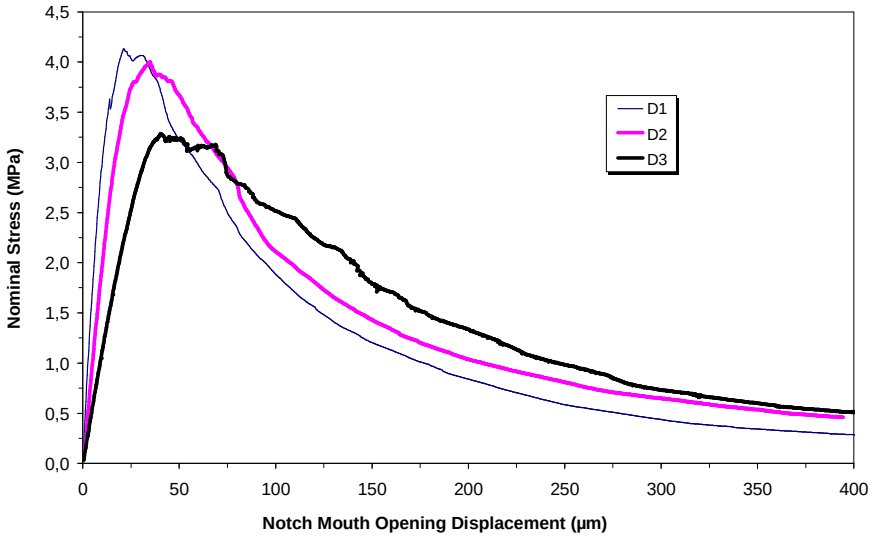

Figure 3.26 Average Force-Notch mouth displacement curves for the M1-D1, M1-D2 and M1-D3 beams.

It can be observed in Figure 3.26 that the relationship between the nominal stress and the notch mouth opening displacement is different for each specimen size. In the pre-peak regime, the notch opening is larger for the D3 as compared to the D1 specimen, regardless of the stress level. The difference becomes more important as the load increases. This is possibly due to the fact that the notch length is larger for the D3 specimen than for the D1 specimen. At peak load stage, a decrease in the nominal strength is observed with the increase of specimen size. This is the evidence of the famous size effect and is attributed to the presence of a FPZ of characteristic size ([7], see Section 1.4.2). More details on the size effect will be given in the following section as well as in Section 3.6.

In the early post-peak regime, a relative sudden drop in the nominal stress is observed. This drop may be due to the fact that damage has already occurred in the major part of the beam section. Another explanation will be given in Section 3.6 with the help of crack profiles. In the tail of the post-peak regime, the relationship between the notch mouth opening displacement and the nominal stress becomes quasi-similar for beams of all three sizes.

Another interesting observation is made in Figure 3.27. The notch mouth opening displacement at peak load is plotted for the three beam sizes. The size effect is obvious. More specifically, it can be observed that the size effect on the notch mouth opening displacement is important for the D1 to the D2 beams. The size effect on nominal strength, however, is less important. On the other hand, a strong size effect is present on the nominal strength between D2 and D3 beams, and a relatively less important size effect on the notch opening displacement.

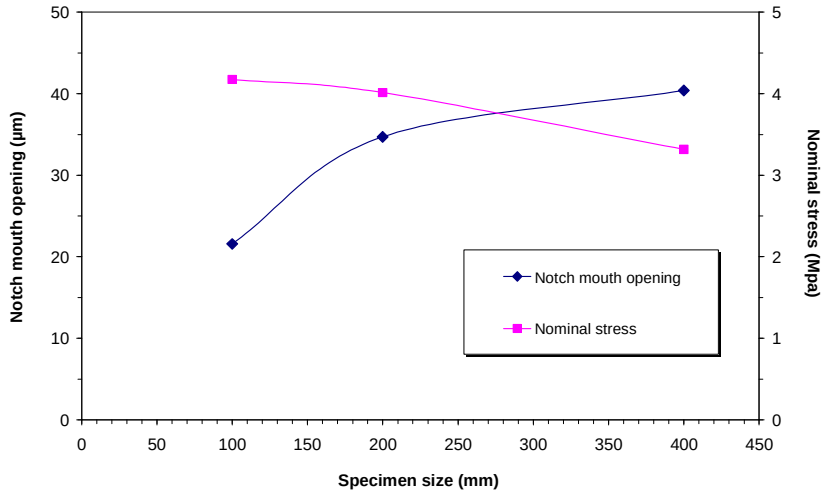

Figure 3.27 Size effect on nominal stress and notch mouth opening displacement at peak load.

3.5.1 Analysis of size effect according to RILEM size effect method

The analysis of the results according to according to RILEM size effect method is made in the following in two steps. First, the size independent fracture parameters are determined. Then an analysis of the results is made based on the experimental results and the Bazant size effect law.

3.5.1.1 Determination of fracture parameters

In our study, the size effect method recommended by RILEM is followed to determine the fracture parameters of the M1 concrete [107]. The calculation procedure adopted is the one provided by Bazant and Planas [14].

The measured maximum loads P^0_i for the three sizes of beams are given in Table 3.1. The loads are corrected to take into account the weight of the specimens. The corrected maximum loads P_i are calculated using the following expression:

$$P_i = P_i^0 + m_i\, g(2S_i - L_i)/2S_i \quad , \qquad i = 1,2,3 \tag{3.2}$$

Where $m_i\, g$ is weight of the beam, S_i is the span and L is length of the beam.

Table 3.1 Results of three point bending tests at peak load for M1 concrete.

Size	*b* mm	*D* mm	*S* mm	*L* mm	*a* mm	*m* kg	P^0 N	*P* N	σ_N MPa
D1	100	100	300	400	20	9.57	5846	5877	2.64
						9.63	5928	5959	2.68
						9.46	5942	5973	2.69
D2	100	200	600	800	40	38.95	10451	10578	2.38
						38.10	11183	11307	2.54
						38.30	12247	12372	2.78
D3	100	400	1200	1600	80	153.6	18158	18660	2.10
						150.4	18575	19066	2.14
						152.1	19333	19830	2.23

The nominal strength σ_N is then calculated, based on the corrected ultimate load for each specimen as

$$\sigma_{Ni} = \frac{3P_i\, S_i}{2bD^2} \quad , \qquad i = 1,2,3 \tag{3.3}$$

The above data is plotted to obtain a linear regression curve (Figure 3.28). The coordinates of the data points are

$$X_i = D_i \qquad and \qquad Y_i = \left(1/\sigma_{Ni}\right)^2 \tag{3.4}$$

Where D_i are the sizes corresponding to P_i.

The regression curve presents the Bazant size effect law (Equation 1.3). We can see that the experimental results do not truly present a linear relation between D and $1/\sigma_N{}^2$. Actually, the results can be interpolated with a curve which is convex upwards.

The slope A and intercept C (with the Y axis) of the regression line are calculated in the following way:

$$A = \frac{\sum\sum_{xy} - \sum_{x}\sum_{y}}{\Delta}, \qquad C = \frac{\sum_{xx}\sum_{y} - \sum_{x}\sum_{xy}}{\Delta} \tag{3.5}$$

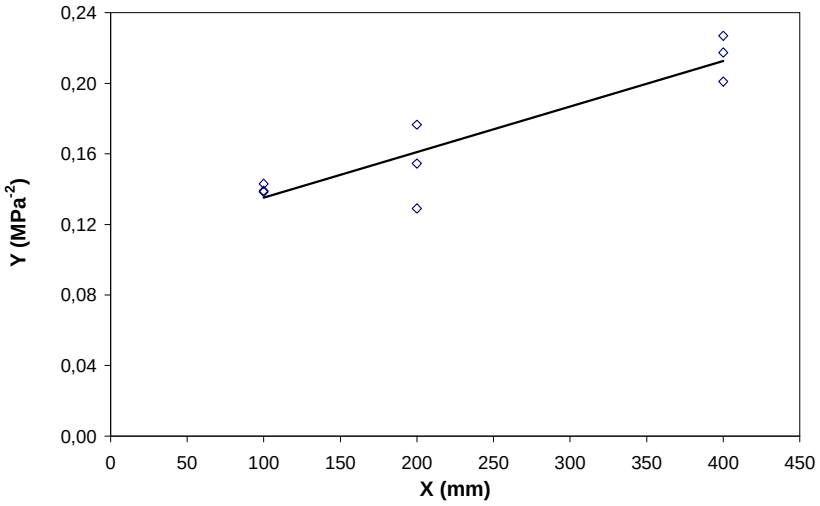

Figure 3.28 Linear regression curve of the nominal strength values for M1 concrete.

Where,

$$\Delta = \sum\sum_{xx} - \left(\sum_{x}\right)^2 \tag{3.6}$$

and

$$\sum = \sum_{i=1}^{3} 1^i = 3, \qquad \sum_{x} = \sum_{k=1}^{3} X_i, \qquad \sum_{y} = \sum_{k=1}^{3} Y_i$$
$$\sum_{xx} = \sum_{k=1}^{3} (X_i)^2, \qquad \sum_{xy} = \sum_{k=1}^{3} X_i\, Y_i \qquad \sum_{yy} = \sum_{k=1}^{3} (Y_i)^2 \tag{3.7}$$

The shape factor for a span to depth ratio S/D is calculated as:

$$k_{S/D}(\alpha) = \sqrt{\alpha}\,\frac{p_{S/D}(\alpha)}{(1+2\alpha)(1-\alpha)^{2/3}} \quad , \qquad p_{S/D}(\alpha) = p_{\infty}(\alpha) + \frac{4D}{S}\left[p_4(\alpha) - p_{\infty}(\alpha)\right] \tag{3.8}$$

Where,

$$p_4(\alpha) = 1.900 - \alpha\left[-0.089 + 0.603(1-\alpha) - 0.441(1-\alpha)^2 + 1.223(1-\alpha)^3\right] \tag{3.9}$$

and

$$p_{\infty}(\alpha) = 1.989 - \alpha(1-\alpha)\left[0.448 - 0.458(1-\alpha) + 1.226(1-\alpha)^2\right] \tag{3.10}$$

The values of k_0 (for $\alpha = a/D$) and dk_0 / da are calculated from the above formulae. Numerical differentiation is performed to obtain dk_0 / da. Finally, the fracture parameters are calculated using the following expressions:

$$K_{IC} = k_0 \frac{1}{\sqrt{A}} \quad , \qquad G_f = \frac{k_0^2}{E'} \frac{1}{A} \quad , \qquad c_f = \frac{k_0}{2(dk_0 / da)} \frac{C}{A}, \qquad D^\circ = \frac{C}{A} \tag{3.11}$$

The coefficients of variation of A and C, i.e. w_A and w_C, and the relative width of the scatter band m are determined as:

$$w_A^2 = \frac{1}{A^2} \frac{\chi^2 \sum}{(n-2)\Delta} \quad , \qquad w_C^2 = \frac{1}{C^2} \frac{\chi^2 \sum_{xx}}{(n-2)\Delta} \quad , \qquad m^2 = \frac{(n-1)\chi^2 \sum \left(\sum_x\right)^2}{(n-2)\Delta \left(\sum_y\right)^2} \tag{3.12}$$

Where n = number of specimens = 3 and

$$\chi^2 = \sum_{yy} - A\sum_{xy} - C\sum_y$$

According to RILEM recommendations, the value of w_A should not exceed 10% and the values of w_C and m 20%. The coefficients of variation of the fracture parameters are finally estimated as:

$$w_{KIC} = \frac{1}{2} w_A \quad , \qquad w_G = \sqrt{w_A^2 + w_E^2} \tag{3.13}$$

Where w_E is the coefficient of variation of E (Young modulus). In our case w_E is considered equal to zero.

3.5.1.2 Analysis of size effect on peak load based on Bazant size effect law

Table 3.2 Fracture parameters of M1 concrete according to RILEM size effect method [107]

D^0	β	Bf_t	l_{ch}	c_f	G_f	K_{IC}	w_A	w_C	m	w_{KIC}	w_G
(*mm*)	(*mm*)	(*MPa*)	(*mm*)	(*mm*)	(*N/m*)	(*MPa*√*m*)	(%)	(%)	(%)	(%)	(%)
423.3	409.5	3.02	250.2	77.5	60.2	1.51	16	10	0.7	8	16

Table 3.2 presents the different fracture parameters determined from the RILEM size effect method. The coefficients of variation are in the acceptable range, except for w_A, which may be due to the

inherent material heterogeneity. However, many experimental data widely accepted in literature show a similar variation (e.g. [12] B3 concrete).

According to the method, $D°$ is the characteristic dimension of the structure located at the transitional point between linear elastic fracture mechanics and strength based mechanical laws. In our case, this value is larger than the height D of the largest specimen used, something which indicates that a more ductile behaviour should be expected for all beams. The brittleness number can also be calculated from Equation 1.4 and is found equal to 0.24, 0.47 and 0.95 for *D1*, *D2* and *D3* respectively. Therefore, the specimens lie in the intermediate stage between plastic behaviour ($\beta \leq 0.1$) and the transition state ($\beta = 1$). This type of behaviour is very important because it is the behaviour of the concrete used in construction sites.

The values found for the characteristic lengths c_f and l_{ch} are evidence of a large sized FPZ. This is probably due to the large aggregate size used in the concrete. According to the Bazant size effect law, the effective fracture process zone length c_f is the distance from the notch tip to the tip of the equivalent LEFM crack in an infinitely large specimen; or it is half of the FPZ length ahead of the real crack. l_{ch} is the characteristic length of the material. In the fictitious crack model [51] it is considered as the length of the FPZ. Irwin defined it as the length in which the material undergoes plastic deformation. For concrete, the material does not show a rectangular yield plateau in front of the crack. This is the reason why Hillerborg [51] using Irwin's expression, estimated the length of the FPZ zone of triangular or concave-upward shape. Therefore, one will get a higher l_{ch} as compared to the actual damaged zone. G_f is the fracture energy of the material and is considered as a material property. If we consider that G_f is a function of the crack length that changes when the crack approach the boundaries ([38, 56], see also Chapter 1), we can conclude that Irwin's characteristic length is not constant but is a function of the crack length.

$$l_{ch} = \left(\frac{K_{IC}}{f_t'} \right)^2 = \frac{E' G_f}{f_t'^2} \tag{3.14}$$

According to Bazant's size effect law, the fracture energy G_f is defined as the energy required for a unitary crack growth in an infinitely large specimen. He assumed that a linear relationship exists between $(1/\sigma_N)^2$ and D (the regression line in Figure 3.28). In the expression of fracture energy (Equation 3.11), k_0 is the value of $k_{S/D}$ for α where α is the ratio of the notch length to specimen height. By applying this to an infinite large dimension, Bazant calculated the fracture energy as the critical energy release rate according to linear elastic fracture mechanics (see Equation 1.7).

Bazant's size effect curve is presented in Figure 3.29. It can be seen that the size effect on the nominal strength is not very pronounced between D1 and D2, but more prominent between D2 and D3. Bazant's size effect law (Equation 1.3) represents a smooth transition between D1, D2 and D3. The size effect curve passes well through the large specimen results (specimen near to the LEFM line), but a slight discrepancy is present for D1 and D2 specimens. This might show some inadequacy of the Bazant size effect in this experimental range.

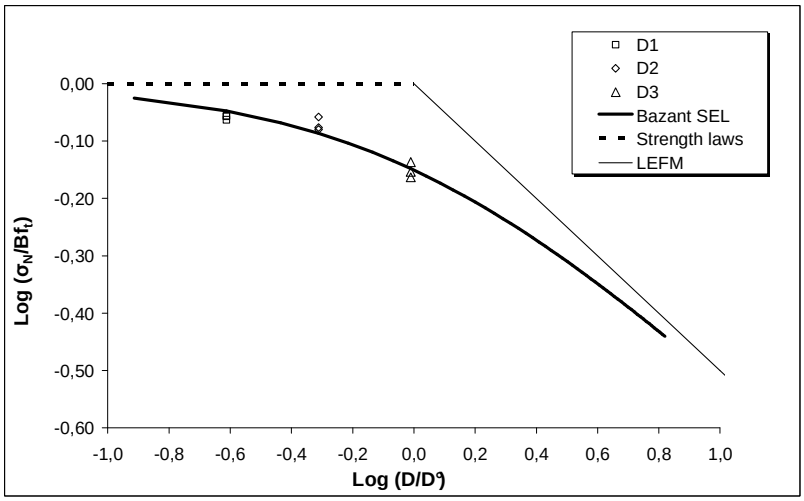

Figure 3.29 Size effect curve between non-dimensional nominal strength and size of the beams.

3.6 Size effect on crack opening

In this section, the crack profiles for the three sizes of beams, obtained from DIC analysis at different loading stages, are studied. Size effect is investigated in terms of crack opening displacement and crack length at the same loading conditions (i.e. % of maximum force) or in terms of loading conditions at the same fracture state.

3.6.1 Size effect on crack initiation

The crack always initiates from the weakest link in the material. Since the beams are notched, the crack starts from the notch tip. This is the reason why the crack opening at the notch tip is analysed hereafter.

Figure 3.30 presents the evolution of the crack opening displacement rate at the notch tip for the three beams. For the D1 beam, an increase in the rate of the crack opening is observed at about 50% of the peak load. After this point, a small decrease occurs and then a continuous increase in the crack opening rate is observed until 95% F_{max} in the post-peak regime. This shows that for the D1 beam the

crack initiates at 50% in pre-peak regime and then continues to grow gradually. For the D3 specimen, the crack opening rate increases suddenly just before the peak load. A similar observation is made for the D2 specimen. In other words, the crack initiates just before the peak load for the D2 and D3 specimens. Thus, an apparent size effect is present on the crack initiation.

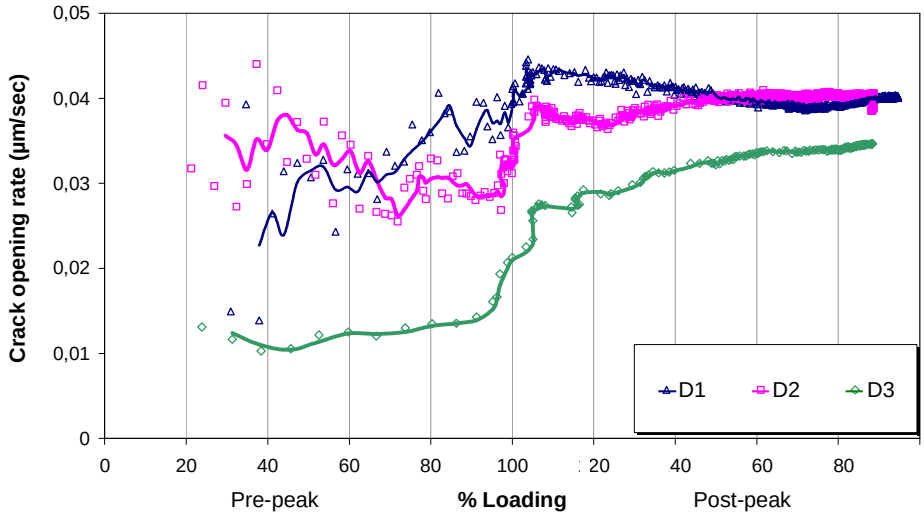

Figure 3.30 Evolution of the crack opening displacement rate at the notch tip with the loading stages for the three beam sizes.

3.6.2 Size effect on crack opening profile at peak load

In Figure 3.31, the crack opening profiles at peak load for the D1, D2 and D3 beams are presented. It can be seen that all the specimens show similar crack profiles (no size effect).

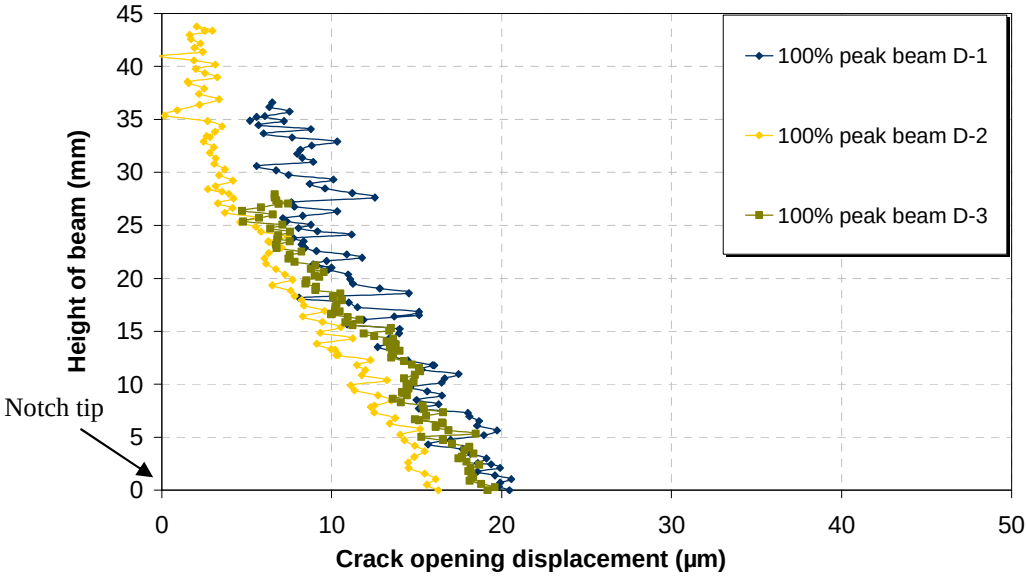

Figure 3.31 Size effect on crack opening profile at peak load for three sizes of M1 beams.

* High resolution

3.6.3 Size effect on crack length

The crack length can be estimated from the crack opening profiles. In Figure 3.32 the relative crack length (L_{crack}/D) at different loading intervals for each specimen size is plotted. It is the ratio of the length of crack from the notch tip (L_{crack}) to length of specimen from notch tip (H). It can be seen that the formation of the crack starts before the maximum load is reached. For the smaller specimen D1, the crack initiates at a lower loading in the pre-peak regime as compared to the larger specimen D3.

In Figure 3.32 the crack growth in D1 specimen can be divided into three stages. The first stage is from the crack initiation to 95% F_{max} in the post peak regime. In this stage, the crack growth is smooth. In the second stage i.e. between 95% F_{max} to 80% F_{max} in the post peak regime, the crack growth is relatively abrupt and the crack length is almost doubled. In the last stage, the crack propagation is relatively slow.

The crack growth in D3 beam is relatively smooth. We can observe that the initiation of the crack is delayed and the crack grows in the same way in the subsequent loading stages. We can also see that the relative crack length in the D1 specimen is bigger as compared to D2 and D3. This shows a significant size effect on the crack length. Just before the rupture of the specimen, the relative crack length is almost the same for all the specimens.

According to the original version of Bazant size effect law [7], the crack length at peak load, in concrete specimens of varying sizes, is proportional to the height of the specimen (and equal to the notch). This is not found here, as the crack lengths at peak load are not proportional to their respective specimen sizes.

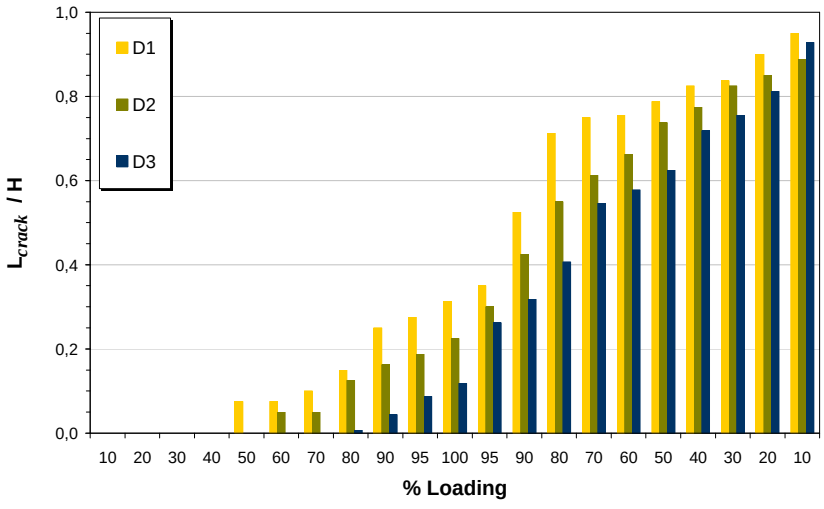

Figure 3.32 Evolution of the relative crack length (crack length from notch tip/specimen height from notch tip) with the loading stages for the three sizes of beams. *Low resolution

3.7 Case study: Crack openings in reinforced concrete and size effect

Serviceability limit states (SLS) for reinforced concrete (RC) structures are usually applied to ensure their functionality and structural integrity under service loading conditions. In current design codes (EC2 EN 1992 [40]), the serviceability limit states are defined by providing three control parameters (1) Limitation of stresses in the material (2) Control of crack openings and spacing (3) Deflection (short term and long term) checks. The maximum stresses, deflections and crack openings are computed from critical combinations of actual applied loads (called service loads), in conjunction with the structure's geometry (type and location of reinforcement) and boundary conditions. In this section, an experimental study is presented, in which three geometrically sized beams are tested in three point bending. Experimental crack openings and crack spacing are obtained, when the structure is subjected to service loadings. A bibliographic study on the crack control and size effect on crack openings in RC structures is first presented. Then, the experimental setup is explained and lastly, the results are analysed.

3.7.1 Crack control in RC structures

It is recognized that cracking in reinforced concrete members may be of two forms: (1) cracking due to restraint provided by structure to volume change, and (2) cracking due to applied loads. In this section, only the cracking due to applied loads is discussed.

There are three principal elements in the provisions of crack control (EC2 EN 1992 [40]): (1) the provision of minimum reinforcement area (2) a method for calculating design crack opening and (3) simplified rules which will avoid the necessity for explicit calculation of crack opening in most normal situations.

3.7.1.1 Design crack opening

The approach almost universally used to explain the basic cracking behaviour of reinforced concrete is to consider the cracking of a concrete prism that is reinforced with a central bar which is subjected to pure tension. Bending does influence the phenomena but this is dealt with in the Eurocode [40] by an empirical adjustment of the coefficients.

According to Eurocode (EC2 EN 1992 [40]), the design crack opening can be determined using the following expression

$$w_k = s_{r,\max}\left(\varepsilon_{sm} - \varepsilon_{cm}\right) \tag{3.15}$$

Where,

w_k is design crack opening; $s_{r,max}$ is maximum crack spacing; ε_{sm} is mean strain in the reinforcement and ε_{cm} is mean strain in concrete between cracks.

In the expression (Equation 3.15) ε_{sm} - ε_{cm} may be calculated as:

$$\varepsilon_{sm} - \varepsilon_{cm} = \frac{\sigma_s - k_t \dfrac{f_{ct,eff}}{\rho_{p,eff}}\left(1 + \alpha_e \rho_{p,eff}\right)}{E_s} \geq 0.6\frac{\sigma_s}{E_s} \tag{3.16}$$

Where,

σ_s is stress in the tension reinforcement assuming cracked section and $\rho_{p,eff}$ is $A_s/A_{c,eff}$, which is the ratio of area of tension reinforcement (A_s) to the effective tension area of concrete around the steel ($A_{c,eff}$). However, $A_{c,eff}$ depends implicitly upon the concrete cover provided on the tension face. See details in EC2 EN 1992 [40].

3.7.1.2 Maximum final crack spacing

According to Eurocode (EC2 EN 1992 [40]) when reinforcement is fixed at a reasonably closed spacing (spacing ≤ 5(c+Φ/2)), the maximum final crack spacing can be calculated as:

$$s_{r,\max} = 3.4c + 0.425 k_1 k_2 \frac{\phi}{\rho_{p,eff}} \tag{3.17}$$

Where,

Φ is bar diameter; c is concrete cover and k_1 and k_2 are the coefficients depending upon steel-concrete bond properties and loading type respectively. See EC2 EN 1992 [40] for details.

In Equation 3.17, concrete cover c is explicitly introduced into the expression of the crack opening as suggested by A. Beeby [16, 17]. Beeby studied the influence of concrete cover on the transfer length. The transfer length increases monotonically with the increase of concrete cover. This effect is introduced in the calculation of crack spacing. Stress in the concrete around the reinforcement is

directly dependent on the stress transfer length between concrete and steel. Since cracking in concrete occurs at the points where stress exceeds the tensile resistance of concrete, therefore, crack spacing is a function of concrete cover. In this study, the ratio of concrete cover to height of the beam is kept constant in order to take into account the effect of overall structure size on the crack opening and crack spacing.

3.7.1.3 Analysis of test data

It has been suggested that when analyzing the test data of crack opening and crack spacing in reinforced concrete tensile members, the following considerations should be made (commentary to EN 1992 [60]):

- The materials to be used should be similar to the materials in use today in the building structures. The low bound rebars, concrete qualities less than 20 N/mm^2 and steel qualities less than 400 N/mm^2 should not be used.

- The stress range should be serviceability range. For this purpose, results in the stress range of steel from 150 to 350 N/mm^2 should be considered for tests involving direct actions. For indirect actions, steel stress range up to the yielding stress of steel should be considered.

- To determine the crack spacing, the number of cracks present at the last phase of the test is always considered since it is the closest to the stabilized cracking, as given by Equation 3.17.

In the literature a very little data is found for the direct comparison between the calculated and the experimental crack widths.

3.7.2 Size effect on crack opening in RC structures

It is obvious that the cracking behaviour is also influenced by structural size. This has already been demonstrated in the previous sections of this chapter. A numerical study of reinforced concrete based on fracture mechanics rules has also shown cracking behaviour to be size dependent [95]. Crack opening was calculated in tensile members who had constant central reinforcement and member length, but varying cross sectional areas. It was found that crack opening decreases as the width of the member increases. Results were not compared with experimental data. They found that previously obtained experimental data is very scattered because crack opening depends not only on the geometry and loading condition of the structure, but also on the size of the structure. In the current design

approach (Equation 3.15 and 3.16) crack opening is evaluated using primarily empirical methods that require some empirical constants. The size effect on the crack opening cannot be accounted for by the conventional analysis unless additional empirical constants are used [114].

A limited amount of experimental data is available in literature, concerning the study of size effect on the crack opening and crack spacing in RC members. Most of the results deal with reinforced concrete members which have been subjected to tension or which have small dimensions [60]. In this section, an experimental program is presented in order to study the effect of structural size on crack opening and crack spacing. Three sizes of beams with geometrically similar length and height, but with constant thickness, are tested in three-point bending. The tensile reinforcement ratio is kept constant. However, the concrete cover to the reinforcement is scaled according to the overall size of the beam. The aim of this study is to evaluate the design crack opening and crack spacing expressions present in the Eurocode (Equations 3.15-3.17), with the experimentally measured crack width and spacing.

3.7.3 Experimental program

3.7.3.1 Materials

The concrete used to prepare the beams is mix M2 (see Tables 2.1 and 2.2). The longitudinal reinforcement of beams is constituted of deformed bars which are 10, 14 & 20*mm* in diameter, while the transverse reinforcement is provided by deformed bars which are 6*mm* in diameter. The steel bars in both cases are type $f_{yk} \geq 500$ MPa.

3.7.3.2 Beams geometry

Three sizes of beams are tested. The dimensions of the beams are given in Table 3.3. The beams have a constant width (b = 100*mm*), however, the length and height are scaled. The concrete cover at the tension face of the beam is also scaled with the same proportion between different sizes of beams. The beams are reinforced with a constant reinforcement ratio by varying the diameter of the bars. The number of bars, however, is kept constant. Steel stirrups are used in the area of high shear. Two hanger bars of 6*mm* diameter are used to support the steel stirrups. These bars are cut where the stirrups are not provided (Figure 3.33).

Table 3.3 Specimens' geometry.

Beam	*b*	*h*	*L*	*l*	*ρ*	cover
	mm	*mm*	*mm*	*mm*	%	*mm*
Small-D1	100	100	400	300	1.99	10
Medium-D2	100	200	800	600	1.84	20
Large-D3	100	400	1600	1200	1.83	40

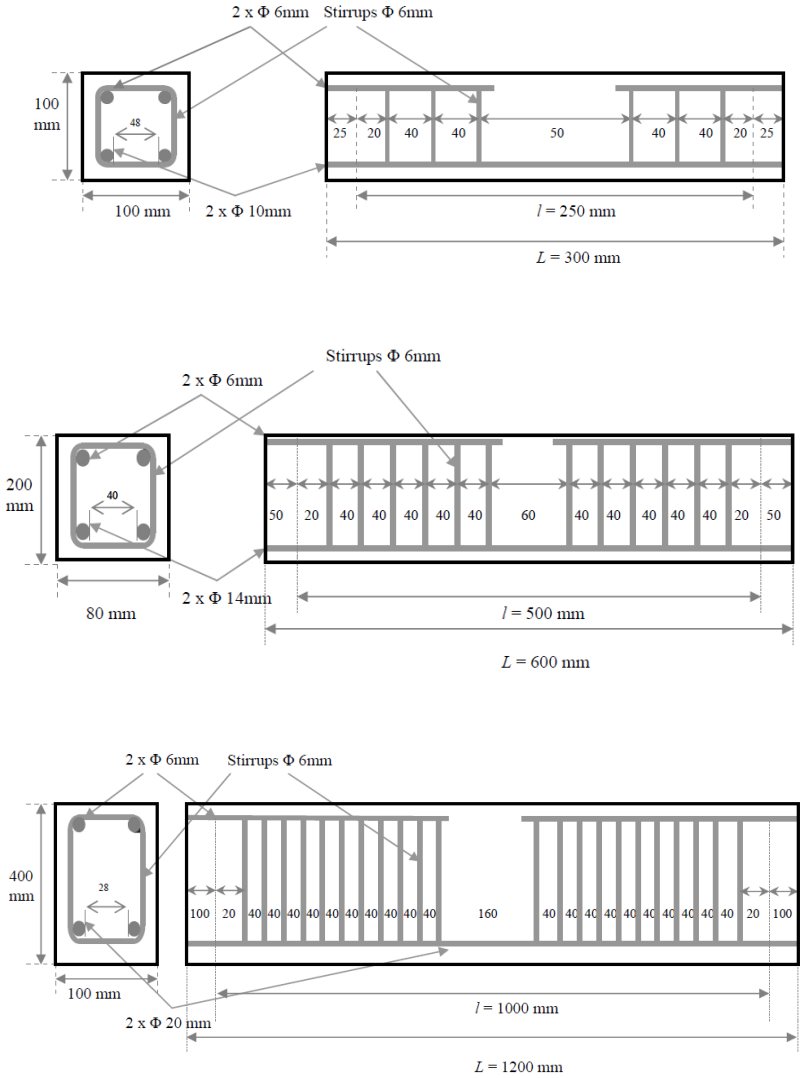

Figure 3.33 Geometry and reinforcement details.*

* The figure is not scaled.

3.7.3.3 Test procedure

All the experiments are performed using the same testing machine with controlled displacement. The test setup is shown in Figure 3.34. The load is applied at the mid span with a cylindrical jack, ensuring the point load. The load is transferred to the beam using a rubber pad, to avoid the concrete damage at the load point. The test is carried out using a constant vertical displacement rate of 0.5 *mm*/*min*. The displacement is measured using a laser sensor, which measures the displacement at the mid section of the beam under the load. The sensor is attached to a steel hanger, which is supported at the supports, to take into account the settlement of the beam at the supports.

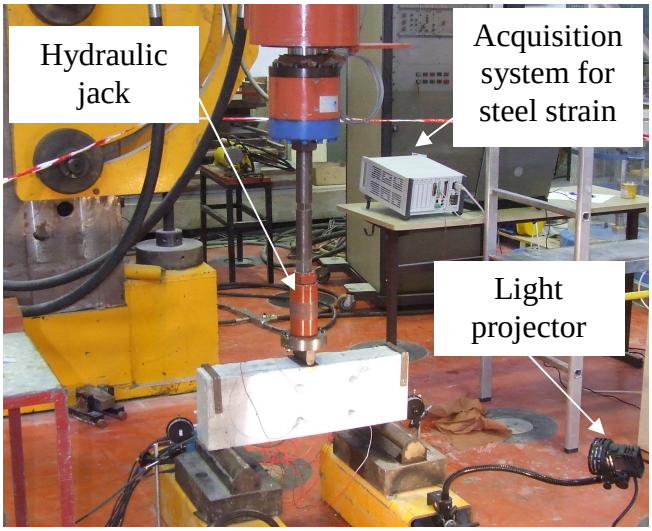

Figure 3.34 Test setup.

For each beam, two electric strain gauges are attached to the lower face of the tension steel at mid span. This is done to measure the longitudinal strain in the steel during the test (Figure 3.35).

Results are discussed here for three point bending tests on three sizes of beams. After the fabrication, these beams are stored at a temperature of 20°C and a relative humidity of 50% for 24 hours. After the removal of the moulds, these beams are stored in 100% relative humidity for 28 days.

Figure 3.35 Strain gauges attached to the steel bars at mid span.*

*View before the pouring of concrete

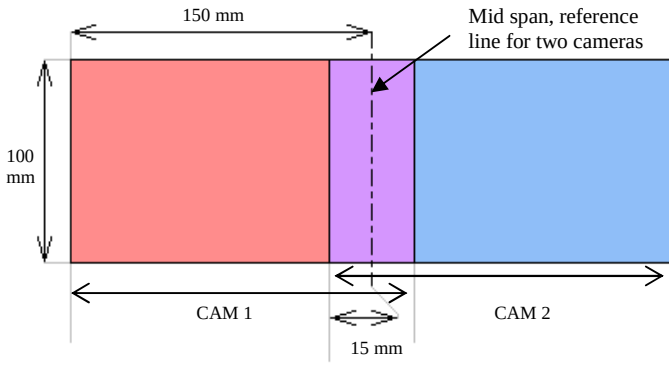

Figure 3.36 Camera zones for digital image correlation.

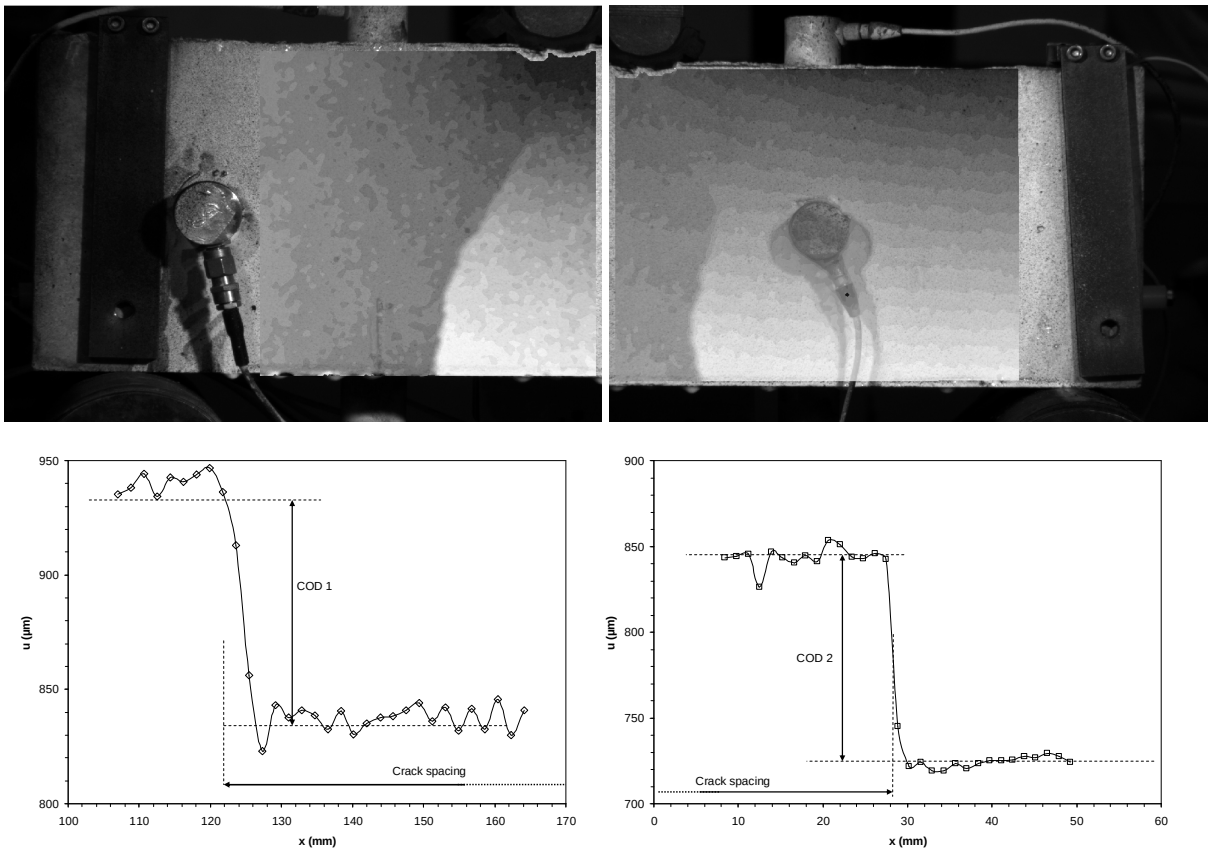

Figure 3.37 Measurement of crack opening displacement (COD) and crack spacing in small (D1) beam.

Digital image correlation technique is used to measure the crack openings and crack spacing. The correlation parameters used are the same (see Chapter 2). The images on a single face of the specimen are captured using two digital cameras, which give 256 levels of gray intensity. The cameras are placed in such a way that an area 15x10 *cm* is filmed by each camera on either side of the mid span. The mid span portion is filmed by both cameras. The mid span section is taken as a reference to relate the measurement values of the two cameras (Figure 3.36). The measurement of crack opening displacement (COD) and crack spacing by digital image correlation is presented in Figure 3.37. COD

is measured as the displacement jump on the surface of the beam. The procedure in describe in Section 3.2. Multiple cracks are found, but only the maximum COD is considered in the further analysis. The crack spacing is measured as the distance between the centre lines of the displacement jumps (see Figure 3.37).

3.7.4 Results and discussions

In Figure 3.38, the crack opening measured using digital image correlation technique is plotted as a function of steel strain ε_{sm} against the crack opening, which is obtained using the Eurocode 2 crack opening formula (Equation 3.15). The crack opening is measured at the mouth of the crack i.e. at the lowest fibre of the beam where the crack opening is maximum. It can be seen in Figure 3.38 that the Eurocode 2 formula underestimates the crack width for all the three sizes. The difference between measured and calculated value increases when the strain is higher. Figure 3.39 shows the comparison between measured and calculated values, for a stress range under the yield limit of steel.

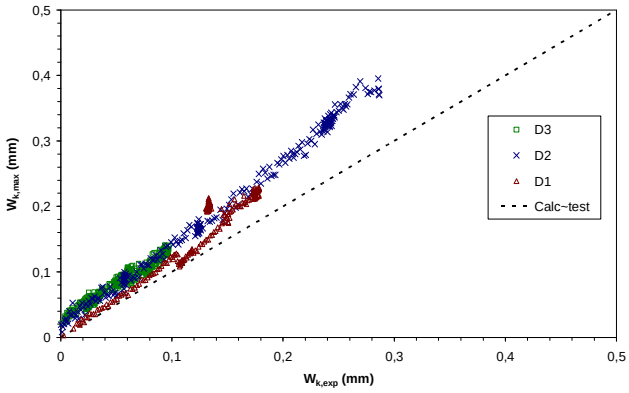

Figure 3.38 Comparison of experimental crack opening ($W_{k,exp}$) and calculated maximum crack opening ($W_{k,max}$) during crack formation stage (ε_{sm}< yield limit).

A more detail observation of the effect of size on the Eurocode 2 calculated crack opening is made in Figure 3.38. The crack openings are calculated in the stress range under the yield limit of steel. It is clear that the calculated crack opening is more or less comparable for a small sized beam but the error increases with an increase in size.

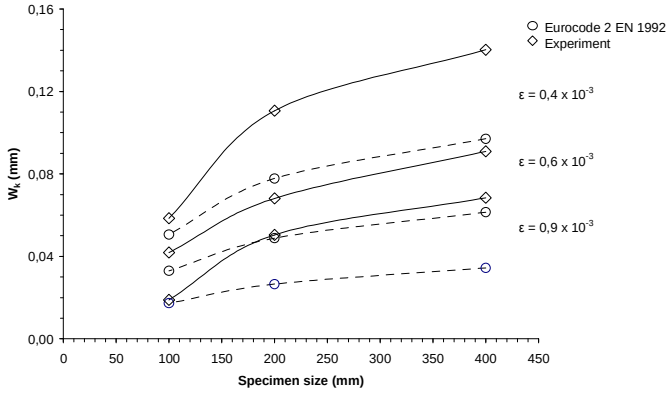

Figure 3.39 Size effect on experimental and calculated maximum crack opening.

The crack opening obtained from the Eurocode 2 formula does not take into account the size effect. The calculated values are different for the three sizes of beams (Figure 3.39), but this should not be considered as size effect, as the Eurocode 2 formula depends only on the concrete cover and diameter of the bars. The true size effect, however, is the effect of the dimensions of the structure on the overall fracture mechanism. As the structure becomes sufficiently large, the size of the heterogeneity becomes negligible compared to the size of the structure and the material follows brittle failure. However, when the size of the structure becomes sufficiently small, the size of the heterogeneity becomes comparable to the size of the structure and the material and the material follows the ductile failure.

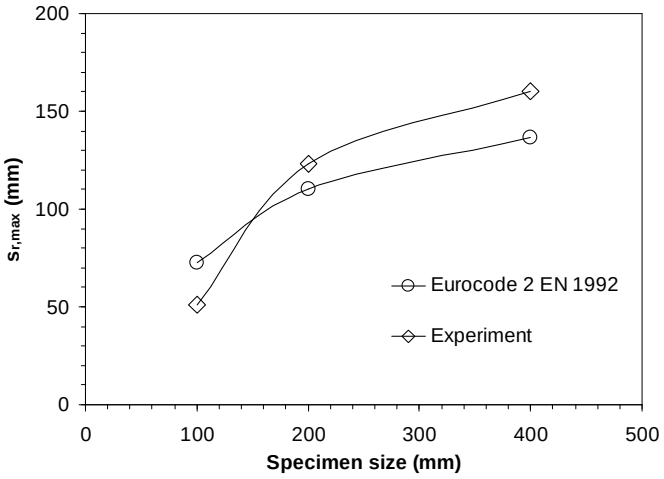

Figure 3.40 Maximum spacing of cracks, comparison of measured values with the calculated values.

The maximum spacing between cracks is also measured when steel stress is equal to 300 N/mm^2. In Figure 3.40 this spacing is compared with the spacing obtained from the Eurocode 2 formula (Equation 3.17). It is seen that for the medium (D2) and large (D3) sized beams, Eurocode 2 underestimates the crack spacing.

Conclusion

This chapter was focused on the crack growth in three sizes of geometrically similar beams, using DIC technique. A procedure was developed in order to obtain crack openings from the displacement field. The fracture process was identified by monitoring the crack openings. In the elastic phase, the crack openings were very small (1-5µm). The crack openings started to increase rapidly after about 60% of peak load in the pre-peak regime. In the post-peak phase, two stages were identified. In the early post-peak stage, the crack openings increased with a considerable decrease in the loading capacity. In the tail part of the post-peak regime, the crack openings in the lower part of the crack significantly increased, with a relatively gradual decrease in the load bearing capacity. This was attributed to the breakage of the remaining links of the semi-cracked zones.

Crack length was also estimated from crack opening profiles. It included the length of the macrocrack and some part of the microcracking zone in which rack openings were not negligible. It was assumed that this crack length plays a significant role in the decrease of the load bearing capacity. It was found that (1) crack length in the pre-peak region was identical in all the beams and did not vary in proportion to the size of the beam. Thus, for a smaller beam (with higher σ_N), longer relative crack length was observed. (2) In post peak region, two stages of crack propagation were observed. During early post-peak, the length of the crack increased rapidly up to 50% of the peak load. However, in the final post-peak region, crack opening became more important than the crack length propagation. (3) In the D1 specimen during the post peak regime, crack length propagation was relatively slower due to the boundary effect. (4) When aggregate size was reduced, a higher peak resistance was obtained, and the corresponding relative crack length measured at peak load was also higher. This conclusion is similar to (1) that higher resistance corresponds to a longer relative crack length.

A case study is also presented in which crack openings and crack spacing in reinforced concrete beams under three point bending tests were monitored. The experimental results were compared with the design values from Eurocode 2. It was observed that (1) Eurocode 2 underestimates the crack openings for all sizes of the beams. As the strains in the rebars increased, the difference between the measured and the calculated (Eurocode 2) values increased. (2) An important size effect on the measured crack openings was observed while keeping the strain level constant in different sizes of the beams. This size effect was not considered in the Eurocode 2 crack control expressions. Therefore it was not well captured in the calculated crack openings. (3) Another size effect was observed on the maximum spacing between the cracks. The Eurocode 2 expression underestimates the crack spacing when the size of the specimen increases.

Chapter 4

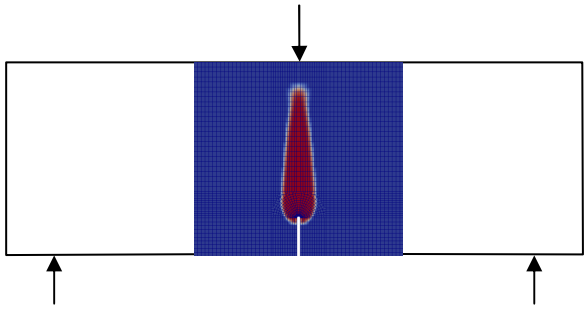

Modelling of Size Effect and Crack Opening Profiles: Comparison with the Experimental Results

Most engineering materials like concrete contain initial defects. Propagation of these defects under certain loading conditions can result in the failure of the structure. Due to catastrophic failures in the past, the engineering community re-examined the design codes and found that conventional strength based design approaches are not valid in case of sharp cracks as the stress value cannot be used as a failure criterion. Actually, the stress at the tip of a sharp crack in an elastic continuum is infinite no matter how small the applied load [48, 47]. This led to the development of Linear Elastic Fracture Mechanics (LEFM) and the use of fracture mechanics principles in the design and modelling of concrete structures.

In concrete numerical simulations, the application of LEFM is restricted because a crack never propagates alone but it is always accompanied by toughening mechanisms e.g. microcracking, crack branching, crack bridging etc. Alternatively, one might include all these effects by using nonlinear fracture theories like the fictitious crack approach or continuum damage mechanics.

In this chapter, a finite element modelling approach is used to simulate the experimental campaign presented in the previous chapters. More specifically:

- In the first section, some fundamentals of crack propagation based on fracture mechanics principles are presented.
- Continuum damage modelling of concrete is discussed in the second section. Emphasis is made on the nonlocal approach of the continuum.
- The third section presents an elementary simulation of a bar using a nonlocal damage model. The procedures to extract crack openings from nonlocal fields are outlined.

- The fourth section deals with the simulation of the concrete beams presented in Chapters 2 and 3. Focus is made on the determination of the model parameters. Global variables and crack opening profiles are extracted and compared with the experimental data.

4.1 Fundamentals of crack propagation

In this section, attempts are made to review some fundamental aspects of concrete fracture. In fracture mechanics, three fracture modes occur in solids. Mode-I or “tensile opening mode” is the most common case where a tensile loading occurs at the crack tip. The crack tip can, however. undergo two other modes, namely Mode-II (in-plane shear) and Mode-III (out-of-plane shear). These three crack modes are shown systematically in Figure 4.1. Only the tensile opening mode of the crack (Mode-I) is focused on in this chapter.

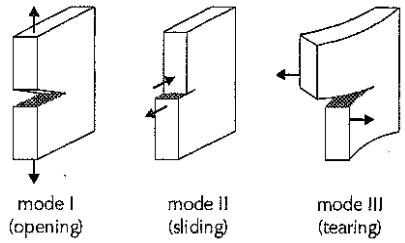

Figure 4.1 Three principle crack modes (a) Mode-I or tensile opening mode (2) Mode-II or in plane shear mode (c) Mode-III or out-of-plane shear mode (from [20]).

4.1.1 Linear elastic crack

Kaplan [63] made a pioneering attempt to apply LEFM principles to concrete. After him, many such attempts have been made to determine global LEFM parameters for concrete, such as the critical stress intensity factor K_{IC} and the critical strain energy release rate G_{IC}. Subsequent work involved determining the relation between fracture parameters and other concrete material characteristics like aggregate size, mechanical strength, rate of loading etc. Soon, it became apparent that a straight forward application of LEFM concepts to concrete is not possible.

Hsu [53] established that the bond between aggregate and matrix is the weakest link in the concrete material. When a load is applied, the bond starts to crack at the early pre-peak stage. The stress-strain diagram starts to deviate from linearity during subsequent loading and energy dissipation occurs due to the formation of microcracks. Unlike brittle materials, a softening type stress-strain curve is obtained. Soon, it was realized that the energy actually required for unit crack propagation is much larger than G_{IC} due to the fact that cracks in quasi-brittle materials are not smooth and are accompanied by toughening mechanisms [63]. For this reason, the G_{IC} is replaced by the crack growth resistance $\Re$. Successive experimental research consisted of setting up test methods to measure $\Re$. One important theoretical step was the discovery of the J-integral by Rice [104] which provided a way to relate the energy release rate for any elastic material to the stress and strain fields close to the crack tip and thus gave a key to analyzing fracture for nonlinear materials.

4.1.2 Critical crack tip opening displacement

Wells [132] proposed that crack tip opening displacement (*CTOD*), defined as the displacement at the tip of the notch (Figure 4.2), can be used to describe fracture toughness of inelastic materials. Jenq and Shah [61] proposed a two-parameter fracture model. They assumed that considering the presence of the crack tip inelastic zone, *CTOD* consists of an elastic component ($CTOD_e$) and an inelastic component ($CTOD_p$). To separate the elastic and plastic fracture responses of a given specimen as shown in Figure 4.2(a), the specimen may be loaded up to the maximum stress, and an unloading and reloading cycle is performed as shown in Figure 4.2(b).

The crack mouth opening displacement (*CMOD*) can be defined as the displacement at the notch mouth. Based on the obtained unloading compliance, the value of the crack mouth opening displacement at peak load ($CMOD_c$) can also be divided into two components.

$$CMOD_c = CMOD_c^e + CMOD_c^p \tag{4.1}$$

Where $CMOD_c^e$ and $CMOD_c^p$ are the elastic and inelastic components respectively and can be determined as shown in Figure 4.3(b). The measured values of $CMOD_c^e$ as well as the maximum stress σ_c are further substituted into the following LEFM equations to calculate the critical stress intensity factor K_{IC} and the critical effective elastic crack length a_c.

$$K_{IC} = \sigma_c \sqrt{\pi a_c}\; g_1\left(\frac{a_c}{b}\right) \tag{4.2}$$

$$CMOD_c^e = \frac{4\sigma_c a_c}{E}\, g_2\left(\frac{a_c}{b}\right) \tag{4.3}$$

The value of critical tip opening displacement $CTOD_c^e$ is then determined based on the obtained values of crack mouth opening displacement at critical stage, $CMOD_c^e$.

$$CTOD_c^e = CMOD_c^e\; g_3\left(\frac{a_c}{b}, \frac{a_0}{a_c}\right) \tag{4.4}$$

Where g_1, g_2 and g_3 are geometric functions [61], b is the height of the specimen and E is the Young's modulus. The schematic diagram of the Jenq and Shah model is presented in Figure 4.3.

Jenq and Shah [61] proposed that the fracture property of a quasi-brittle material may be characterized by the values of K_{IC} and $CTOD_c$. It is important to note that the $CTOD_c$ is defined at the initial crack

tip and that geometric factors such as geometrically similar crack lengths at critical loads are assumed for geometrically similar beams. A large round-robin test program was conducted by RILEM Committee TC89 [65]. It is shown that the critical stress intensity factor K_{IC} evaluated at the tip of the effective crack is essentially independent of the specimen size as well as the methods of the estimation of the effective crack lengths. A similar extensive comparison has not been done for $CTOD_c$. Since $CTOD_c$ is a small quantity and thus difficult to measure, additional verification is needed to confirm that it is indeed a material property.

Karihaloo and Nallathambi [64] proposed an effective crack model based on the equivalent LEFM approach. The basic concept is similar to the two-parameter fracture model [61]. However, secant compliance at the maximum load, rather than the elastic part of the unloading compliance is used to determine the effective-elastic crack length.

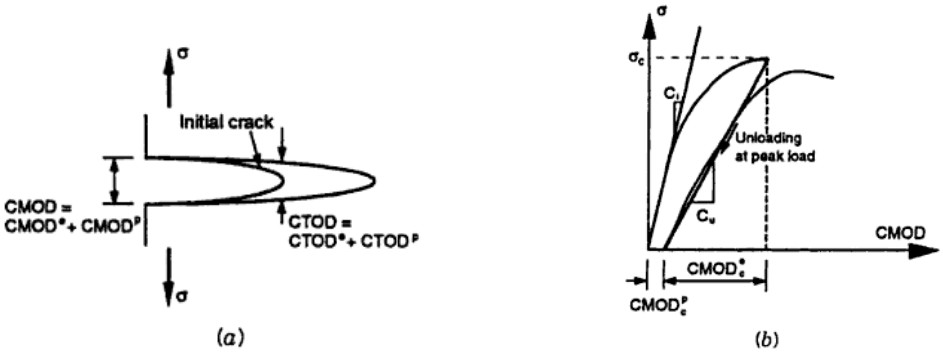

Figure 4.2 Procedure for determining fracture parameters by the two-parameter fracture model [61] (a) crack tip opening displacement (b) loading and unloading procedure.

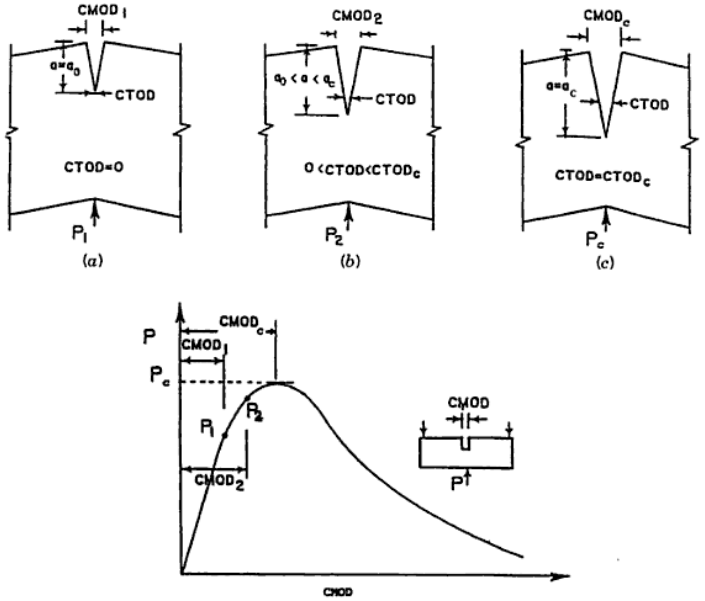

Figure 4.3 Stages of crack growth according to Jenq and Shah model [61] (a) initiation of stable crack growth (b) stable crack growth (c) start of unstable crack growth.

In summary, all the models based on effective elastic crack approach (e.g. Jenq and Shah model [61]) can only predict the maximum load and the corresponding displacement (the crack lengths may not be correct), since material fracture parameters are defined for the critical fracture of a structure. Since the pre-peak stable crack growth can be controlled by critical fracture, it may also be predicted. However, discrepancies increase as the fracture state is far away from the peak load. Generally, effective-elastic crack approach may underestimate the displacement after the peak load because the inelastic response is ignored.

4.1.3 Fracture energy dissipation in a quasi-brittle crack

The fracture behaviour of concrete is greatly influenced by the fracture process zone. Among the most successful approaches to apply fracture mechanics, one is to simulate Mode-I concrete fracture with an effective line crack. In this case, the inelastic fracture process zone is taken into account by cohesive pressure acting on the crack faces. The cohesive pressure $\sigma(w)$ is a monotonic decreasing function of the crack opening displacement w. The value of $\sigma(w)$ is equal to material tensile strength f_t for $w = 0$ at the crack tip (the end of the fracture process zone). This implies that microcracks ahead of the crack tip are not included in the fracture process zone.

This is reasonable if the size of microcracking zone is negligible compared to the macrocrack and thus the energy released due to microcracking can be neglected. The energy release rate G_q at the tip of the effective quasi-brittle crack may therefore be divided into two portions (1) the energy consumed during the material fracturing in creating two surfaces G_{IC}, which is equivalent to the material surface energy, and (2) the energy rate to overcome the cohesive pressure $\sigma(w)$ in separating the surfaces, G_σ. As a result, the total energy release rate for a mode-I quasi-brittle crack can be expressed as:

$$G_q = G_{IC} + G_\sigma \tag{4.5}$$

The value of G_{IC} may be evaluated based on LEFM and is called critical energy release rate. Since G_σ is equal to the work done by the cohesive pressure over a unit length of the crack for a structure with a unit thickness, its value can be calculated as:

$$\begin{aligned} G_q &= \frac{1}{\Delta a}\int_0^{\Delta a}\int_0^{w}\sigma(w)dx\,dw = \frac{1}{\Delta a}\int_0^{\Delta a} dx \int_0^{w}\sigma(w)\,dw \\ &= \int_0^{w_t}\sigma(w)\,dw \end{aligned} \tag{4.6}$$

Substituting we get

$$G_q = G_{IC} + \int_0^{w_t} \sigma(w)\, dw \tag{4.7}$$

Where Δa is the change in crack length, $\sigma(w)$ is the normal cohesive pressure and w_t is the crack separation displacement at the initial crack tip. The above Equation (4.7) is the general energy equilibrium condition for the propagation of a mode-I quasi-brittle crack. It shows that for quasi-brittle fracture, the energy release rate due to applied load (G_q) is balanced by two fracture energy dissipation mechanisms i.e. the energy dissipation due to creation of a new fracture surface [47] and the energy dissipation due to formation of a nonlinear fracture zone (due to toughening mechanisms).

4.1.4 Fictitious crack model

The fictitious crack approach assumes that energy required to create the new surfaces is small compared to that required to separate them. As a result, the energy dissipation can be completely characterized by the cohesive stress-crack opening relationship $\sigma(w)$. Hillerborg and co-workers [51] were the firsts to propose a fictitious crack model for fracture in concrete. The area under the entire softening stress-crack opening curve is denoted as G_f, and it is given by

$$G_f = \int_0^{w_c} \sigma(w)\, dw \tag{4.8}$$

The fracture energy represents the energy absorbed per unit area of the crack and is regarded as a material fracture parameter. In the fictitious crack model, the softening, stress-crack opening curve $\sigma(w)$ is also assumed as material property, independent of the structural geometry and size. Therefore, the fictitious crack model requires knowing only three material parameters: the values of f_t, G_F and the shape of the $\sigma(w)$ curve. Here, the characteristic length of the material is defined as the length of the fracture process zone and determined by

$$l_{ch} = \frac{EG_f}{f_t'^{\,2}} \tag{4.9}$$

Where E is the modulus of elasticity of the material. The value of l_{ch} approximately ranges from 100mm to 400mm [52].

It is noted that the choice of the $\sigma(w)$ function influences significantly the prediction of the structural response [108, 1] and the local behaviour (e.g. the crack opening displacement is particularly sensitive to shape of the $\sigma(w)$ curve). Different shapes of $\sigma(w)$ curves, including linear, exponential and power functions have been previously used. Experimental determination of $\sigma(w)$ using tension tests has also been suggested [46]. However this is difficult as results may vary with the specimen size and shape [127].

4.2 Damage Mechanics and Smeared crack concept

Two approaches can be found in the literature to simulate cracks: the discrete approach and the smeared crack approach. The former approach models crack as a geometrical discontinuity, whereas the latter imagines the cracked solid as a continuum. In a typical finite element analysis cracks are often modelled by means of a separation between finite element edges. The approach suffers from a major drawback that the crack is constrained to follow a predefined path along the element edges. Recently, an extension of the finite element method known as the Extended Finite Element Method (X-FEM) [93] was developed to cater the arbitrary discontinuities in meshes. This extension exploits the partition of unity property of finite elements [84], which allows local enrichment functions to be easily incorporated into a finite element approximation. Work has also been done to model cohesive crack growth, where energetic considerations are used to model the crack tip [92].

The counterpart of the discrete crack concept is the smeared crack concept, in which the cracked solid is imagined to be a continuum. This approach, introduced by Rashid [103], starts from the notion of stress and strain and permits a description in terms of stress-strain relations. Many numerical models are proposed based on continuum damage modelling approach [113, 73]. The procedure is attractive not only because it preserves the topology of the original finite element mesh, but also because it does not impose restrictions with respect to the orientation of the crack planes. It is for these two reasons that the smeared crack concept has quickly replaced the early discrete concepts and has become into widespread use after the 1970s. Different models based on the smeared crack concept and the damage mechanics theory are detailed hereafter.

4.2.1 Crack band Model

Bazant and Oh [11] modelled the fracture process zone considering a band of uniformly and continuously distributed microcracks, which has a fixed width h and a blunt front as shown in Figure 4.4. Crack propagation is simulated by a simple stress-strain relationship. Bazant argued that for randomly inhomogeneous materials, the equivalent continuum stresses and strain are defined as the

averages of microstresses and microstrains over a certain representative volume. The cross section of this volume should be ideally taken to be much larger than the size of the inhomogeneities i.e. several times the maximum aggregate size in the case of concrete. From different measurements, Bazant further assumed that large amount of microcracks are concentrated essentially on a line which is highly tortuous, extending to each side of the straight line to a distance equals to the aggregate size, as the crack is trying to pass around the harder aggregate pieces. Also, Bazant assumed that the boundary of the fracture process zone should not be defined as the boundary of visible microcracks, but as the boundary of the strain- softening region. Since the strain softening is caused not only by microcracking but also by any bond ruptures, the fracture process zone could be much wider (as well as longer) than the region of visible microcracks. To build an equivalence principle between the crack band model and the cohesive crack model, the crack opening displacement is considered as:

$$h\varepsilon^{f} = w \tag{4.10}$$

Where ε^{f} is the inelastic fracturing strain, graphically defined as shown in Figure 4.4 and w is the cohesive crack opening displacement.

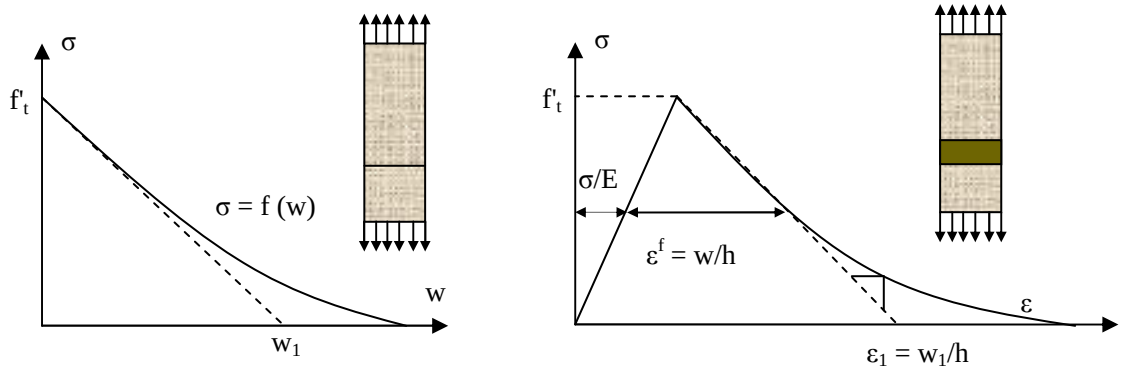

(a) (b)

Figure 4.4 Correspondence between (a) the softening curve of the cohesive crack model and (b) the stress-strain curve of the crack band model [11].

Based on Equation 4.10, the energy consumed due to crack advance per unit area of the crack band is the product of the area under the stress-strain curve and the width of the crack band h. This leads to

$$G_f = h_c\left(1+\frac{E}{E_t}\right)\frac{f_t^{'2}}{2E} \tag{4.11}$$

Where E_t is the strain-softening modulus (represented by the dashed line in Figure 4.4) and $f_t^{'}$ is tensile strength of the material. The width of the crack band is calculated as $h = n_a d_a$, d_a being the maximum aggregate size and n_a is an empirical constant whose suggested value is 3 for concrete. It implies that the size of the facture process zone is independent of the size and geometry of the specimen (this assumption is criticized in [38]).

For the models based on the fictitious crack approach [51, 11] it is often reported that the assumption $G_{IC} = 0$ provides some computational efficiency. However, specific features associated with crack propagation, such as crack profiles, computed from the fictitious crack approach often do not match with those experimentally measured [89]. The fictitious crack model may physically make sense when the crack tip fracture process zone has the same fracture mechanisms as the crack wake-process-zone or macrocrack propagation [31]. Another problem with fictitious crack models is the need to determine experimentally a size independent value of the tensile strength that can be measured consistently and easily [114].

4.2.2 Continuum damage modelling of concrete

In the continuum damage mechanics theory the mechanical effects of toughening mechanisms, void nucleation and growth are represented by a set of state variables which act on the elastic and/or inelastic behaviour of the material at the macroscopic level.

4.2.2.1 Mazars damage model

Hereafter, a simple scalar damage model is presented, in which damage is assumed to be isotropic [82]. In damage mechanics theory, damage engenders a degradation of the elastic stiffness of the material through a variation of the Young's modulus.

$$\varepsilon_{ij} = \frac{1+\nu_0}{E(1-d)}\sigma_{ij} - \frac{\nu_0}{E(1-d)}\sigma_{kk}\delta_{ij} \tag{4.12}$$

Where ν_0 and E_0 are the Poison's ratio and Young's modulus of the undamaged isotropic material respectively and δ_{ij} the Kronecker symbol. The elastic (i.e. free) energy per unit mass of the material is:

$$\rho\psi = \frac{1}{2}(1-d)\varepsilon_{ij}C^0_{ijkl}\varepsilon_{kl} \tag{4.13}$$

Where d is the damage variable. Its value varies from 0 to 1 for the undamaged to fully damaged state respectively. C_0 is the stiffness tensor of the undamaged material. This energy is assumed to be the state potential. The damage energy release rate is defined as the variable associated to the damage state variable in the state potential:

$$Y = -\rho \frac{\partial \psi}{\partial d} = \frac{1}{2} \varepsilon_{ij} C_{ijkl} \varepsilon_{kl} \leq Y_0 \tag{4.14}$$

With the rate of dissipated energy:

$$\dot{\phi} = -\frac{\partial \rho \psi}{\partial d} \dot{d} \tag{4.15}$$

Where ρ is the mass density.
For an isotropic damage model, this equation reduces to:

$$\dot{\phi} = Y\dot{d} \tag{4.16}$$

The damage energy release rate is always positive and thus the rate of damage must be positive in order to comply with the second principle of thermodynamics. The evolution of damage is very often related to the strain state. Moreover, it is defined in an explicit, integrated way, which is easier to handle. The damage loading function can be defined as:

$$f\left(\tilde{\varepsilon}, Y\right) = \tilde{\varepsilon} - \kappa \tag{4.17}$$

Where $\tilde{\varepsilon}$ is a positive equivalent measure of strain and κ equals the damage threshold κ_{D0} initially and during the damage process it is the largest ever reached value of $\tilde{\varepsilon}$. For the uni-axial tensile case, the equivalent uni-axial strain is straightforward (it is the axial strain). However, for general states of stress, damage evolution should be related to some scalar quantity, function of the state of strain. There are several proposals in this regard. For concrete, Mazars [82] proposed the following form:

$$\tilde{\varepsilon} = \sqrt{\sum_{i=1}^{3} \left(\langle \varepsilon_i \rangle_+ \right)^2} \tag{4.18}$$

Where ε_i are the principal strains.

The evolution of damage has the following form:

$$\begin{aligned} &If \qquad f(\tilde{\varepsilon},\kappa)=0 \;\; and \;\; \dot{f}(\tilde{\varepsilon},\kappa)=0 \; then \begin{cases} d=h(\kappa) \\ \kappa=\tilde{\varepsilon} \end{cases} \;\; where \;\; \dot{d}\geq 0 \\ &otherwise \begin{cases} \dot{d}=0 \\ \dot{\kappa}=0 \end{cases} \end{aligned} \tag{4.19}$$

The function $h(\kappa)$ is specific, depending on different models in the literature.

In order to capture the differences of mechanical responses of the material in tension and in compression, the damage variable is often determined as a linear combination of two damage variables d_t and d_c, (see [82]):

$$d=\alpha_t d_t+(1-\alpha_t)d_c \tag{4.20}$$

Where d_t and d_c are the damage variables in tension and compression respectively. They are combined with the weight coefficients α_t defined as functions of the principal values of the strains ε_{ij}^t and ε_{ij}^c, due to positive and negative stresses.

$$\sigma_{ij}^t=(1-d)C_{ijkl}^{-1}\varepsilon_{kl}^t \;, \quad \sigma_{ij}^c=(1-d)C_{ijkl}^{-1}\varepsilon_{kl}^c \tag{4.21}$$

$$\alpha_{t,c}=\sum_{i=1}^{3}\left(\frac{\langle\varepsilon_i^{t,c}\rangle\langle\varepsilon_i\rangle_+}{\tilde{\varepsilon}^2}\right)^{\beta} \tag{4.22}$$

In uni-axial tension α_t = 1 and in uni-axial compression α_t = 0. Hence, d_t and d_c can be obtained separately from uni-axial tests. The purpose of exponent β is to reduce the effect of damage on the response of the material under shear compared to tension [100]. The evolution of damage is provided in an integrated form, as a function of the variable κ [82]:

$$d_{t,c}=1-\frac{\kappa_{D0}(1-A_{t,c})}{\kappa}-A_{t,c}\exp\left(-B_{t,c}(\kappa-\kappa_{D0})\right) \tag{4.23}$$

Where κ_{D0}, A_t, B_t, A_c and B_c are model parameters.

4.2.2.2 Influence of model parameters

Besides the elastic parameters E, υ, there are six parameters to be defined in Mazars damage model (A_t, A_c, B_t, B_c, κ_{D0}, β), see Figure 4.5.

- κ_{D0} is the damage threshold. Its value influences the stress at peak as well as the curve of post peak. The stress drop will be less brittle if the value of κ_{D0} is small. The recommended values of κ_{D0} are from 0.5 to 1.5 x 10^{-4}.
- The A coefficient influences the tail part of post-peak stress-strain curve. This coefficient gives the horizontal asymptote of ε axis when A equals to 1 and a horizontal line passing from the peak if A is taken as 0.
- The B coefficient influences the post-peak curve as it induces a stress drop if its value is too high (B > 10000). Typical values are: B_c between 1000 and 2000, and B_t between 5000 and 100000.
- β is a corrective factor which makes it possible to improve the result in shearing compared to the initial version of the model (which corresponds to β =1). The typical value used is 1.06.

a)

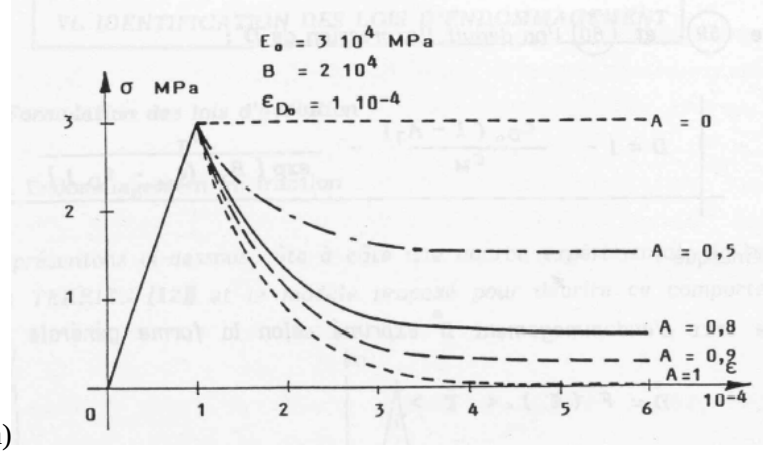

b)

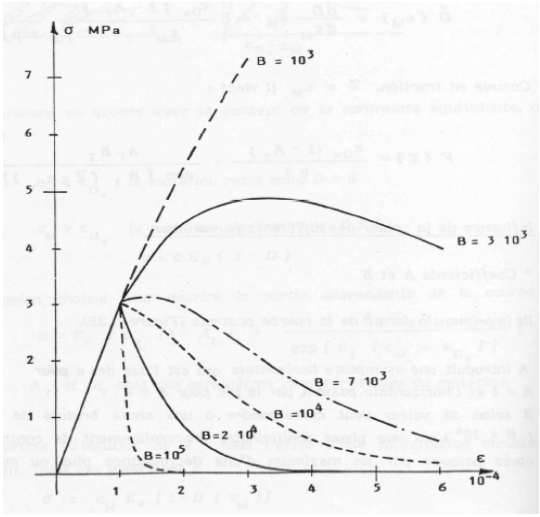

Figure 4.5 Mazars model: Influence of the parameters (a) A_t (b) B_t [82].

4.2.2.3 Nonlocal continuum damage

The forgoing damage formulation of damage theory is local. It is however clear that after microcracking has taken place in concrete; a macroscopic mechanism develops in the form of a damage band. The strains tend to localize in a specific area of finite dimension (macrocrack). The local model formulation predicts this dimension to be zero, with vanishing energy dissipation at failure. Numerically, it yields a response which is dependent on the size and the orientation of the mesh. Therefore, a regularization technique has to be added in order to achieve a mesh independent result and damage localization over several finite elements.

It is often argued that the stress response of a material point cannot be described locally but one has also to consider its neighbourhood in order to take into account microcracks interaction [98]. Non locality, in a gradient or integral format, is a mean for a proper, consistent modelling of fracture [3, 33, 98]. It avoids the difficulties encountered upon material softening and strain localization. Within a single approach, it encompasses both crack initiation (for which continuum models are very well fitted) and crack propagation (for which discrete fracture approaches have been developed).

In the scalar damage model proposed by Mazars [82], in which evolution of damage is controlled by the equivalent strain $\tilde{\varepsilon}$, the principle of nonlocal continuum models is to replace the equivalent strain $\tilde{\varepsilon}$ with its weighted average [98]:

$$\bar{\varepsilon}(x) = \frac{1}{\Omega_r(x)} \int_{\Omega} \psi(x,\xi)\tilde{\varepsilon}(\xi)d\xi \tag{4.24}$$

Where Ω is the volume of the structure and $\psi(x, \xi)$ is the weight function. It is required that the nonlocal operator does not alter the uniform field, which means that the weight function must satisfy the condition:

$$\int_{\Omega} \psi(x,\xi)d\xi = 1 \qquad \forall x \in \Omega \tag{4.25}$$

For this reason, the weight function is recast in the following form [98]:

$$\psi(x,\xi) = \frac{\psi_0(x-\xi)}{\Omega_r(x)} \quad , \quad \Omega_r(x) = \int_{\Omega} \psi(x-\xi)\, d\xi \tag{4.26}$$

Where $\Omega_r(x)$ is a representative volume at point x and $\psi_0(x\text{-}\xi)$ is the basic nonlocal weight function of the distance $(x\text{-}\xi)$ between the point at which the average is taken and the point contributing to that average. A Gauss distribution function if often considered to define $\psi_0(x\text{-}\xi)$:

$$\psi_0(x-\xi) = \exp\left(-\frac{4\left\|x-\xi\right\|^2}{l_c^2}\right) \tag{4.27}$$

l_c is the internal length of the nonlocal continuum. $\bar{\varepsilon}$ replaces the equivalent strain in the evolution of damage. In particular, the loading function becomes $f(\bar{\varepsilon}, Y) = \bar{\varepsilon} - \kappa$.

The representative volume in one, two or three dimensions may be taken as a line segment of length l_c, or a circle or sphere of diameter l_c. Due to this spatial averaging, a special treatment is required for points located at the boundary or close to it where a part of the material representative volume Ω_r protrudes outside the boundary. For such points, Ω_r is considered as a variable.

Different variations of the original formulation can be found in the literature. The advancements are twofold: (1) preserving the uniform field in the vicinity of the boundary makes the averaging in Equation (4.26) not symmetric to its arguments x and ξ. This lack of symmetry leads to the non symmetry of the tangent operator [97, 62]. A symmetrical nonlocal formulation has been recently proposed [19, 68]. (2) The model should be able to capture the discontinuous fields involved in the process of failure due to increasing stress. For this reason focus is made on the case of evolving boundaries of the nonlocal fields. Different modifications of the integral type nonlocal damage have been introduced, in which the internal length l_c increases [99] or decreases [45] in the course of damage, based on experimental observations.

In the following sections the original nonlocal formulation of the Mazars damage model is used [13, 98]. In the following sections, this model is adopted in order to investigate the numerical response of a 1D model bar and to simulate the experimental campaign on concrete size effect presented in the previous chapters.

4.3 1D bar: Numerical investigations

4.3.1 Mesh discretization

A simple bar of length (L) 1*m* and height (d) 0.1*m* is considered hereafter. The bar is simply supported on the left hand side as shown in Figure 4.6. An incremental uni-axial displacement (δ) is imposed in $x - x$ direction on the right hand side of the bar. Plane stress condition is assumed. The calculation is performed using the finite element code Cast3M.

The mesh is constructed using quadrilateral elements with four gauss points. In order to analyze the mesh objectivity, four different discretizations are adopted (m = 11, 22, 33 and 66) where m = number of elements in the bar and *h* is the size of the element.

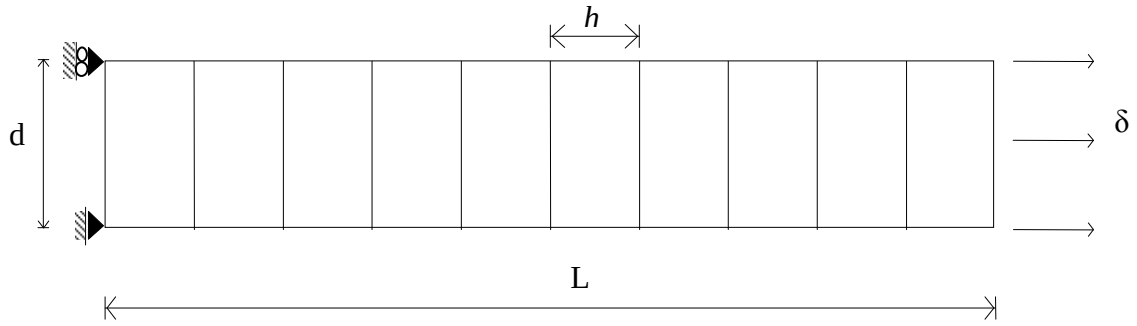

Figure 4.6 Finite element mesh of the 1D bar.

4.3.2 Material parameters

Mazars damage model is used in this study and the material parameters are given in Table 4.1. The Poison coefficient is taken equal to 0 to obtain 1D behaviour. A spatial variability of damage threshold κ_{D0} is generated by using a Gaussian distribution function as shown in Figure 4.7. This distribution causes the variation of material tensile strength f_t of the same magnitude, where f_t is calculated as:

$$f_t = E \text{ x } \kappa_{D0} \tag{4.28}$$

Where E is the Young's Modulus and κ_{D0} is damage threshold and its value is varied between κ_{D0}^{I} and κ_{D0}^{II}.

Table 4.1 Material parameters.

E_0 (MPa)	ν_0	κ_{D0}^{I}	κ_{D0}^{II}	A_t	B_t	A_c	B_c	β
30 000	0	1.3×10^{-4}	7.0×10^{-5}	1	3000	1.2	1500	1.06

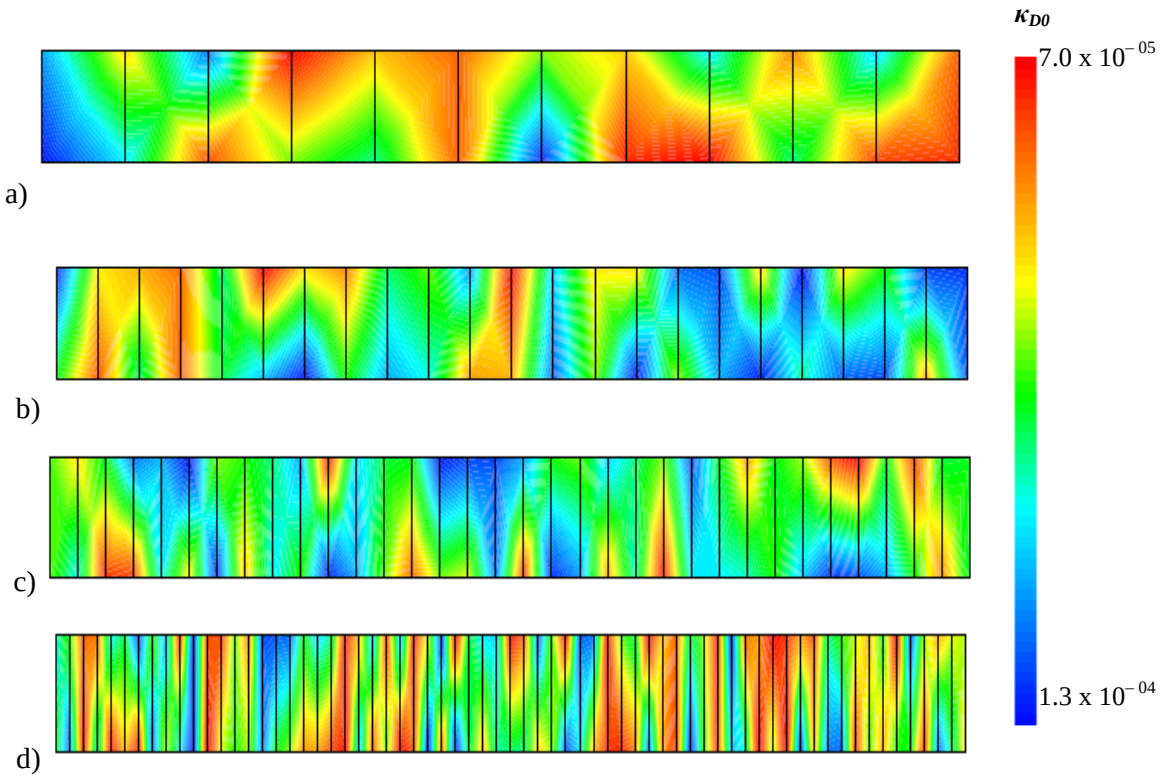

Figure 4.7 Distribution of damage threshold in different discretizations of the model beam (a) m = 11, (b) m = 21, (c) m = 31, (d) m = 61.

From Figure 4.7 it can be seen that the gauss distribution function in Cast3M provides a distribution of the damage threshold κ_{D0} both in the X and Y directions.

4.3.3 Local calculation

The first calculation is performed using the local formulation of the Mazars damage constitutive law (Section 4.2.2.1). The global Force-Displacement curves obtained for the different meshes are shown in Figure 4.8. In each case, the peak load is the same; however the post-peak behaviour is different as the mesh is refined. The snap back behaviour becomes more important as the size of finite element is reduced. This is the consequence of the strain or damage localization as shown in Figure 4.9. Solution depends on the finite element size. By further decrease of the size of the element damage will localize into a zone of vanishing volume. In this volume the total energy dissipation rate (Equation 4.15) will tend to zero which is physically unrealistic [98].

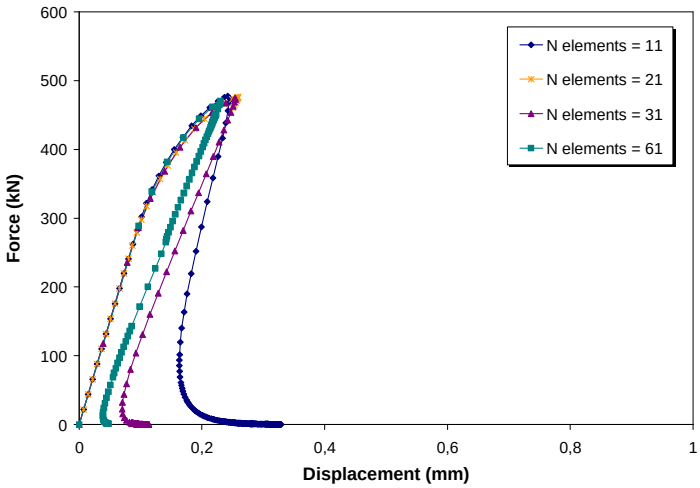

Figure 4.8 Force – Displacement curves for different meshes (local formulation).

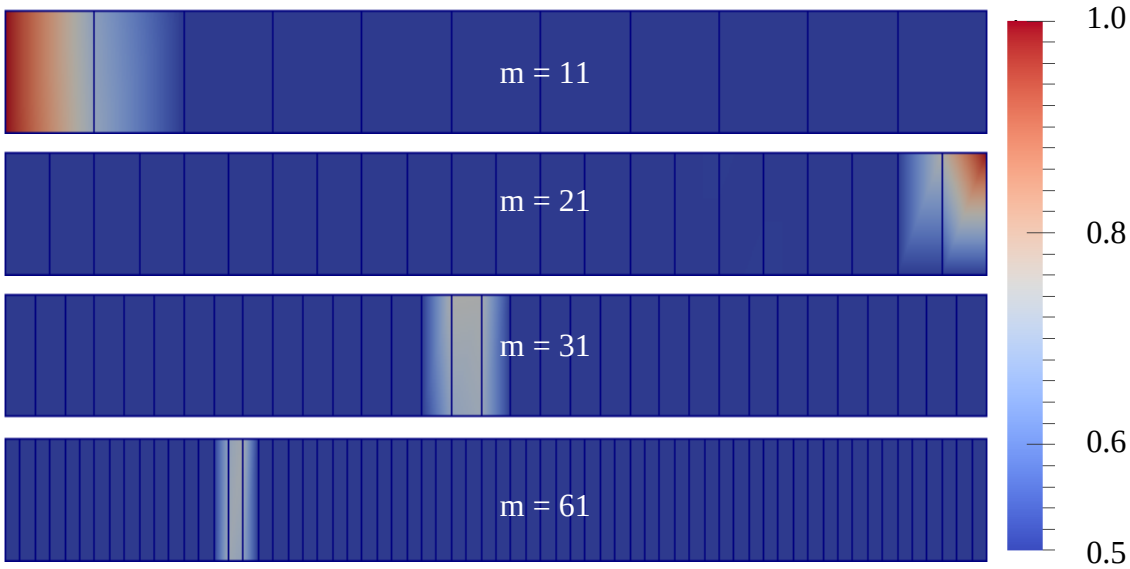

Figure 4.9 Damage field at final loading stage for different meshes (local formulation).

4.3.4 Nonlocal calculation

The nonlocal formulation of the Mazars damage model (Section 4.2.2.3) is used hereafter with a localization limiter or internal length l_c equal to 0.3. This value is selected in order to have at least three times the size of the finite element. Figure 4.10 shows the global Force-Displacement curves for each mesh. Almost the same global response is observed, independent of the mesh sizes. The small differences are due to the differences on the spatial variability of the damage threshold.

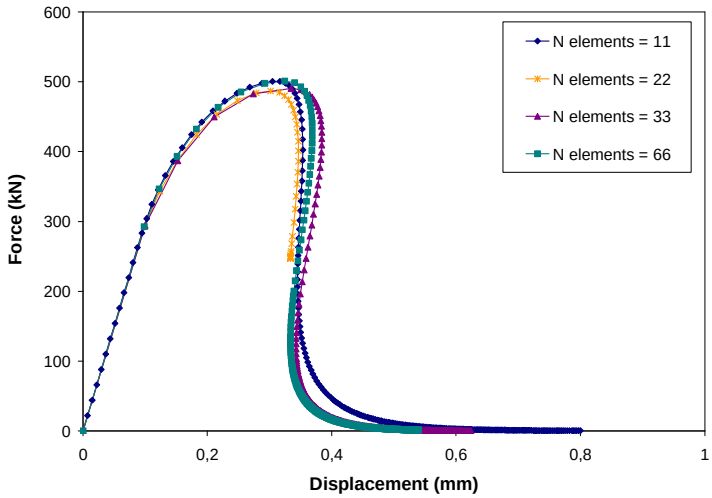

Figure 4.10 Force – Displacement curves for different meshes (nonlocal formulation).

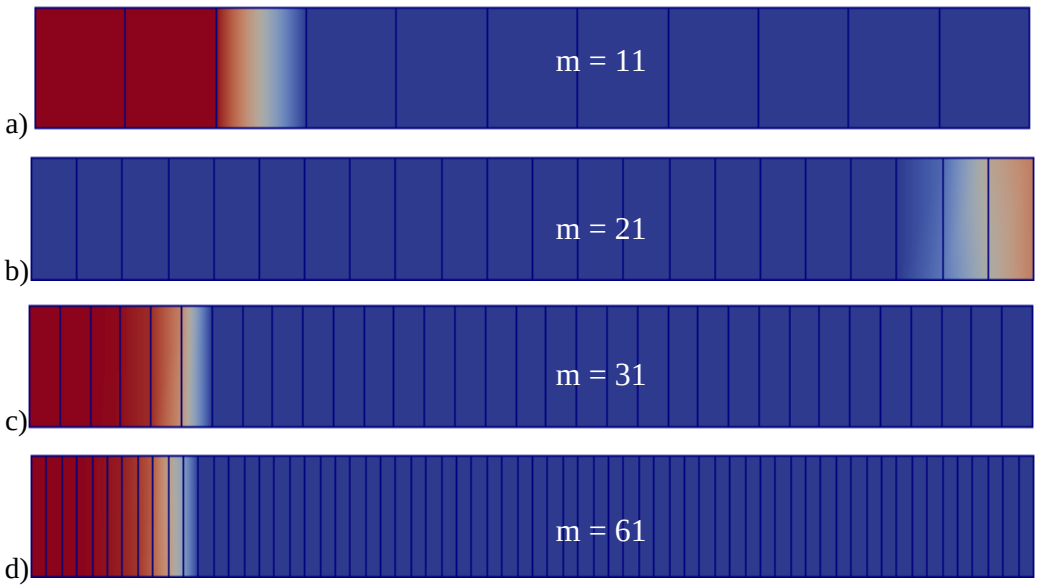

Figure 4.11 Damage field at final loading stage for different meshes (nonlocal formulation).

The damage field at the final loading stage and for the different meshes is presented in Figure 4.11. Damage is localized in the zone which is several times the element size. The location of the damage zone is different for the mesh m=21 due to the random distribution of the damage threshold.

In order to examine the evolution of damage for different finite element sizes, the damage fields at different loading stages and for two types of mesh refinements (m = 11 and 66) are presented in Figures 4.12 and 4.13 respectively. In both cases, a similar behaviour is observed. In the elastic range, damage is equal to zero in the beam. In the non-linear range up to the peak load, damage increases in

the same way. The small fluctuations are due to the random distribution of the damage threshold. However, the damage starts to localize as soon as the peak-load is attained. In the post-peak regime, the damage increases in the localized zone of length equal to the internal length l_c (0,3m).

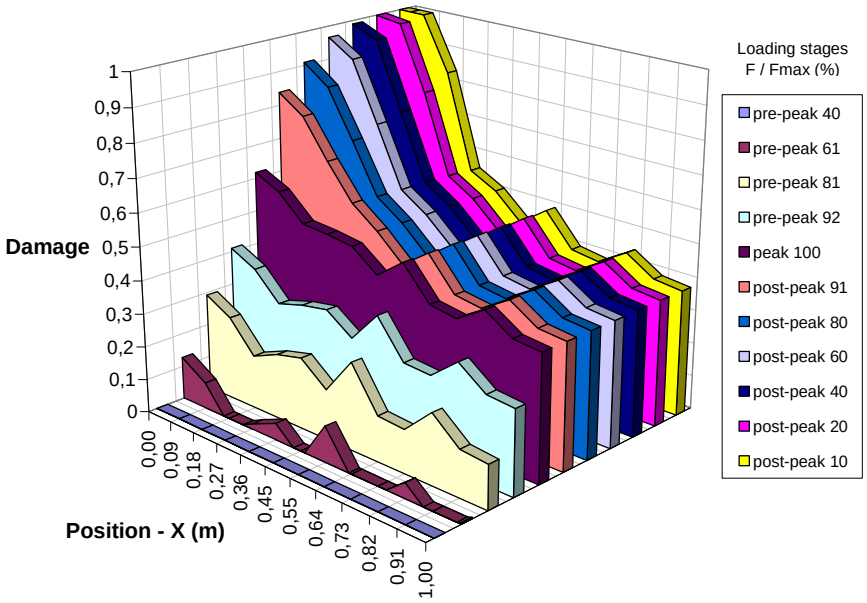

Figure 4.12 Damage evolution diagram (m = 11, nonlocal formulation).

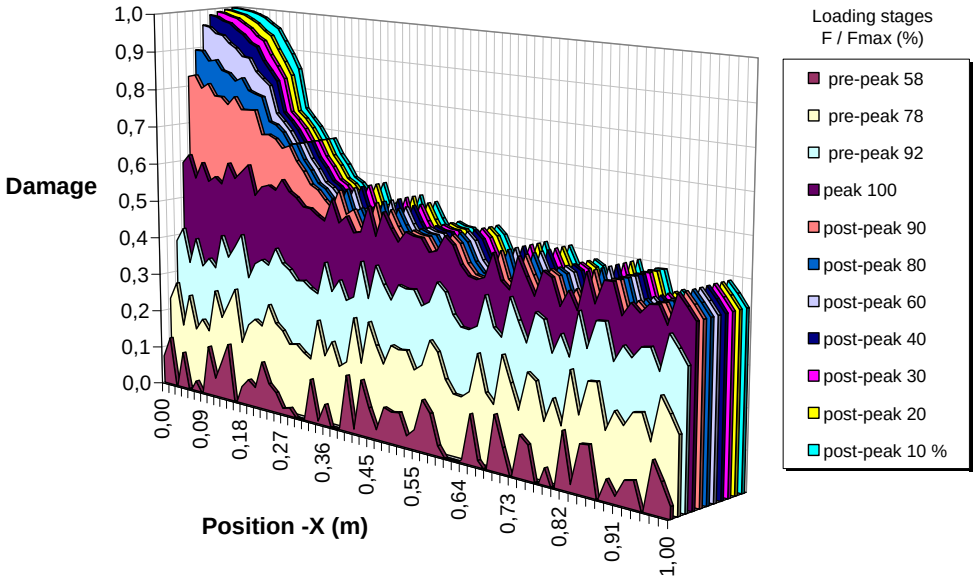

Figure 4.13 Damage evolution diagram (m = 61, nonlocal formulation).

4.3.5 Calculation of crack opening

In [83] it is shown that damage and fracture mechanics are two correlated theories. In the later theory, fracture is considered as the development of a macrocrack and the fracture process zone is generally introduced as a cohesive pressure near the crack tip. This approach is equivalent to the continuum

damage mechanics approach and the information of one theory can be obtained from other theory on the basis of an equivalence principle in terms of energy release. For example one can try to use crack openings, which however are not directly available when using continuum damage models. In general, a post-processing method is needed to extract crack openings from continuous fields. Different post-processing approaches have already been proposed in the framework of the French national project CEOS.fr [80]. Two of them are studied hereafter.

The first method (displacement jump technique) is based on the assumption of the crack band theory that the energy dissipation in the localized damage zone is equal to the energy consumed by a line crack with certain crack opening [11]. In local models, damage is localized in one element. In nonlocal models however, damage is localized in a zone of width equal to the internal length l_c (see Figures 4.12 and 4.13). Crack opening can therefore be estimated as the displacement jump across the localized damage zone of width equal to the internal length. Figure 4.14 presents the evolution of axial displacement in the beam (m=66). Since the beam fails at the left edge, crack openings can be calculated as the difference of the displacement values at the left and right boundaries of the localized damage zone. In this example ($l_c = 0.3m$) the displacement jump between x = 0 and x = $0.3m$ gives the crack opening at x = 0. At peak load the crack opening calculated is $120\mu m$.

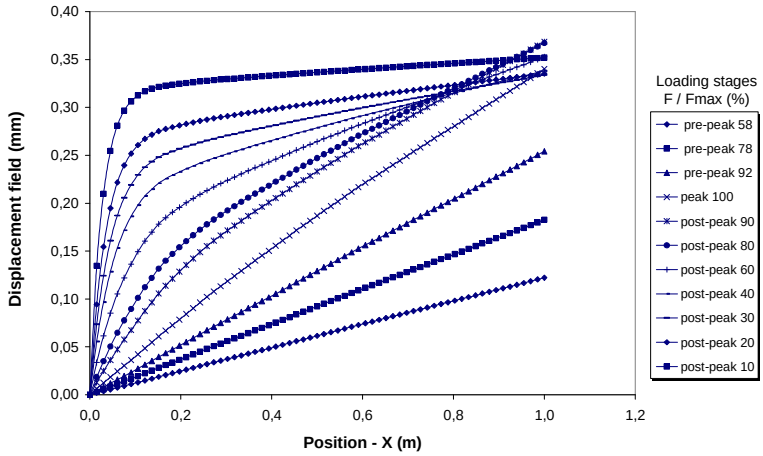

Figure 4.14 Axial displacement profile (m = 66, nonlocal formulation).

The second method used for estimated crack openings from continuum damage fields is proposed by Matallah and co-workers [81]. This method was basically developed for the case of local damage models with fracture energy regularization. The crack opening displacement w is taken as the fracture strain accumulated over the width h of the fracturing element.

$$w = \varepsilon^{uco} h \tag{4.29}$$

Where ε^{uco} is the unitary crack opening strain variable representing the fracture portion of the total strain.

This approach works satisfactorily for local damage models, where *h* is size of the element containing the damage. For these models, fracture energy regularization is an easy task because the model parameters are local. In case of nonlocal models however, strains depend on the neighbouring strains and damage is diffused in several elements. Thus, the application of the above approach (Equation 4.29) can underestimate crack openings. This is clearly shown in Figure 4.15 where the two above methods are compared (m = 61).

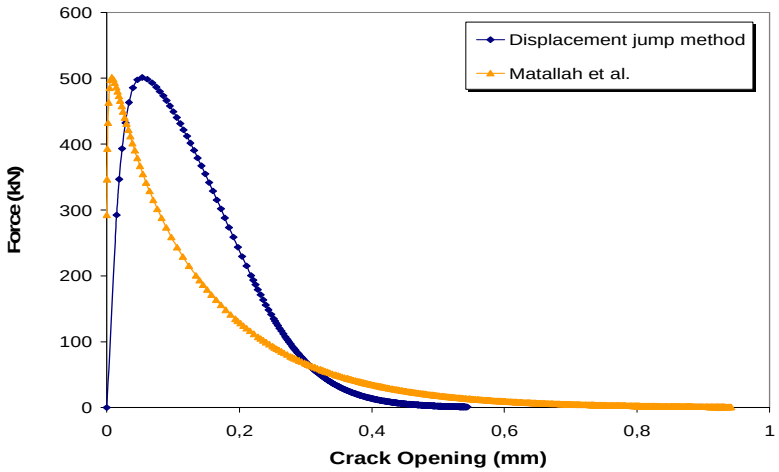

Figure 4.15 Comparison of crack opening using two different methods (nonlocal formulation, m =66).

4.4 Three point bending test

In this section the beams D1, D2 and D3 made from the M1 concrete (see Chapter 3) are modelled using the nonlocal formulation of the Mazars continuum damage mechanics model [82, 98]. The finite element code is Cast3M and plane stress condition is assumed.

4.4.1 Mesh discretization

Two dimensional quadrilateral elements with four gauss points are adopted. The mesh is constructed with elements of different sizes. The elements are kept small in the area close the notch where damage is expected to occur. The lower limit of the element size verifies the usual criterion that the characteristic length l_c should be at least three times the size of the element. However for the three sizes of beams (D1 small, D2 medium, D3 large) the size of elements is kept constant, which is a necessary to model the size effect. The resulting meshes of D1, D2 and D3 beams are presented in

Figure 4.16 (a, b, c). The notch tip of the beam is modelled using an arc as shown in Figure 4.16(d) to avoid any singularity of the mechanical fields.

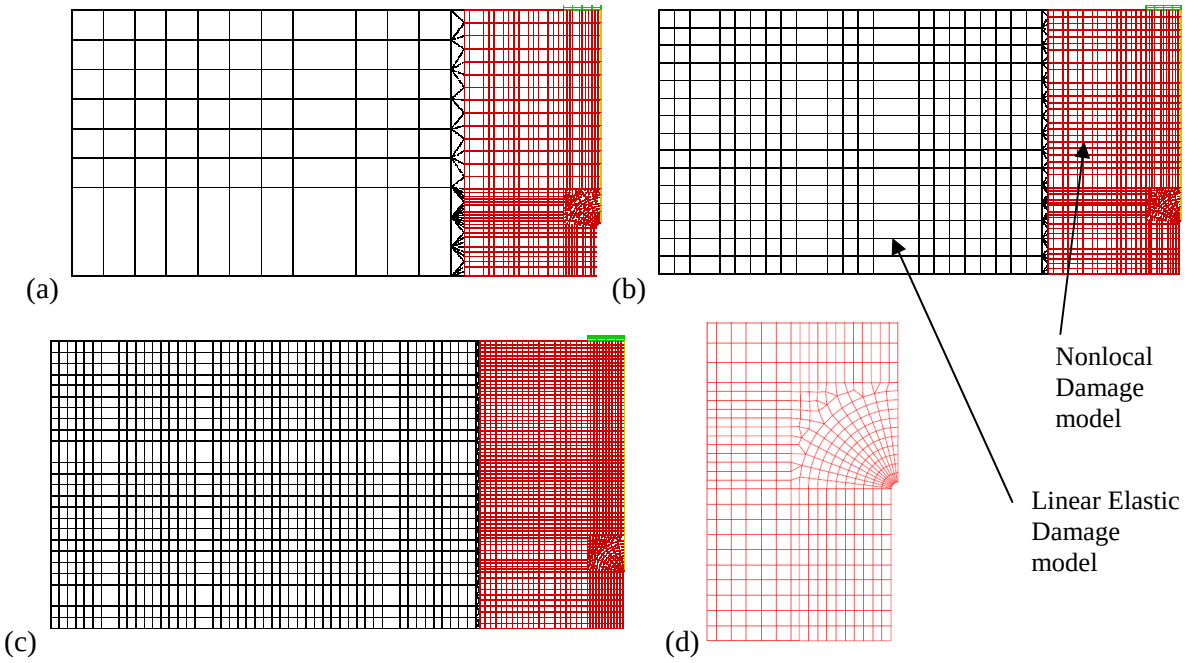

Figure 4.16 Finite element meshes for the (a) D1 beam (b) D2 beam (c) D3 beam (d) notch.

4.4.2 Boundary conditions

Due to symmetrical boundary conditions and in order to reduce the computational demands, only one symmetrical half of the beam is modelled. The nonlocal damage formulation of the model is applied in the central part of the beam where damage is expected to occur (represented in red in Figure 4.16); the other part is assumed linear elastic. This also helps reducing considerably the time of simulation with negligible effects on the results. The part of the beam which is modelled with the nonlocal damage law is always proportional to the height of the beam.

Loading is applied as an incremental vertical displacement of a rigid plate (linear elastic law, with a Young's modulus ten times than that of concrete) fixed at the top right end of the beam (see Figure 4.17). To capture the symmetrical boundary conditions, the displacements in the horizontal direction (X-displacement) of the right side of the beam above the notch are blocked. The vertical displacement of the articulation at the left side of the beam is also restrained.

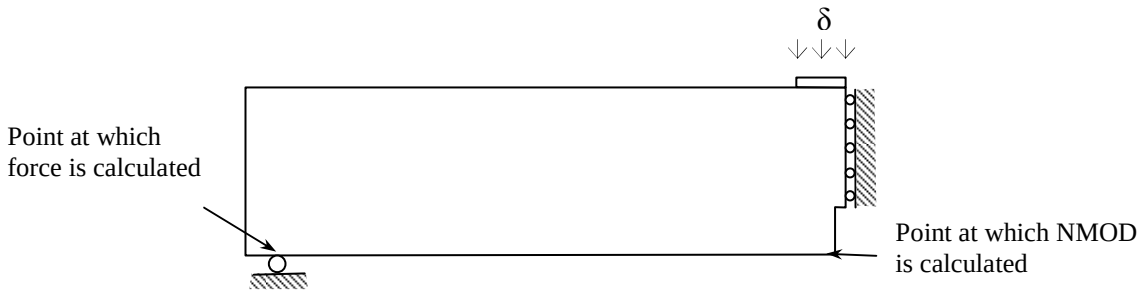

Figure 4.17 Illustration of the boundary conditions.

In the following, global results are presented in the form of Force-Notch Mouth Opening Displacement (NMOD). The force is calculated as the vertical reaction at the bottom left support of the beam and NMOD as the horizontal displacement at the bottom right corner (see Figure 4.17).

4.4.3 Determination of the nonlocal damage model parameters

Two sets of parameters need to be identified for the nonlocal formulation of the Mazars law (1) the local parameters which are related to the local behaviour of the model and (2) the spatial parameter governing the interaction of the material points, which is also termed the *internal length* of the nonlocal continuum and is related to the imaginary width of the fracture process zone. These two sets of parameters are closely related to each other and should be appropriately determined to give the nonlocal model a response consistent with the required macroscopic material behaviour and the local fracture characteristics. The existence of the spatial parameter requires the solution of a boundary value problem for the determination of the model parameters [18]. This is totally different from the local approach, where the (point-wise) constitutive behaviour of the model can be calibrated directly from the experimental data.

This issue has been discussed by several researchers. Their studies can be generally grouped into two classes: those based directly on the numerical inverse analysis of experimental results and those exploiting the correspondence between the cohesive crack model and crack band model. In the first category, an automatic calibration of model parameters based on numerical inverse analysis is generally employed by using optimization algorithms, experimental data from real structural tests and size effect laws. Several different optimization algorithms are available in literature [22, 77, 18]. In the second category, the correspondence between the cohesive crack model and crack band model along with a relationship between the internal length parameter of the nonlocal model and the width *h* of the fracture process zone is exploited (e.g. in nonlocal and gradient models used by De Borst and Pamin [32] and Di Prisco et al. [34]).

In the following, an optimization algorithm is applied based on inverse analysis of the performed size effect tests. The general procedure is the one proposed by Le Bellego and co-workers [18].

The model parameters are assembled in the following vector:

$$x^T = [\ E\ \ \upsilon\ \ \kappa_{D0}\ \ A_t\ \ B_t\ \ A_c\ \ B_c\ \ \beta\ \ l_c\ ] \tag{4.30}$$

Hence, the described model contains eight parameters to be identified.

- The two first parameters are the elastic moduli (Young's modulus E and Poison's ratio υ). They are determined from standard uni-axial tests.
- κ_{D0} is the damage threshold, A_t and B_t are the parameters of the model relative to the damage evolution under tensile loadings (Equation 4.23). They all are unknown.
- A_c and B_c are the parameters of the model relative to the damage evolution law under compressive loadings; β is linked to the shear response. For the case of three point bending tests of concrete beams, tensile loadings are more important than compressive loadings and shear. In the following, A_c, B_c and β are therefore defined using typical values. They are taken equal to 1.2, 1500 and 1.06 respectively.
- The internal length l_c characterises the material connectivity and the fracture process zone and needs to be determined.

The vector of unknown material parameters becomes

$$P^T = [\ \kappa_{D0}\ \ A_t\ \ B_t\ \ l_c\ ] \tag{4.31}$$

For computational efficiency, an initial set of model parameters is first determined by manual calibration on the Force – NMOD curves. A trial and error procedure is adopted by fitting the numerical Force-NMOD curve with the experimental curve. The medium D2 beam is chosen for the initial fitting of the numerical and experimental curves.

Le Bellego and co-workers [18] proposed that the initial value of l_c should be related to the size of the fracture process zone and can be taken between $3d_a$ to $5d_a$, where d_a is the maximum size of aggregates. In this study, two different values of l_c are tested and two initial sets of parameters are obtained as shown in Table 4.2. In the first set, an internal length equal to d_a and in the second (almost) $3d_a$ are chosen. The Force-NMOD curves from both parameter sets are presented in Figure 4.18.

Table 4.2 Initial guess of the nonlocal model parameters (manual calibration).

	κ_{D0}	A_t	B_t	l_c (mm)
Initial Set – 1	5.0 x 10^{-5}	0.75	6500	20
Initial Set – 2	5.6 x 10^{-5}	0.83	21000	65

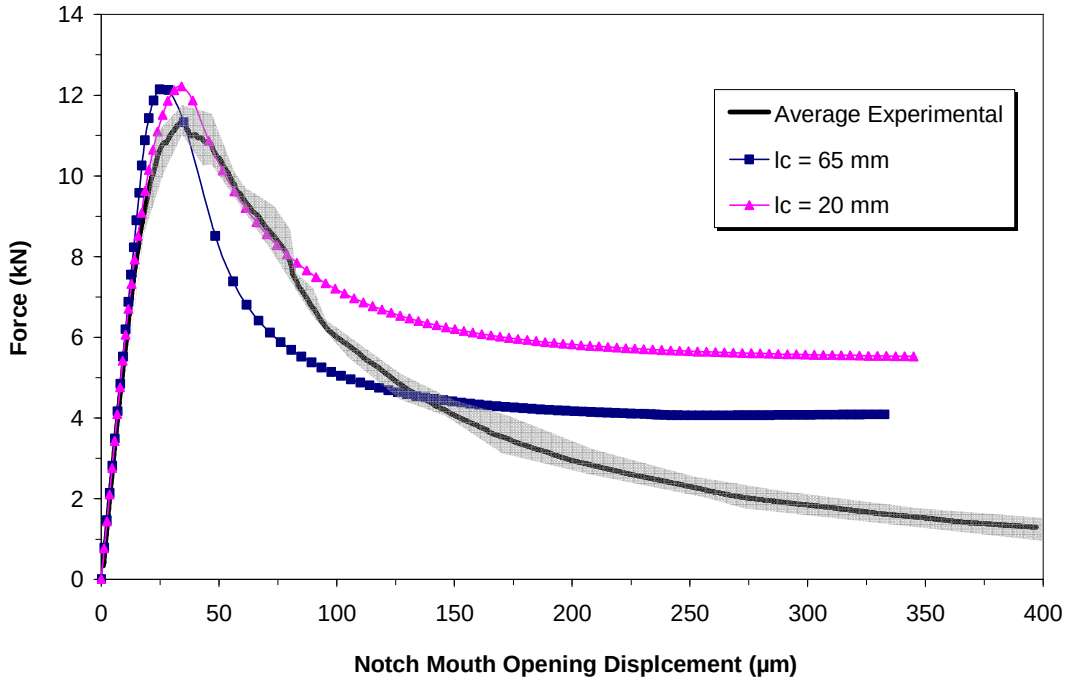

Figure 4.18 Force – Notch Mouth Opening Displacement curve for the D2 beam (initial guess, manual calibration).

Although the manual calibration provides acceptable global results for the D2 specimen (especially till the peak load point), local phenomena may not be correctly reproduced. Furthermore, application to specimens of different sizes will not be accurate because the size effect in not captured [18].

In the second step, the initial sets of parameters (Table 4.2) are adjusted according to the response of geometrically similar beams with varying sizes. This is done using an optimization procedure that calibrates the Force-NMOD responses of the three specimen sizes (D1, D2 and D3) simultaneously. The optimization procedure proposed by Le Bellego et al. [18] proposes the use of the Levenberg-Marquardt algorithm to perform minimization of the following functional $\tau(\vec{P})$:

$$\tau(\vec{P}) = \frac{1}{2}\sum_{size=1}^{3}\left[\sum_{measured\ data\ points}\left\{\left(\frac{R^i(\vec{P}) - R^i_{\exp}}{Max(R^i_{\exp})}\right)^T\left(\frac{R^i(\vec{P}) - R^i_{\exp}}{Max(R^i_{\exp})}\right)\right\}\right] \tag{4.32}$$

Where R^i_{exp} is the experimental response for the size i ($i \in [1, 2, 3]$) and $R^i(\vec{P})$ is the numerical response, $\vec{P}$ is the vector of model parameters. Several definitions can be used for the responses. Hereafter we use the stresses computed from the applied load measured for 100 values of the NMOD equally spaced and covering the whole experimental data range. Because the experimental responses and the numerical ones have however different values from one specimen size to another, it is necessary to express them in a non-dimensional way (or to use a weighted functional). This is the reason why the error between the numerical and experimental responses is divided by the maximal experimental response for each size. Five iterations are used to minimise the functional (the error reaches a minimum and remains constant afterwards). This optimization algorithm is run within the finite element code Cast3M.

Table 4.3 presents the model parameters calculated by the optimization procedure for both sets of the initial parameters. The global responses provided are given in Figure 4.19. It can be observed that the two sets give the same values for the peak load for the cases of D1 and D2 beams. For the D3 beam however, the peak load provided by the Automated Set - 1 is higher. Thus, and in terms of size effect the two sets of parameters give different results. Furthermore, comparison with the experimental data shows that calibration is poor in the post-peak regime.

Table 4.3 Nonlocal model parameters from the optimization algorithm.

	κ_{D0}	A_t	B_t	l_c (mm)
Automated Set – 1	3.52×10^{-5}	0.78	5089	15.3
Automated Set – 2	5.22×10^{-5}	0.80	22660	68.0

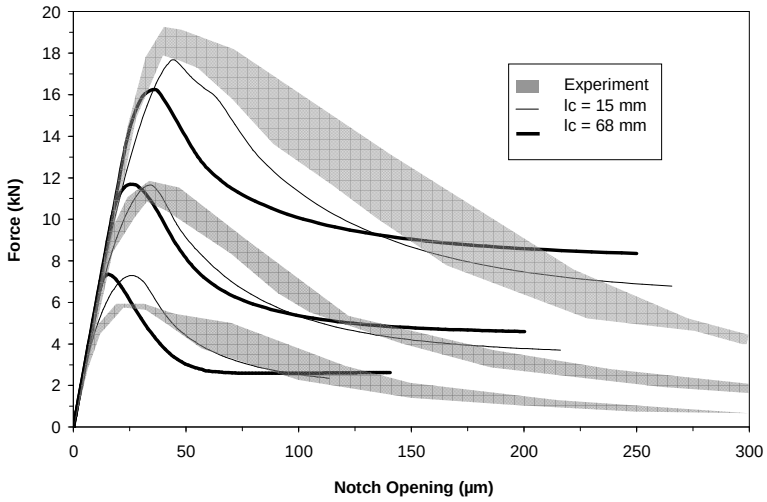

Figure 4.19 Global responses of geometrical similar beams using the automated nonlocal model parameters.

It seems that the robustness of the optimization procedure is limited and is highly dependent on a good estimation of the initial parameter set. In addition, the estimation of a single set of parameter that provides an acceptable fitting of the entire Force – NMOD curves of several specimen sizes does not necessarily correspond to a correct prediction of the peak loads [58].

In the previous identification procedure, the internal length l_c is treated as a general parameter in the boundary value problem and a constant value of l_c is used for the different specimens' sizes. However, recent experimental studies have shown that the FPZ width varies with the specimen size [94, 38, 37, 36].

Finally, Iacono and co-workers [58] have shown that even when using an inverse analysis for identifying the model parameters, calibration based on three points bending experimental data does not provide acceptable predictions for tensile tests.

4.4.4 Size effect and computation of global fracture parameters

The results are transported into the normalized size effect plot in two ways (Figure 4.20):

- In Figure 4.20(a), the normalization parameters $D°$ and Bf_t are obtained from numerical results at the peak load condition. Bazant's size effect law (SEL) is also presented. The computed points are located on the right hand side of the size effect curve and a strong size effect on the nominal strength is observed for both sets of model parameters. The results obtained from the second parameter set ($l_c = 68mm$) present a relatively more brittle behaviour (closer to the LEFM law) compared to results obtained from the first parameter set ($l_c = 15mm$). Nevertheless, the computed results are not in good agreement with the experimental results.
- The fracture parameters can also be calculated from the numerical results using the size effect method [107] (Table 4.4). It can be seen that the normalization parameters $D°$ and Bf_t coming from the experiments and the computations are not similar. This may be the first reason of the disagreement between the experimental and numerical points on the size effect plot. The fracture energy G_f obtained from the numerical results is lower and thus a more brittle behaviour is obtained. The characteristic length l_{ch}^* according to Hillerborg is also deduced (using Equation 4.9). This characteristic length has already been used by Bazant and Pfeiffer in [12] in order to determine the size of the fracture process zone. It should be noted that the computed values of l_{ch}^* do not correspond to the internal length l_c of the nonlocal model. Moreover, l_{ch}^* decreases while the nonlocal internal length l_c increases.

- In Figure 4.20(b), the computed results are normalized using the same parameters $D°$ and Bf_t as for normalizing the experimental data. Now the numerical results are situated on the left hand side of the size effect curve. Nevertheless, they do not follow Bazant's size effect law; they present instead a steep decrease in the nominal strength compared to the experimental results.

Table 4.4 Size independent Fracture parameters.

Parameter set	D^0 (mm)	Bf_t (MPa)	G_f (N/m)	l_{ch}^* (mm)
l_c = 15mm	88.9	4.78	31.6	52.6
l_c = 68mm	28.60	7.23	23.6	16.9
Experiment	423.3	3.02	60.2	250.2

l_{ch}^* is the material characteristic length according to Hillerborg (Equation 4.9).

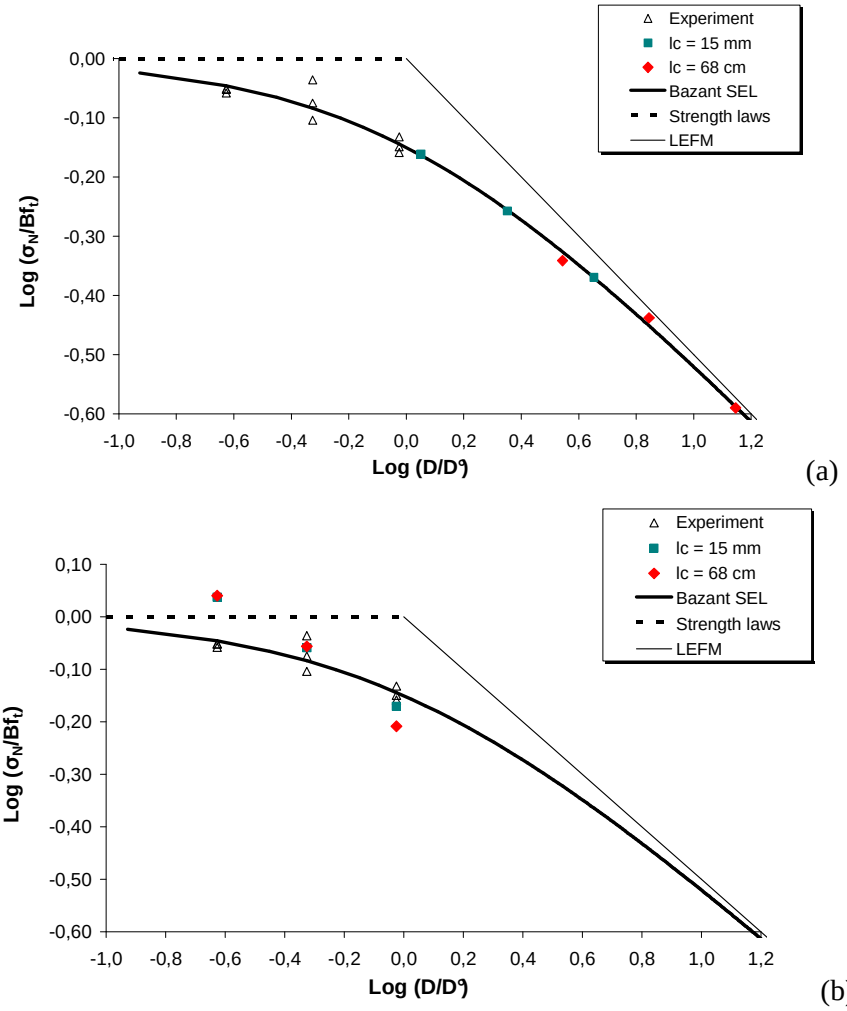

Figure 4.20 Size effect plots (a) Data are normalized with different parameters (b) data are normalized using the same parameters as the experimental data.

4.4.5 *Evolution of the damage variable*

The evolution of the internal damage variable d is studied hereafter. d is a scalar variable and is computed from Equations 4.20 and 4.23. Its value varies from 0 to 1 (when d = 1 the material is completely damaged). Figure 4.21 presents the damage field at peak load and at the tail end of the Force-NMOD curve. An important effect of the internal length l_c on the width of the damaged zone can be observed. The width of the damage zone increases with increasing internal length.

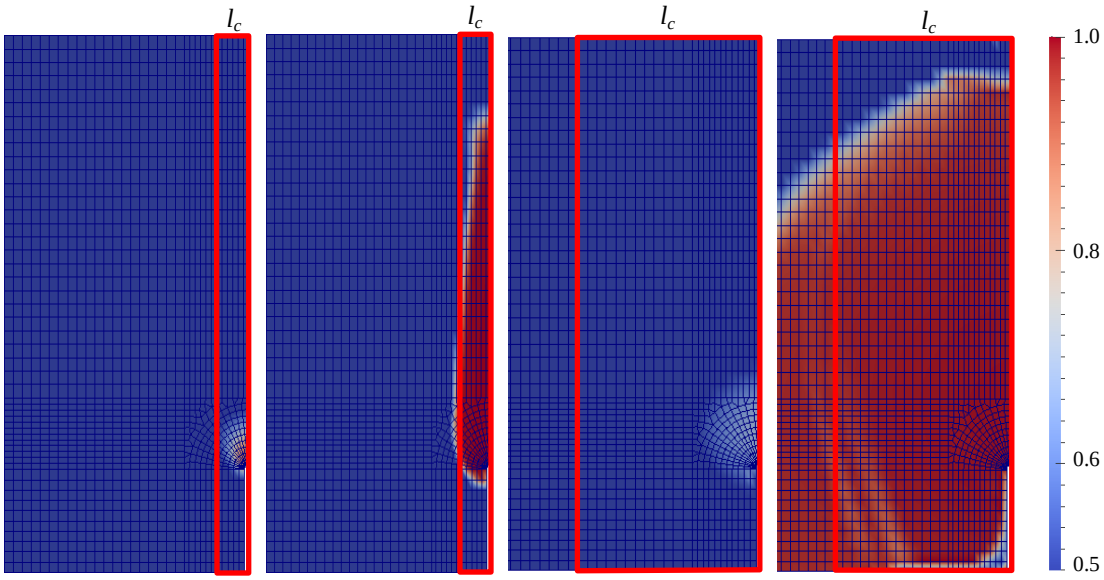

Figure 4.21 Evolution of internal damage variable in D2 beam (a) at peak load, l_c = 15mm (b) at the tail of the F-NMOD curve, l_c = 15mm (c) at peak load, l_c = 68mm (d) at the tail of the F-NMOD curve, l_c = 68mm.

In Figure 4.21(a), the internal length, l_c is almost the same to the zone in which damage is localized. As the beam is further loaded, damage grows but the width of the localization zone stays almost the same (Figure 4.21(b)). In Figure 4.21(c), l_c is now much larger as compared to the zone in which damage is localized. Later on however, the damage zone grows and at the tail of the Force-CMOD curve its width is several times the characteristic length (Figure 4.21(c)).

4.4.6 *Estimation of crack opening and comparison with experiments*

Figure 4.22 presents the crack opening profile using two ways, the displacement jump method and the method proposed by Matallah and co-workers [81]. It can be seen that the later method underestimates the crack opening as it is better suited for a local formulation of the damage model. The displacement

jump method reproduces better the experimental crack opening profile (the method is based on measuring the displacement jump between two points on the either side of the zone of width equals to the internal length l_c). In the following, only the displacement jump method is therefore used to analyse the results of crack openings.

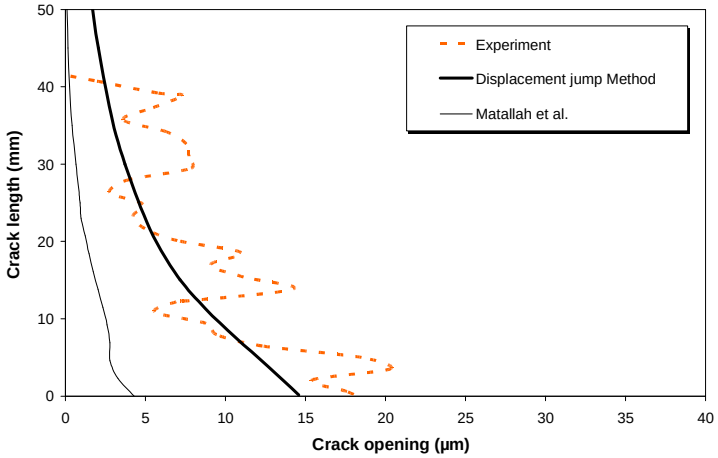

Figure 4.22 Crack opening profile at peak load using two methods (l_c = 15*mm*, D2 specimen).

4.4.7 Influence of characteristic length on the crack opening profile

Crack opening profiles are estimated at different loading conditions for each set of model parameters (Figure 4.23). It is noticed that the characteristic length has a significant influence on the results. For l_c = 15*mm*, the profile is divided into two straight lines with a smooth transition between the two lines. The initial straight line follows well the experimental data. However, the second straight line disagrees with the experimental data. In other words, the numerical crack length is longer compared to the experimental crack length. This is because in the upper part of the crack (close to the compression zone) the nonlocal strains are influenced by the compressive stresses (known as boundary effect). Therefore, in the following only the initial part of the crack opening profile is considered. The crack opening profile for l_c = 68*mm* is essentially a straight line and it is not reproducing correctly the experimental results.

The crack opening profiles at different loading stages show that the numerical profile agrees well with the experimental profile in the pre-peak regime. As the specimen passes the peak load the discrepancy between experimental and numerical profile increases. This may be due to the incapability of the model to predict accurately the post-peak fracture state of the beam. This can be also seen in the global F-NMOD curves, where coherence of experimental and numerical curves in the post-peak regime is not satisfactory (Figure 4.19).

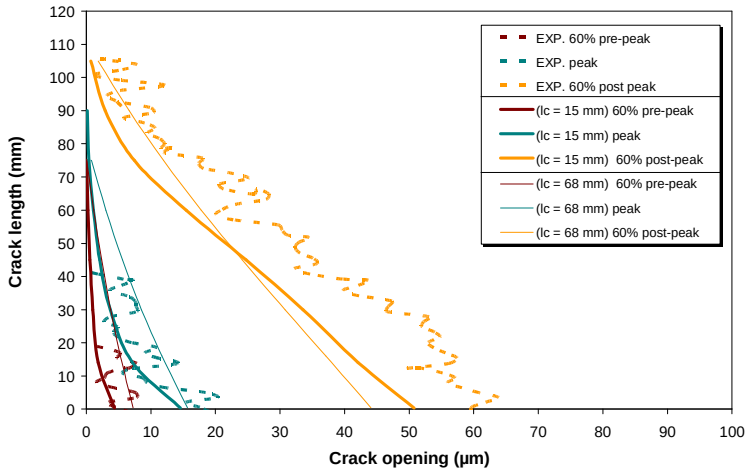

Figure 4.23 Crack opening profile (D2 specimen).

4.4.8 Size effect on computed crack opening profile

The influence of the beam dimensions (size effect) on the crack opening profile is finally analysed. Figure 4.24 presents the crack opening profile at peak load for three geometrically similar sizes of beams. It can be observed that the initial part of the crack opening profile is practically the same for all three sizes. This is in accordance with the experimental findings (Figure 3.31) i.e. specimens of geometrically similar sizes show the same crack opening profile at their peak loads and the relative crack length (crack length/specimen height) decreases when the specimen size increases.

In the original version of size effect law proposed by Bazant [7], the relative crack length at peak load in concrete specimens of varying sizes is assumed constant. This is clearly not found in this study either with the numerical simulations or the experimental data.

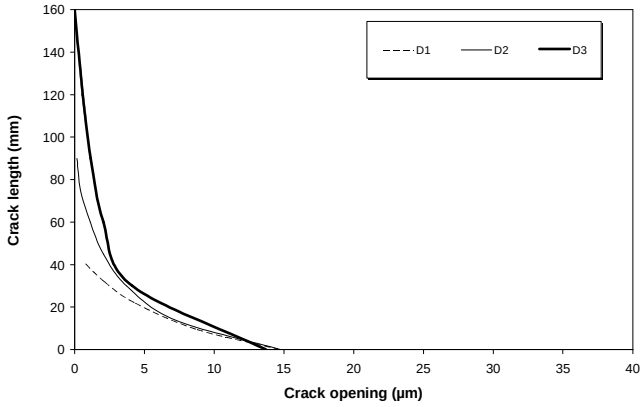

Figure 4.24 Size effect on crack opening profile at peak load ($l_c = 15mm$).

Finally, the upper part of the crack opening profiles is not same when the size of the specimens increases. However, it is assumed that due to boundary effect on the nonlocal strains, the results of crack openings are not good in this part and therefore it is not considered in the above size effect analysis.

Conclusion

In this chapter, a numerical investigation on the influence of size effect on crack opening, crack length and crack propagation is presented. An isotropic nonlocal strain softening damage model is used. Calibration of the internal length and other model parameters are done by using the Levenberg Marquardt algorithm. It is concluded that the robustness of the optimization procedure is limited and is highly dependent on a good estimation of the initial parameter set. In addition, the estimation of a single set of parameter that provides an acceptable fitting of the entire Force-Notch mouth opening displacement curves of several specimen sizes does not necessarily correspond to a correct prediction of the peak loads. In general, the computed results are not in good agreement with the experimental results. The fracture parameters are calculated from the numerical results using the size effect method [107] (Table 4.4). It can be seen that the normalization parameters $D°$ and Bf_t coming from the experiments and the computations are not similar. The fracture energy G_f obtained from the numerical results is lower and thus a more brittle behaviour is obtained. The characteristic length l_{ch}^* according to Hillerborg is also deduced from Equation 4.9. It should be noted that the computed values of l_{ch}^* do not correspond to the internal length l_c of the nonlocal model (l_{ch}^* decrease while the nonlocal internal length l_c increase).

The damage mechanics model is able to produce localization of damage but not the cracking itself. Information about crack opening profile is extracted using a post processing method. The crack opening data is extracted as the relative displacement field between the nodes of the finite element on either side of the localized damage zone of width equals to internal length. The crack opening profiles at different loading stages show that the numerical profile agrees well with the experimental profile in the pre-peak regime. As the specimen passes the peak load the discrepancy between experimental and numerical profile increases. This may be due to the incapability of the model to predict accurately the post-peak fracture state of the beam.

The influence of beam dimensions (size effect) on the crack opening profile is finally analysed. Figure 4.24 presents the crack opening profile at peak load for three geometrically similar sizes of beams. It can be observed that crack profile is practically the same for all three sizes. This is in accordance with the experimental findings (Figure 3.31) i.e. specimens of geometrically similar sizes show the same crack opening profile at their peak loads and the relative crack length (crack length/specimen height) decreases when the specimen size increases. In the original version of size effect law proposed by Bazant [7], the relative crack length at peak load in concrete specimens of varying sizes is assumed constant. However, this is clearly not found in this study either with the numerical simulations or the experimental data.

GENERAL CONCLUSIONS

Different theories are available in literature to differentiate between the different cracking zones. Cracking in concrete can be discretized into main crack, secondary cracks and microcracks ahead of the main and secondary cracks. However, the inner cracking zone associated with the main crack is more energetic and is responsible for the decrease of the load bearing capacity of a concrete structure. When load is applied, at first, microcracks usually form in the weakest locations of the material. The weakest locations are usually the aggregate matrix interface. As the load increases, the microcracks coalesce into the secondary and main cracks and a large amount of energy is released. Some microcracks, however, do not coalesce. They exist around the main crack and are usually termed as dead microcracks. In some parts of the crack, the crack interfaces are not completely separate. When the crack traverses a major part of the specimen/structure (i.e. just before the rupture of the specimen/structure), these small links between the crack interfaces start to break and are responsible for the tail part of the stress-strain diagram.

Many toughening mechanisms are acting ahead of the main crack in a zone called Fracture Process Zone (FPZ). These mechanisms include microcrack shielding, crack branching, crack interface bridging, aggregate interlock and crack tip blunting. A considerable amount of energy supplied by the applied load is consumed by the FPZ to overcome these mechanisms. This phenomenon becomes more important as the aggregate size is increased. When material is subjected to tensile loadings, the strains localize in the FPZ and result in the post-peak softening of the stress-strain diagram. The characterization of fracture in terms of crack opening is recently becoming more frequent for most concrete structures. Crack opening is a key parameter in order to estimate the durability of their structural components.

The fracture behaviour of concrete cannot be separated from the size effect. Different theories exist in literature, from among which the deterministic energetic size effect theory of Bazant is analysed in this study. In this case, the decrease of nominal strength while increasing the size of the structure is attributed to the growth of the fracture process zone. Bazant [7] considered fracture energy as the size independent material parameter and assumed that at peak load, the crack length is proportional to the size of the specimen. In the present study, this assumption is analysed and eventually a size effect on the fracture process of concrete is investigated.

An experimental program is carried out in which RILEM size effect method is adopted to test geometrically similar beams of various sizes. Two types of concrete mixes (M1 and M2) are used. The M1 concrete mix (maximum aggregate size = 20mm) is used in the RILEM size effect experiments.

Three point bending tests are also performed on the M2 (maximum aggregate size = 12*mm*) concrete specimens under similar loading and boundary conditions in order to study the effect of aggregate size on the fracture behaviour.

Digital image correlation (DIC) technique is used in this study to measure the cracking over the surface of the concrete specimens. It is found to be a robust and highly precise tool for fracture measurements such as crack opening and crack length. The possible error sources (lens distortion, vibrations, periodic bias and image distortions etc.) are eliminated by adopting a higher interpolation function and a higher order correlation algorithm. Two types of DIC resolutions are adopted. In the first type, the complete height of the specimen is captured and in the second type an area above the notch, which is approximately 35*mm* x 25*mm*, is captured. The second type gives a higher number of pixels per unit area of the specimen. It is observed that the two resolutions essentially give the same crack opening profile. A small zigzag nature of the crack opening profile is noticed with the lower resolution.

A procedure is developed in order to determine crack openings from displacement field obtained from DIC. The fracture process is identified by monitoring the crack openings. Crack openings start to increase rapidly after about 60% of peak load in the pre-peak regime which indicates the localization of microcracks and the formation of a macrocrack. As the specimen crosses the peak load limit, a considerable decrease in the loading capacity is observed with a gradual increase in the crack openings. In the tail part of the post-peak regime, the crack openings in the lower part of the crack increase significantly, with a relatively gradual decrease in the load bearing capacity. This is attributed to the breakage of the remaining links in the semi-cracked zones.

The analysis of the crack growth in three sizes of geometrically similar beams using DIC technique showed that (1) crack length in the pre-peak region is identical in all the beams and does not vary in proportion to the size of the beam. Thus for a smaller beam (with higher σ_N), a longer relative crack length is observed. (2) In the post-peak region, two stages of crack propagation are observed. During early post-peak, the length of the crack increases rapidly up to 50% of the peak load. However, in the final post-peak region, crack opening becomes more important than the crack length propagation. (3) In the D1 specimen during the post-peak regime, crack length propagation is relatively slower due to the boundary effect. (4) When aggregate size is reduced, a higher peak resistance is obtained. The corresponding relative crack length measured at peak load is also higher. This conclusion is similar to (1): higher resistance corresponds to a longer relative crack length.

Crack length is estimated using the crack opening profiles. It includes the length of the macrocrack and some part of the microcracking zone in which crack openings are not negligible. It is assumed that this crack length plays a significant role in the decrease of the load bearing capacity. It was found that (1) crack length in the pre-peak region is identical in all the beams and does not vary in proportion to the size of the beam. Thus for smaller beam (with higher σ_N), longer relative crack length was observed. (2) In post peak region two stages of crack propagation were observed. During early post-peak, the length of the crack increases rapidly up to 50% of the peak load. However, in the final post-peak region, crack opening becomes more important than the crack length propagation. (3) In D1 specimen during the post peak regime, crack length propagation is relatively slower due to the boundary effect. (4) When aggregate size is reduced, a higher peak resistance is obtained; the corresponding relative crack length measured at peak load is also higher. This conclusion is similar to (1) that higher resistance corresponds to a longer relative crack length.

A case study is also presented in which crack openings and crack spacing in reinforced concrete beams under three point bending tests were monitored. The experimental results were compared with the design values from Eurocode 2. It was observed that (1) Eurocode 2 underestimates the crack openings for all sizes of the beams. As the strains in the rebars increase, the difference between the measured and the calculated (Eurocode 2) values increase. (2) An important size effect on the measured crack openings is observed keeping same the strain level in different sizes of the beams. This size effect is not considered in the Eurocode 2 crack control expressions. Therefore it is not well captured in the calculated crack openings. (3) Another size effect is observed on the maximum spacing between the cracks. The Eurocode 2 expression underestimates the crack spacing when the size of the specimen increases.

Numerical investigation of size effect on crack opening, crack length and crack propagation is also carried out. An isotropic nonlocal strain softening damage model is used. Calibration of the internal length and other model parameters are done by inverse calibration technique using Levenberg Marquardt algorithm. The damage mechanics model is able to produce localization of damage but not the cracking itself. Information about crack opening profile is extracted using a post processing method. The crack opening data is extracted as the relative displacement field between the nodes of the finite element on either side of the localized damage zone.

It is concluded that the robustness of the optimization procedure is limited and is highly dependent on a good estimation of the initial parameter set. In addition, the estimation of a single set of parameter that provides an acceptable fitting of the entire Force-Notch Mouth Opening curves of several specimen sizes do not necessarily correspond to a correct prediction of the peak loads. In general, the

computed results are not in good agreement with the experimental results. The fracture parameters are calculated from the numerical results using the size effect method [107]. It can be seen that the computed normalization parameters $D°$ and Bf_t and the experimental values are not similar. The fracture energy G_f obtained from the numerical results is lower and thus a more brittle behaviour is obtained. The characteristic length l_{ch}^* according to Hillerborg is also deduced from Equation 4.9. It should be noted that the computed values of l_{ch}^* do not correspond to the internal length l_c of the nonlocal model. When l_c is increased in the nonlocal model, the computed values of l_{ch}^* however, is decreased.

The crack opening profiles at different loading stages show that the numerical profile agrees well with the experimental profile in the pre-peak regime. As the specimen passes the peak load the discrepancy between experimental and numerical profile increases. This may be due to the incapability of the model to predict accurately the post-peak fracture state of the beam.

Eventually, the influence of the beam dimensions (size effect) on the crack opening profile is analysed. Figure 4.24 presents the crack opening profile at peak load for three geometrically similar sizes of beams. It can be observed that crack profile is practically the same for all three sizes. This is in accordance with the experimental findings (Figure 3.31) i.e. specimens of geometrically similar sizes show the same crack opening profile at their peak loads and the relative crack length (crack length/specimen height) decreases when the specimen size increases. In the original version of size effect law proposed by Bazant [7], the relative crack length at peak load in concrete specimens of varying sizes is assumed constant. However, this is clearly not found in this study either with the numerical simulations or the experimental data. However, it might be interesting to compare the results with the latest version of Bazant size effect law [15].

PERSPECTIVES

In the perspective of this work, further experimental research should be carried out to investigate the role of crack openings and crack length in the fracture process of concrete. Crack openings can be determined using more sophisticated techniques e.g. eXtended Digital Image Correlation (X-DIC) techniques. The combination of two more techniques can be very useful to monitor crack growth. Higher resolution cameras should be used to improve the precision of the results and to capture the maximum surface of the specimen. The crack opening profile inside the specimen should also be determined and compared with the surface crack opening profile. This can be done by using interferometry techniques together with DIC. The use of acoustic emission technique (2D) in combination with DIC can also be helpful in order to monitor fracture process zone development along with crack opening profile. This can give an insight into the theory of the variation of fracture process zone size with crack length.

The size effect on crack length can be further investigated by using notchless specimens of varying sizes or by using specimens of the same size but varying notch lengths. Also, different concrete mixtures with varying fracture energies can be used in order to investigate the relationship of size independent fracture energy term with crack length. This study can be conducted at different ages of concrete. In early stage concrete, this study may be useful for investigating fracture process zone development and early cracking of concrete. Long term durability factors such as creep should also be investigated along with the fracture process development and size effect.

Fracture or damage mechanics theories should be able to capture the size effect on global response as well as on the local fracture phenomenon. For this, it is necessary to introduce an internal length in the constitutive laws which relates directly to the experimental findings. One can use the experimental crack opening profile and growth of crack length to test the robustness of the numerical models. The inverse calibration of model parameters is a practical technique but in this case, internal length should be determined from the local fracture observations and not the global curves.

The case study presented in Chapter 3 has shown the ineffectiveness of Eurocode 2 to predict size effect on crack openings and crack spacing. The design equations can incorporate size effect by including some empirical constants. In fact, the codes should consider energetic relations in order to estimate crack openings and crack spacing. Further experimental investigation can be carried out to investigate the size effect on crack propagation in the reinforced concrete specimens.

BIBLIOGRAPHIC REFERENCES

[1] A. Alvaredo and R. Torrent. The effect of the shape of the strain-softening diagram on the bearing capacity of concrete beams. *Materials and Structures*, 20:448–454, 1987.

[2] F. E. Amparano, Y. Xi, and Y.-S. Roh. Experimental study on the effect of aggregate content on fracture behavior of concrete. *Engineering Fracture Mechanics*, 67(1):65 – 84, 2000.

[3] H. Askes. *Advanced spatial discretisation strategies for localised failure. mesh adaptivity and meshless methods*. PhD thesis, Delft University of Technology, Faculty of Civil Engineering and Geosciences., 2000.

[4] G. I. Barenblatt. The formation of equilibrium cracks during brittle fracture. general ideas and hypothesis, axially symmetric cracks. *Prikl. Mat. Mekh.*,, 23(3):434–444, 1959.

[5] J. Baruchel, E. Buffiere, J. Y.and Maire, P. Merle, and G. Peix. *X-Ray Tomography in Material Sciences*. Hermes Science (Paris), 2000.

[6] Z. P. Bazant. Instability, ductility and size effect in strain-softening concrete. *Journal of Engineering Mechanics Division, American Society of Civil Engineers*, 102:331–344, 1976.

[7] Z. P. Bazant. Size effect in blunt fracture: Concrete, rock, metal. *Journal of Engineering Mechanics (ASCE)*, 110(4):518–535, 1984.

[8] Z. P. Bazant. Scaling of quasibrittle fracture and the fractal question. *ASME Journal of Materials and Technology*, 117:361–367, 1995.

[9] Z. P. Bazant. Scaling of quasibrittle fracture: hypotheses of invasive and lacunar fractality, their critique and weibull connection. *International Journal of Fracture*, 83:41–65, 1997.

[10] Z. P. Bazant. *Scaling of structural strength*. Hermes Penton, 2005.

[11] Z. P. Bazant and B. Oh. Crack band theory for fracture of concrete. *Materials and Structures*, 16:155–177, 1983.

[12] Z. P. Bazant and P. A. Pfeiffer. Determination of fracture energy from size effect and brittleness number. *ACI Materials Journal*, 84:463–480, 1987.

[13] Z. P. Bazant and G. Pijaudier-Cabot. Measurement of characteristic length of nonlocal continuum. *Journal of Engineering Mechanics*, 115(4):755–767, 1989.

[14] Z. P. Bazant and J. Planas. *Fracture and Size Effect in Concrete and Other Quasibrittle Materials*. CRC Press, Boca Raton and London, 1998.

[15] Z. P. Bazant and Q. Yu. Universal size effect law and effect of crack depth on quasi-brittle structure strength. *Journal of Engineering Mechanics*, 135(2):78–84, 2009.

[16] A.W Beeby. Calculation of crack width, pren 1992-1 (final draft), chapter 7.3.4. Technical report, 2001.

[17] A.W. Beeby. Crack control provisions in the new eurocode for the design of concrete structures. *ACI Special publication*, 204:57–84, 2001.

[18] C. Le Bellégo, J.F. Dubé, G. Pijaudier-Cabot, and B. Gérard. Calibration of nonlocal damage model from size effect tests. *European Journal of Mechanics - A/Solids*, 22(1):33 – 46, 2003.

[19] G. Borino, B. Failla, and F. Parrinello. A symmetric nonlocal damage theory. *International Journal of Solids and Structures*, 40(13-14):3621 – 3645, 2003.

[20] D. Broek. *The Practical Use of Fracture Mechanics*. Kluwer Academic Publishers, The Hague, 1988.

[21] H. Bruck, S. McNeill, M. Sutton, and W. Peters. Digital image correlation using newton-raphson method of partial differential correction. *Experimental Mechanics*, 29:261–267, 1989.

[22] J. Carmeliet. Optimal estimation of gradient damage parameters from localization phenomena in quasi-brittle materials. *Mech. Cohes.-Frict. Mater.*, 4(1):1–16, 1999.

[23] A. Carpinteri. Decrease of apparent tensile and bending strength with specimen size: Two different explanations based on fracture mechanics. *International Journal of Solids and Structures*, 25(4):407 – 429, 1989.

[24] A. Carpinteri. Fractal nature of material microstructure and size effects on apparent mechanical properties. *Mechanics of Materials*, 18(2):89 – 101, 1994.

[25] L. Cedolin, S. D. Poli, and I. Iori. Experimental determination of the fracture process zone in concrete. *Cement and Concrete Research*, 13(4):557 – 567, 1983.

[26] T. P. Chang, K. L. Taso, and B. R. Lin. Effect of aggregate on fracture properties of high-performance concrete. In H Mihashi and K Rokugo, editors, *Proceeding of 3rd International Conference on Fracture Mechanics of Concrete Structures (FRAMCOS-3)*, pages 151–160, 1998.

[27] B. Chen and J. Liu. Effect of aggregate on the fracture behavior of high strength concrete. *Construction and Building Materials*, 18(8):585 – 590, 2004.

[28] S. Choi and S. P. Shah. Measurement of deformations on concrete subjected to compression using image correlation. *Experimental Mechanics*, 37:307–313, 1997.

[29] T. Chu, W. Ranson, and M. Sutton. Applications of digital-image-correlation techniques to experimental mechanics. *Experimental Mechanics*, 25:232–244, 1985.

[30] D. Corr, M. Accardi, L. Graham-Brady, and S. P. Shah. Digital image correlation analysis of interfacial debonding properties and fracture behavior in concrete. *Engineering Fracture Mechanics*, 74(1-2):109–121, 2007.

[31] B. N. Cox and D. B. Marshall. Concepts for bridged cracks in fracture and fatigue. *Acta Metallurgica et Materialia*, 42(2):341 – 363, 1994.

[32] R. De Borst and J. Pamin. Gradient plasticity in numerical simulation of concrete cracking. *European Journal of Mechanics – A/Solids*, 15(2):295–320, 1996.

[33] R. De Borst, L. J. Sluys, H. B. Muhlhaus, and J. Pamin. Fundamental issues in finite element analyses of localization of deformation. *Engineering Computations: Int J for Computer-Aided Engineering*, 10:99–121, 1993.

[34] M. di Prisco, L. Ferrara, F. Meftah, J. Pamin, R. de Borst, J. Mazars, and J. M. Reynouard. Mixed mode fracture in plain and reinforced concrete: some results on benchmark tests. *International Journal of Fracture*, 103:127–148, 2000.

[35] S. Diamond, S. Mindess, F. P. Glasser, L. W. Roberts, Skalny J. P., and L. D. Wakeley. Microstructure of cement-based systems/bondings and interfaces in cementitious materials. In *Proceedings MRS Fall meeting*, volume 370, Boston, 1994. MRS, Pittsburgh.

[36] K. Duan, X. Hu, and F. H. Wittmann. Boundary effect on concrete fracture and non-constant fracture energy distribution. *Engineering Fracture Mechanics*, 70(16):2257 – 2268, 2003.

[37] K. Duan, X. Hu, and F. H. Wittmann. Scaling of quasi-brittle fracture: Boundary and size effect. *Mechanics of Materials*, 38(1-2):128–141, 2006.

[38] K. Duan, X. Hu, and F.H. Wittmann. Explanation of size effect in concrete fracture using non-uniform energy distribution. *Materials and Structures*, 35:326–331, 2002.

[39] D.S. Dugdale. Yielding of steel sheets containing slits. *Journal of Mechanics and Physics of Solids*, 8:100–108, 1960.

[40] European Committee for Standardization (CEN), Brussels. *Eurocode 2: Design of concrete structures – Part 1-1: General rules and rules for buildings.*, December 2004.

[41] R. Feldman and P. Sereda. A model for hydrated portland cement paste as deduced from sorption-length change and mechanical properties. *Materials and Structures*, 1:509–520, 1968.

[42] E. Ferrié, J. Y. Buffière, W. Ludwig, A. Gravouil, and L. Edwards. Fatigue crack propagation: In situ visualization using x-ray microtomography and 3d simulation using the extended finite element method. *Acta Materialia*, 54(4):1111 – 1122, 2006.

[43] L. H. C. Fisher, R. A.and Tippett. Limiting forms of the frequency distribution of the largest and smallest number of a sample. In *Proceedings Cambridge Philosophical Society*, volume 24, pages 180–190, 1928.

[44] M. Fréchet. Sur la loi de probabilité de l'écart maximum. In *Ann. Soc. Polon. Math.*, volume 6, page 93, Cracow, 1927.

[45] C. Giry, F. Dufour, J. Mazars, and P. Kotronis. Stress state influence on nonlocal interactions in damage modelling. In *Computational Modelling of Concrete Structures, Proceedings of the Euro-C 2010 Conference*, 2010.

[46] V. S. Gopalaratnam and S. P. Shah. Softening response of plain concrete in direct tension. *ACI Journal Proceedings*, 82(3):310–323, 1985.

[47] A. A. Griffith. The phenomena of rupture and flow in solids. *Phiilos. T. Roy. Soc. A*, 221:163–197, 1921.

[48] A. A. Griffith. The theory of rupture. In *Proceedings of the First International Conference of Applied Mechanics*, pages 55–63, 1924.

[49] A. Guvenilir, T. M. Breunig, J. H. Kinney, and S. R. Stock. Direct observation of crack opening as a function of applied load in the interior of a notched tensile sample of al—li 2090. *Acta Materialia*, 45(5):1977 – 1987, 1997.

[50] A. Hillerborg. The theoretical basis of a method to determine the fracture energy of concrete. *Materials and Structures*, 18:291–296, 1985.

[51] A. Hillerborg, M. Modéer, and P. E. Petersson. Analysis of crack formation and crack growth in concrete by means of fracture mechanics and finite elements. *Cement and Concrete Research*, 6(6):773–781, 1976.

[52] H. K. Hilsdorf and W. Brameshuber. Code-type formulation of fracture mechanics concepts for concrete. *International Journal of Fracture*, 51:61–72, 1991.

[53] T. C. Hsu, F. O. Slate, G. M. Sturman, and G. Winter. Microcracking of plain concrete and the shape of the stress-strain curve. *ACI journal proceedings*, 60(2):209–224, 1963.

[54] X. Hu. Toughness measurement from crack close to free edge. *International Journal of Fracture*, 86:L63–8, 1997.

[55] X. Hu and F. H. Wittmann. An analytical method to determine the bridging stress transferred within the fracture process zone: I, general theory. *Cement and Concrete Research*, 21(6):1118 – 1128, 1991.

[56] X. Hu and F. H. Wittmann. Size effect on toughness induced by crack close to free surface. *Engineering Fracture Mechanics*, 65(2-3):209 – 221, 2000.

[57] X. Hu and F.H. Wittmann. Fracture energy and fracture process zone. *Materials and Structures*, 25:319–326, 1992.

[58] C. Iacono, L.J. Sluys, and J.G.M. van Mier. Calibration of a higher-order continuum model using global and local data. *Engineering Fracture Mechanics*, 75(16):4642 – 4665, 2008.

[59] G. R. Irwin, J. A. Kies, and H. L. Smith. Fracture strengths relative to the onset and arrest of crack propagation. *Proc ASTM*, 58:640–657, 1958.

[60] J. P. Jacobs. Commentary eurocode 2. Technical report, European Concrete Platform ASBL, Brussels, June 2008.

[61] Y. S. Jenq and S. P. Shah. A two parameter fracture model for concrete. *Journal of Engineering Mechanics (ASCE)*, 111:1227–1241, 1985.

[62] M. Jirasek and B. Patzak. Consistent tangent stiffness for nonlocal damage models. *Computers & Structures*, 80(14-15):1279 – 1293, 2002.

[63] M. F. Kaplan. Crack propagation and the fracture concrete. *ACI Journal*, 58(11), 1961.

[64] B. L. Karihaloo and P. Nallathambi. Determination of specimen-size independent fracture toughness of plain concrete. *Magazine of Concrete Research*, 38:67–76, 1986.

[65] B. L. Karihaloo and P. Nallathambi. *Fracture Test Methods for Concrete*, chapter Notched beam test: mode I fracture toughness, page 1–86. Chapman and Hall, London, 1991.

[66] C. E. Kesler, D. J. Naus, and J. L. Lott. Fracture mechanics-its applicability to concrete. In *Proceeding of International Conference on the Mechanical Behaviour of Materials*, Kyoto, 1971.

[67] H. D. Kleinschrodt and H. Winkler. The influence of maximum aggregate size and the size of specimen on fracture mechanics parameters. In F.H. Wittmann, editor, *Fracture Toughness and Fracture Energy of Concrete*, pages 396–402. Elsevier Science Publishers, Amsterdam, 1986.

[68] A. Krayani, G. Pijaudier-Cabot, and F. Dufour. Boundary effect on weight function in nonlocal damage model. *Engineering Fracture Mechanics*, 76(14):2217 – 2231, 2009.

[69] P. Kreijger. The skin of concrete composition and properties. *Materials and Structures*, 17:275–283, 1984.

[70] E. N. Landis and S. P. Shah. The influence of microcracking on the mechanical behavior of cement based materials. *Advanced Cement Based Materials*, 2(3):105 – 118, 1995.

[71] J. S. Lawler, D. T. Keane, and S. P. Shah. Measuring three-dimensional damage in concrete under compression. *ACI Materials Journal*, 98(6):465–475, 2001.

[72] R.H. Leicester. The size effect of notches. In *Proceeding of 2nd Australian Conference of Mechanics of Structures and Materials*, pages 4.1–4.20, Melbourne, 1969.

[73] S. Levasseur, F. Collin, R. Charlier, and D. Kondo. On a class of micromechanical damage models with initial stresses for geomaterials. *Mechanics Research Communications*, 37(1):38 – 41, 2010.

[74] Z. Li, S. Kulkarni, and S. P. Shah. New test method for obtaining softening response of unnotched concrete specimen under uniaxial tension. *Experimental Mechanics*, 33:181–188, 1993.

[75] Z. Li and S. P. Shah. Localization of microcracking in concrete under uniaxial tension. *Materials Journal*, 91(4):372–381, 1994.

[76] P. Luo, Y. Chao, M. Sutton, and W. Peters. Accurate measurement of three-dimensional deformations in deformable and rigid bodies using computer vision. *Experimental Mechanics*, 33:123–132, 1993.

[77] R. Mahnken and E. Kuhl. Parameter identification of gradient enhanced damage models with the finite element method. *European Journal of Mechanics - A/Solids*, 18(5):819 – 835, 1999.

[78] B. B. Mandelbrot, D.. E. Passoja, and A. J. Paullay. Fractal character of fracture surfaces of metals. *Nature*, 308(5961):721–722, 1984.

[79] J.C. Maso. Interfaces in cementitious composites. In *RILEM Proceedings 18*. E&FN Spon/Chapman & Hall, London/New York, 1992.

[80] M. Matallah and La Borderie C. Analyse critique des résultats du benchmark ceos.fr. Technical report, Projet MEFISTO (GT1-1), 15 Juin 2009.

[81] M. Matallah, C. La Borderie, and O. Maurel. A practical method to estimate crack openings in concrete structures. *Int. J. Numer. Anal. Meth. Geomech.*, 34(15):1615–1633, 2010.

[82] J. Mazars. *Application de la mécanique de I'endommagement au comportement non linéaire et à la rupture du béton de structure*. PhD thesis, L.M.T.-University Paris 6, France, 1984.

[83] J. Mazars and G. Pijaudier-Cabot. From damage to fracture mechanics and conversely: A combined approach. *International Journal of Solids and Structures*, 33(20-22):3327 – 3342, 1996.

[84] J. M. Melenk and I. Babuska. The partition of unity finite element method: Basic theory and applications. *Computer Methods in Applied Mechanics and Engineering*, 139(1-4):289 – 314, 1996.

[85] H. Mihashi. Stochastic theory of concrete fracture. In F.H. Wittmann, editor, *Fracture Mechanics of Concrete*, pages 301–339. Elsevier Science Publishers, Amsterdam, 1983.

[86] H. Mihashi. States of the art and a view of the fracture mechanics of concrete. *Journal of JCI*, 25(2):14–25, 1987.

[87] H. Mihashi and M. Izumi. A stochastic theory for concrete fracture. *Cement and Concrete Research*, 7(4):411 – 421, 1977.

[88] H. Mihashi, N. Nomura, and S. Niiseki. Influence of aggregate size on fracture process zone of concrete detected with three dimensional acoustic emission technique. *Cement and Concrete Research*, 21(5):737 – 744, 1991.

[89] R. A. Miller, A. Castro-Montero, and S. P. Shah. Cohesive crack models for cement mortar examined using finite-element analysis and laser holographic measurements. *Journal of the American Ceramic Society*, 74(1):130–138, 1991.

[90] S. Mindess. Interfaces in concrete. In J. Skalny, editor, *Materials Science of Concrete I*, page 163. The American Ceramic Society, Westerville, OH, 1989.

[91] S. Mindess. Fracture process zone detection. In S.P. Shah and A. Carpinteri, editors, *Report RILEM TC 89-FMT 'Fracture Mechanics Test-Methods for Concrete*, page 231–261. Chapman & Hall, London/New York, 1991.

[92] N. Moes and T. Belytschko. Extended finite element method for cohesive crack growth. *Engineering Fracture Mechanics*, 69(7):813 – 833, 2002.

[93] N. Moes, J. Dolbow, and T. Belytschko. A finite element method for crack growth without remeshing. *Int. J. Numer. Meth. Engng.*, 46(1):131–150, 1999.

[94] K. Otsuka and H. Date. Fracture process zone in concrete tension specimen. *Engineering Fracture Mechanics*, 65(2-3):111–131, 2000.

[95] C. Ouyang and S.P. Shah. Fracture energy approach for predicting cracking of rein-forced concrete tensile members. *ACI Structural Journal*, 91:69–78, 1994.

[96] F.T. Peirce. Tensile tests on cotton yarns-v. the weakest link. *Journal of Textile Institue*, 17:355–368, 1926.

[97] G. Pijaudier-Cabot. *Continuum models for materials with microstructure*, chapter Non local Damage. Jihn Wiley Pubs., 1995.

[98] G. Pijaudier-Cabot and Z. P. Bazant. Nonlocal damage theory. *Journal of Engineering Mechanics*, 113(10):1512–1533, 1987.

[99] G. Pijaudier-Cabot, K. Haidar, and J. F. Dubé. Non-local damage model with evolving internal length. *Int. J. Numer. Anal. Meth. Geomech.*, 28(7-8):633–652, 2004.

[100] G. Pijaudier-Cabot, J. Mazars, and J.Pulikowski. Steel-concrete bond analysis with nonlocal continuous damage. *Journal of Structural Engineering*, 117(3):862–882, 1991.

[101] T. C. Powers. The physical structure and engineering properties of concrete. In *Research and Development Bulletin No. 90*. Portland Cement Association, Skokie, IL., 1958.

[102] M. E. Raiss, J. W. Dougill, and J. B. Newman. Observation of the development of fracture process zones in concrete. In S.P. Shah, S.E. Swartz, and B. Barr, editors, *Fracture of Concrete and Rock –Recent Developments*, page 243–253. Elsevier Applied Science, London, New York, 1989.

[103] Y. R. Rashid. Analysis of prestressed concrete pressure vessels. *Nuclear Engineering and Design*, 7(4):334–344, 1968.

[104] J. R. Rice. The localization of plastic deformation. In A. t. Koiter, editor, *Theoretical and Applied Mechanics, Proceedings on tghe 14th International Congress on Theoretical and Applied Mechanics*, volume 1, pages 207–220. North-Holland Publishing, 1976.

[105] Recommendation RILEM. Determination of the fracture energy of mortar and concrete by means of three-point bend tests on notched beams. *Materials and Structures*, 18:287–290, 1985.

[106] Recommendation RILEM. Determination of fracture parameters kic and ctodc of plain concrete using three-point bend tests. *Materials and Structures*, 23:457–460, 1990.

[107] Recommendation RILEM. Size-effect method for determining fracture energy and process zone size of concrete. *Materials and Structures*, 23:461–465, 1990.

[108] P. E. Roelfstra and F. H. Wittmann. *Fracture Toughness and Fracture Energy*, chapter Numerical method to link strain softening with failure of concrete, pages 163–175. Elsevier Science Publishers, Amsterdam, 1986.

[109] S .Roux, J. Réthoré, and F. Hild. Digital image correlation and fracture: an advanced technique for estimating stress intensity factors of 2d and 3d cracks. *Journal of Physics D: Applied Physics*, 42(21):214004, 2009.

[110] J. Réthoré, S. Roux, and F. Hild. From pictures to extended finite elements: extended digital image correlation (x-dic). *Comptes Rendus Mécanique*, 335(3):131 – 137, 2007.

[111] J. Réthoré, J. P. Tinnes, S. Roux, J. Y. Buffière, and F. Hild. Extended three-dimensional digital image correlation (x3d-dic). *Comptes Rendus Mécanique*, 336(8):643 – 649, 2008.

[112] K. Scrivener and E. M. Gartner. Microstructural gradients in cement paste around aggregate particles. In S. Mindess and S.P. Shah, editors, *Bonding in Cementitious Composites*. Material Research Society, Pittsburgh, 1988.

[113] A. Sellier and B. Bary. Coupled damage tensors and weakest link theory for the description of crack induced anisotropy in concrete. *Engineering Fracture Mechanics*, 69(17):1925 – 1939, 2002.

[114] S. P. Shah, S. E. Swartz, and C. Ouyang. *Fracture mechanics of concrete: Applications of fracture mechanics to concrete, rock and other quasi-brittle materials*. Wiley (New York), 1995.

[115] A. Shterenlikht, P. Lopez-Crespo, P. J. Withers, J. R. Yates, and E. A. Patterson. Mixed mode (i+ii) stress intensity factor measurement using image correlation. In E. E. Gdoutos, editor, *Fracture of Nano and Engineering Materials and Structures*, pages 427–428. Springer Netherlands, 2006.

[116] M. Sutton, S. McNeill, J. Helm, and Y. Chao. Advances in two-dimensional and three-dimensional computer vision. In Pramod Rastogi, editor, *Photomechanics*, volume 77 of *Topics in Applied Physics*, pages 323–372. Springer Berlin / Heidelberg, 2000.

[117] M. A. Sutton, S. R. McNeill, and M. Jang, J.; Babai. Effects of subpixel image restoration on digital correlation error estimates. *Optical Engineering*, 27:870–877, 1988.

[118] T. Tang, S. P. Shah, and C. Ouyang. Fracture mechanics and size effect of concrete in tension. *Journal of Structural Engineering*, 118(11):3169–3185, 1992.

[119] T. Tang, D. G. Zollinger, and R. H. Yoo. Fracture toughness of concrete at early ages. *ACI Materials Journal*, 90(5):463–471, 1993.

[120] L. H. C. Tippett. On the extreme individuals and the range of samples. *Biometrika*, 17:364, 1925.

[121] W. Tong. An evaluation of digital image correlation criteria for strain mapping applications. *Strain*, 41(4):167–175, 2005.

[122] J. G. M. Van Mier. Fracture study of concrete specimens subjected to combined tensile and shear loadings. In J.F. Jullien, editor, *Proceedings International Conference on 'Measurement*

and Testing in Civil Engineering', volume 1, page 337–347, Lyon–Villeurbanne, September 13–16: 1988 1988.

[123] J. G. M. Van Mier. Mode i fracture of concrete: Discontinuous crack growth and crack interface grain bridging. *Cement and Concrete Research*, 21(1):1 – 15, 1991.

[124] J. G. M. Van Mier. *Fracture processes of concrete: assessment of material parameters for fracture models*. CRC Press, Boca Raton, 1997.

[125] J. G. M. Van Mier and M. B. Nooru-Mohamed. Geometrical and structural aspects of concrete fracture. *Engineering Fracture Mechanics*, 35(4-5):617 – 628, 1990.

[126] J. G. M. Van Mier, E. Schlangen, and A. Vervuurt. Tensile cracking in concrete and sandstone: Part 2: Effect of boundary rotations. *Materials and Structures*, 29:87–96, 1996.

[127] J. G.M. Van Mier and H. K. Man. Some notes on microcracking, softening, localization, and size effects. *International Journal of Damage Mechanics*, 18(3):283–309, 2009.

[128] B. Wagne, S. Roux, and F. Hild. Spectral approach to displacement evaluation from image analysis. *Eur. Phys. J. AP*, 17(3):247–252, 2002.

[129] S. Walker and D. L. Bloem. Effects of aggregate size on properties of concrete. *ACI Journal*, 57(9):283–298, 1960.

[130] P. F. Walsh. Fracture of plain concrete. *Indian concrete journal*, 46(11), 1972.

[131] W. Weibull. Phenomenon of rupture in solids. In *Proceedings, Royal Swedish Institute of Engineering Reseach*, volume 153, pages 1–55, Stockholm, 1939.

[132] A. A. Wells. Application of fracture mechanics at and beyond general yielding. *Brit. Weld. J.*, 10:563–570, 1963.

[133] F. H. Wittmann. Structure of concrete with respect to crack formation. In F.H. Wittmann, editor, *Fracture Mechanics of Concrete*, page 43. Elsevier, London/New York, 1983.

[134] F. H. Wittmann and J. V. Zaitsev. Crack propagation and fracture of composite materials such as concrete. In *Proceedings of 5th International Concference on Fracture (ICF5)*, Cannes, 1981.

[135] K. Wu, B. Chen, and W. Yao. Study of the influence of aggregate size distribution on mechanical properties of concrete by acoustic emission technique. *Cement and Concrete Research*, 31(6):919 – 923, 2001.

[136] R. Zimbelmann. A contribution to the problem of cement-aggregate bond. *Cement and Concrete Research*, 15(5):801 – 808, 1985.